MOTION OF A FLOATING CABLE-DRIVEN PLATFORM

BY

MAMON MOHAMMAD HOROUB

A Dissertation Presented to the

DEANSHIP OF GRADUATE STUDIES

KING FAHD UNIVERSITY OF PETROLEUM & MINERALS

DHAHRAN, SAUDI ARABIA

In Partial Fulfillment of the
Requirements for the Degree of

DOCTOR OF PHILOSOPHY

In

MECHANICAL ENGINEERING

March, 2016

In the name of Allah, the Most Gracious and the Most Merciful

KING FAHD UNIVERSITY OF PETROLEUM & MINERALS

DHAHRAN- 31261, SAUDI ARABIA

DEANSHIP OF GRADUATE STUDIES

This thesis, written by MAMON HOROUB under the direction his thesis advisor and approved by his thesis committee, has been presented and accepted by the Dean of Graduate Studies, in partial fulfillment of the requirements for the degree of **DOCTOR OF PHILOSOPHY IN MECHANICAL ENGINEERING**

Dr. Muhammad Hawwa
(Advisor)

Dr. Zuhair Mattoug Gasem
Department Chairman

Dr. Ahmad Masoud
(Member)

Dr. Salam A. Zummo
Dean of Graduate Studies

Dr. Mehmet Sunar
(Member)

4/8/16
Date

Dr. Moustafa Elshafei
(Member)

Dr. Yagoub N. Al-Nassar
(Member)

2016

Dedicated

to

My Beloved Parents,

My wife, My Sons,

My Brothers, and My Sisters

ACKNOWLEDGMENTS

All praise and thanks are due to Almighty **Allah**, Most Gracious and Most Merciful, for his immense beneficence and blessings. He bestowed upon me health, knowledge and patience to complete this work. May peace and blessings be upon prophet Muhammad (PBUH), his family and his companions.

Thereafter, acknowledgement is due to KFUPM through its remarkable facilities and for granting me the opportunity to pursue my graduate studies.

I acknowledge, with deep gratitude and appreciation, the inspiration, encouragement, valuable time and continuous guidance given to me by my dissertation advisor, Dr. Muhammad Hawwa. I am highly grateful to my Committee members Drs. Ahmad Masoud, Mehmet Sunar, Moustafa Elshafei and Yagoub N. Al-Nassar for their constructive guidance and support. A heartfelt thanks goes out to Dr. Mahir Hassan who provided support, mentoring, and motivation along my research.

My heartfelt thanks are due to my parents, brothers, my wife, and my sons for their prayers and moral support throughout my academic life. My parents' advice, to strive for excellence, has made all this work possible. Special thanks are due to my senior colleagues at the university, for their help, prayers and who provided wonderful company and good memories that will last a life-time.

TABLE OF CONTENTS

LIST OF TABLES

LIST OF FIGURES

LIST OF ABBRIVIATIONS

CB	Center of Buoyancy
FCDP	Floating Cable-Driven Platform
CG	Center of Gravity
C( )	Cosine function
DOF	Degree Of Freedom
MC	Metacenter
S( )	Sine function
SWL	Still Water Level
RMS	Root Mean Square
TLP	Tension Leg Platform

NOMENCLATURE

A	Water wave amplitude
A_j	Area
a	Radius of the moving platform
$\boldsymbol{a}^{(i)}$	The position vector of point $A^{(i)}$
$A^{(i)}$	Anchors' angle for ith mooring cable with respect to positive X-axis.
b	Submerged depth
$\bar{b}$	Submerged depth due to weight
$B^{(i)}$	Motors' angle with respect to positive X-axis
$b^{(i)}$	Length of the line between the moving platform center point to the attachment point $B^{(i)}$
$\overline{BM}$	Distance between the Center of Buoyancy and the Metacenter
c	Water wave velocity
C	Damping matrix
C_a	Added mass coefficient
d	Water depth
D	Diameter of platform
$\boldsymbol{e}^{(i)}$	The unit vector in the direction from the moving platform center point to the attachment point $B^{(i)}$
eig	Eigen value
F	Force vector
F_b	Buoyancy force
f_j^k	jth natural frequency of the moving platform at the kth location
GM	Metacentric height
h	Platform Height
H	Water wave height
H_m	Hankel function

I_{ii}	Total mass moment of inertia in the ith DOF
I_m	Modified Bessel function
J_m	Bessel function
$\mathbf{J}$	Jacobean matrix
$\mathbf{K}$	Stiffness matrix
$\mathbf{K_a}$	Added stiffness matrix
$\mathbf{K_\tau}$	Stiffness matrix due to the mooring cable's tension
$\mathbf{K_s}$	Stiffness matrix due to the mooring cable's material
k	Wave number
$k^{(i)}$	ith mooring cable stiffness per one meter
$\overline{KG}$	Distance between CG and SWL
$l^{(i)}$	Length of ith mooring cable.
$\mathbf{M}$	Mass matrix
$\mathbf{M_a}$	Added mass matrix
M_y	Moment around y-axis
m_{ii}	Total mass in the ith DOF
P	Translation position vector
$\boldsymbol{r}$	Position vector
R	Transformation matrix
t	Time
T	Water wave period
$\mathbf{T}_i$	Mooring cable's tensions
$\boldsymbol{u}^{(i)}$	Unit vector along ith mooring cable
$\mathbf{U}$	Modal matrix
$\boldsymbol{V_p}$	Velocity of the moving platform's centroid.
W	Weight
λ	Wave length
ω	Angular frequency
ω_n	Natural Frequency
$\boldsymbol{\omega_p}$	Angular velocity of the moving platform.

ξ_i	Damping coefficient in the ith DOF
$\boldsymbol{\psi}$	Base coordinate frame
ψ	Roll Angle
θ	Pitch Angle
φ	Yaw Angle
$\boldsymbol{\Gamma}$	Moving coordinate frame
$\alpha^{(i)}$	Angle between $\boldsymbol{u}^{(i)}$ and z' axis at point $A^{(i)}$
$\gamma^{(i)}$	Angle between the projection of $\boldsymbol{u}^{(i)}$ on the $x'y'$plane and the x' axis at point $A^{(i)}$
$\bar{\boldsymbol{\tau}}$	Mooring cable's pre-tension vector
Ω	Mooring cable stiffness vector
ϵ_m	Neumann's number

DISSERTATION ABSTRACT (ENGLISH)

Full Name : Mamon Mohammad AbedAlqader Horoub

Dissertation Title : Motion of a Floating Cable-driven Platform

Major Field : Mechanical Engineering

Date : March, 2016

In this study, an efficient universal mathematical model is developed to study the dynamics of floating cable driven/moored platforms (FCDPs). The model is based on establishing the mass, stiffness, and damping matrices of the FCDP as functions of the platform position. The current research embraces the kinematic and dynamic analysis of two types of FCDPs in marine environments. These are: a floating movable cylindrical platform (FMCP), and a movable spar platform (MSP). In both of these platforms, variable length mooring cables are controlled by reel/motor devices mounted on the floating structure of the platforms. An experimental study is conducted in a small basin to study the floating cylindrical platform in a static fluid environment to verify the developed mathematical model of the FCDPs.

For the sake of generality, the floating structure has a cylindrical geometry with six degrees-of-freedom and it is connected to the seabed by a mooring system. The floating platforms are subjected sea wave forces, in addition to the buoyancy force. The main purpose of the analysis is to identify conditions that keep the mooring cables taut when the FCDP is exposed to environmental loads. Thus, an effective area is defined as the set of all locations in which the floating structure can be at without losing the mooring cable tensions. Degree of rigidity of the FCDPs is checked within their effective area. Measures

such as the minimum natural frequency, minimum mooring cables' tensions, and minimum submerged depth are used to assess FCDP mobility and degree of rigidity.

RMS values of tensions in the mooring cables, as well as of displacement, velocities, and accelerations of the floating structure of FCDP are obtained for various cases of mooring system strengths and mooring system pre-tensions. The dynamic response of the FCDP with one or two mooring cables failure is investigated. Finally, the influence of the mooring system configuration on the effective area of MSP is studied.

DISSERTATION ABSTRACT (ARABIC)

ملخص الرسالة

الاسم: مأمون محمد عبدالقادر حروب

عنوان الرسالة: سير المحطة البحريه العائمة المتحركة باستخدام الحبال.

التخصص:الهندسة الميكانيكية

تاريخ التخرج: 1437 هـ - (مارس 2016 م)

تم تطوير نموذج رياضي عام يستخدم لدراسة المحطات البحريه العائمة[1], و يستند هذا النموذج على تأسيس مصفوفات الوزن، التخميد، والمرونه و التي تعتمد قيمها على موقع المحطة. لقد تمَّ دراسة نوعين من المحطات البحرية العائمة، وهي: المحطة الإسطوانية العائمة المتحركة، ومحطة السبار المتحركة[2]، ويركز هذا البحث في دراسة هذين النوعين من المحطات باستخدام حبال متغيرة الاطوال والتي يتم التحكم بها بواسطة المحركات المثبته على الجزء الطافي من المحطات. بعد ذلك، تم اجراء دراسة تجريبية في حوض صغير لدراسة نموذج مصغر للمحطة الاسطوانية العائمه دون وجود قوى خارجية تؤثر على المحطة، وتهدف هذه الدراسة إلى التحقق من فعالية النوذج الرياضي المطور.

حيث يتم دراسة حركة المحطات بوجود القوى الخارجية مثل الرياح والأمواج البحرية. والمحطات العائمة عبارة عن شكل اسطواني باستطاعته التحرك بِحُرِّيَّة في ستة اتجاهات مختلفه. الهدف الاساسي من هذه الدراسة هو تحديد الظروف التي تحافظ على أن تكون الحبال مشدودة عندما تتعرض الى القوى الخارجية. وبالتالي، تم إجراء مراحل مختلفة من التحليل على المحطات البحرية العائمة، منها: حساب المساحة الفعَّالة والتي تعرف بالمساحة التي يمكن للمنصات أن تتحرك بداخلها دون فقدان خاصية شد الحبال، كما تم دراسة استقرار المحطات داخل المساحة الفعّالة، وتحليل مقدار

---

(1) – المحطات البحريه العائمة: محطات تستخدم في استكشاف واستخراج البترول.

(2) – السبار: نوع من المحطات البحرية العائمة التي تستخدم في استخراج البترول وتعتمد في استقرارها على الحبال.

الشد المسبق الذي يجب تزويده للحبال داخل المساحة الفعَّالة من أجل المحافظة على استقرار المحطات وتوازنها عند تعرضها للقوى الخارجية، ومن وجهة أخرى تم دراسة تاثير زيادة أو نقصان القوى الداخلية للحبال الناتجة عن تغير الشد المسبق، أو الناتجة عن تغيير الخصائص الداخلية للمادة الأساسية التي تُصنَع منها الحبال.

بالإضافة إلى دراسة تأثير قطع الحبال على فعالية المحطات و توازنها بوجود تأثير القوى الخارجية، كما شمل هذا البحث دراسة تأثُّر المساحة الفعَّالة للمحطات بتغيير نقاط اتصال الحبال بالجزء الطافي من المحطات وقعر البحار.

CHAPTER 1

OFFSHORE PLATFORMS

1.1 Introduction

Offshore platforms are huge structures which are used for different purposes, such as generating electricity, transportation, prospecting, and extracting oil and gas from marine environments. They are designed to work in harsh environments.

In the global oil and gas industry, the primary resources of oil and gas are the onshore and offshore reservoirs, at shallow water depths. For future energy supplies, exploring new reservoirs is essential in difficult environments, such as deep-water situations. In deep-water exploration, there are a lot of challenges, and the technology related to offshore oil and gas industry has developed rapidly for extracting oil and gas from ultra-deep water.

The traditional fixed-base offshore structures are considered unsuitable to face the challenges of the deep-water environment. This is primarily due to different constraints such as installation, technical aspects, and the cost of fabrication. In deep water, alternative innovative platforms have been developed, such as spar platforms. The spar platforms are moored to the seabed using conventional mooring cables that can be a taut mooring system or a catenary mooring system.

Floating marine platforms are key structures for offshore oil and gas exploration and production, particularly, in deep seas. These platforms' operations depend on the harmonious management of a mooring system. Mooring cables (the mooring system) are used to anchor the platform to the seabed. They also restore the floating platform's

position when it is exposed to loads caused by environmental conditions and rig operations.

In all cases, offshore platforms constitute two parts: a semi-submerged structure, and mooring cables connected to the seabed. Offshore platforms however, have certain limitations [1, 2], one of which is their inability to change their horizontal position on the sea surface. Therefore, this study explores the idea of using adaptable mooring cables (through reel/motor arrangement on the floating structure) to move these floating platforms along the sea surface for the purpose of developing moving offshore platforms (Floating Cable-Driven Platform, FCDP), see Figure 1.1.

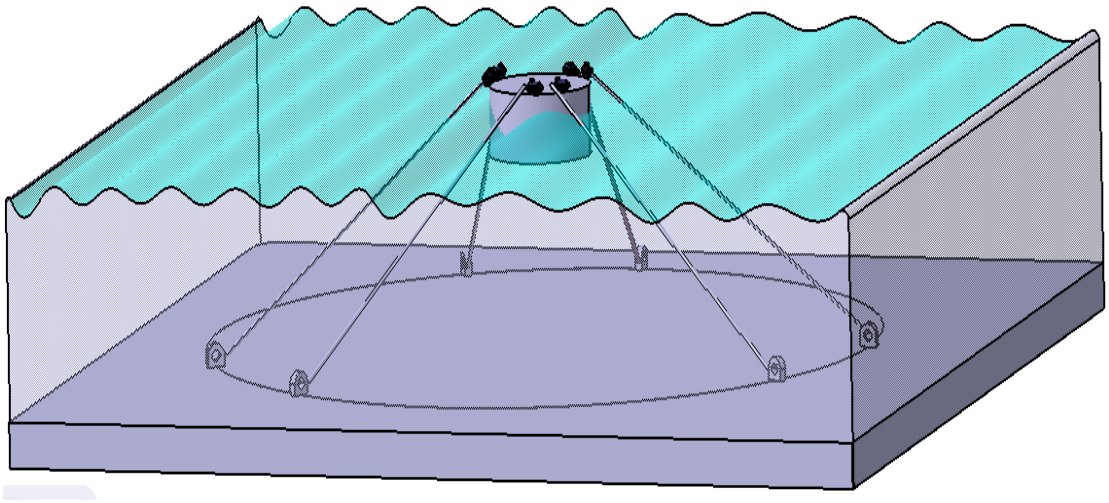

Figure 1.1: General floating cable-driven platform (FCDP).

In the following sections, different types of offshore platforms are discussed and classified depending on their flotation, water depth and their structures.

1.2 Offshore Platforms

Depending on the requirements, offshore platforms can be classified as either a floating platform or a platform fixed to the seabed. They can be operated in different water levels, which is from 60 to 3700m [3].

The following are the widely used offshore platforms, see Figure 1.2:

- Fixed offshore platforms.
  - Conventional fixed platforms,
  - Compliant towers.
- Floating offshore platform.
  - Semi-submersible platform,
  - Sea star platform,
  - Tension leg platforms,
  - Spar platforms,
  - Offshore wind power.

These platforms are used to store onsite processing equipment and provide accommodation for the people who work on them.

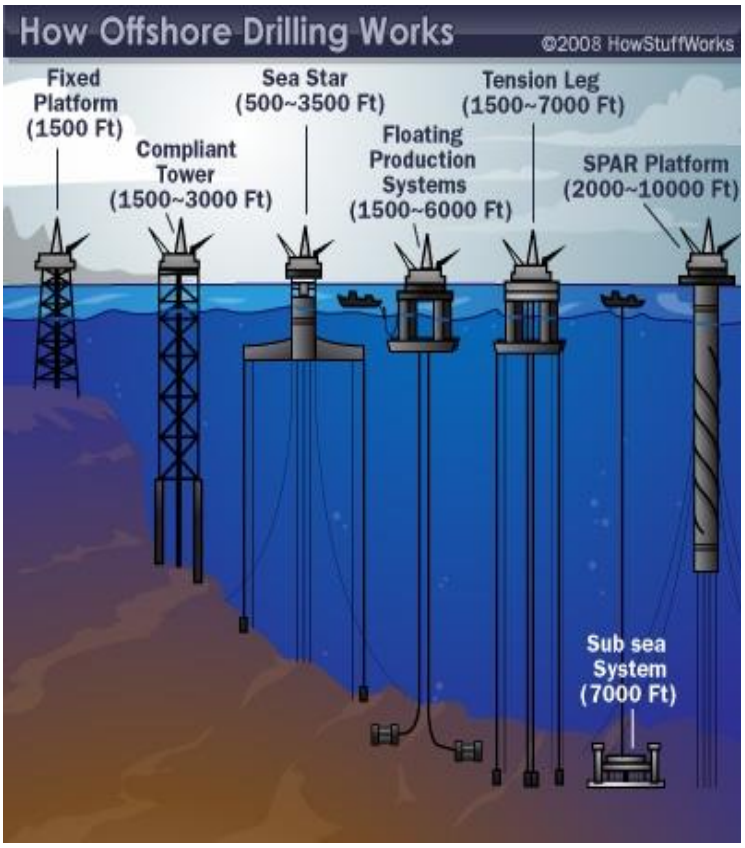

Figure 1.2: Different types of offshore platforms [4].

A fixed platform is one of the types of platforms that are used for oil and gas production. These platforms are fixed directly to the seabed with concrete and/or steel legs. They can be held in place by mooring cables, steel legs, and giant anchors.

1.2.1 Conventional Fixed Platform

Concrete or large steel legs are used to fix the platforms directly to the seabed. These types of platforms contain space for onsite processing and facilities for the crew. These platforms are designed to have a long lifespan, and they are extremely stable. Fixed platform can be used in depths up to 520 m, see Figure 1.3.

Figure 1.3: Fixed platform [5].

1.2.2 Compliant Towers

These towers are an updated version of the fixed platform and are designed based on the basic idea of fixed platforms. Concrete and steel towers of these platforms are narrower than the fixed platforms, giving them more flexibility. This flexibility in their design allows the platforms to move laterally with the forces that are generated from the wind and sea waves and currents. These towers can operate in depths ranging from 457 to 914 m, see Figure 1.4.

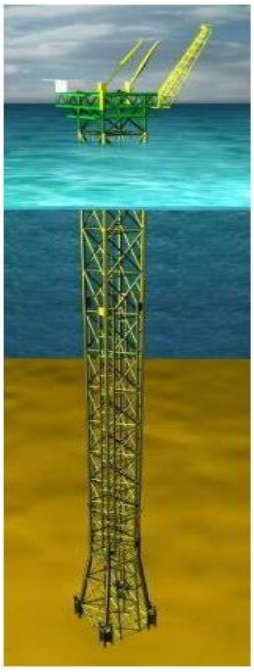

Figure 1.4: Compliant tower [5].

1.2.3 Semi-submersible Platform

Depending on the requirements, semi-submerged platforms can be moved from one place to another at any time. They are held in place using the principal of dynamic positioning, with the help of giant anchors. These types of platforms can operate in depths ranging from 60 to 3000 m, see Figure 1.5.

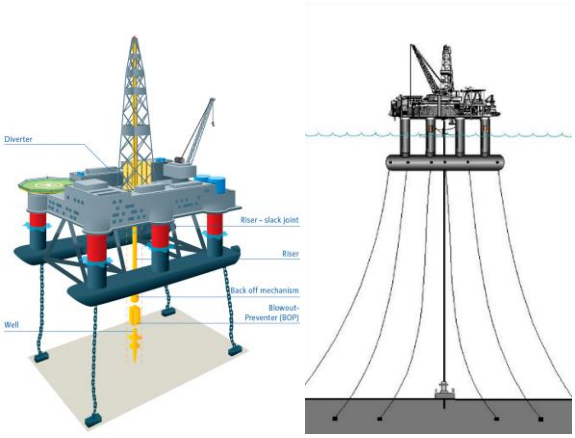

Figure 1.5: Semi-submersible Platform [6].

1.2.4 Sea Star Platform

These platforms are a modified design of the semi-submersible version. They have flexible steel legs, instead of anchors, which are used to connect the platform to the seabed. The range of the water depths that these platforms operate in is 152 to 1067 m, see Figure 1.6.

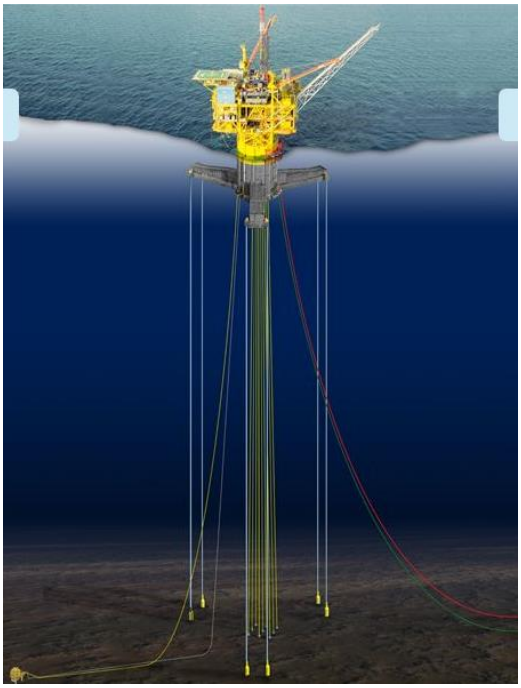

Figure 1.6: Sea Star Platform [5].

1.2.5 Tension Leg Platforms

The tension leg platform (TLP) is considered one of the floating platform types. TLPs are offshore stations that are used to explore for oil in deep water. They are fixed by mooring cables anchored to the seabed, which means that the tension legs extend from the seabed to the platform itself. The TLPs can operate in water depths up to 2134 m, see Figure 1.7.

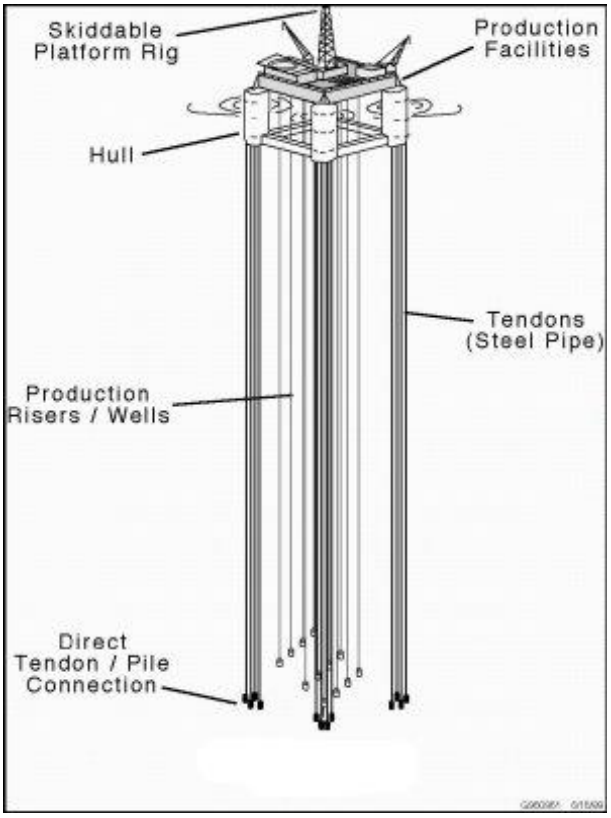

Figure 1.7: Tension Leg Platforms [7].

1.2.6 Spar Platforms

A huge hollow cylindrical hull is the base of this type of platform. This base is connected with another cylinder end which descends to a water depth of 213 m. The weight of the cylinder allows the platform to stay in place, which provides more stability to the system. Mooring cables/chains are used to connect the cylinder with the seabed. The working water depth of spar platforms is up to 3048 m.

There are three main types of spar platforms: classic, truss, and cell spar platforms. The main parts of the spar platform are a hard tank, a mid-section (cylinder, truss or heave plates), and a soft tank as shown in Figure 1.8.

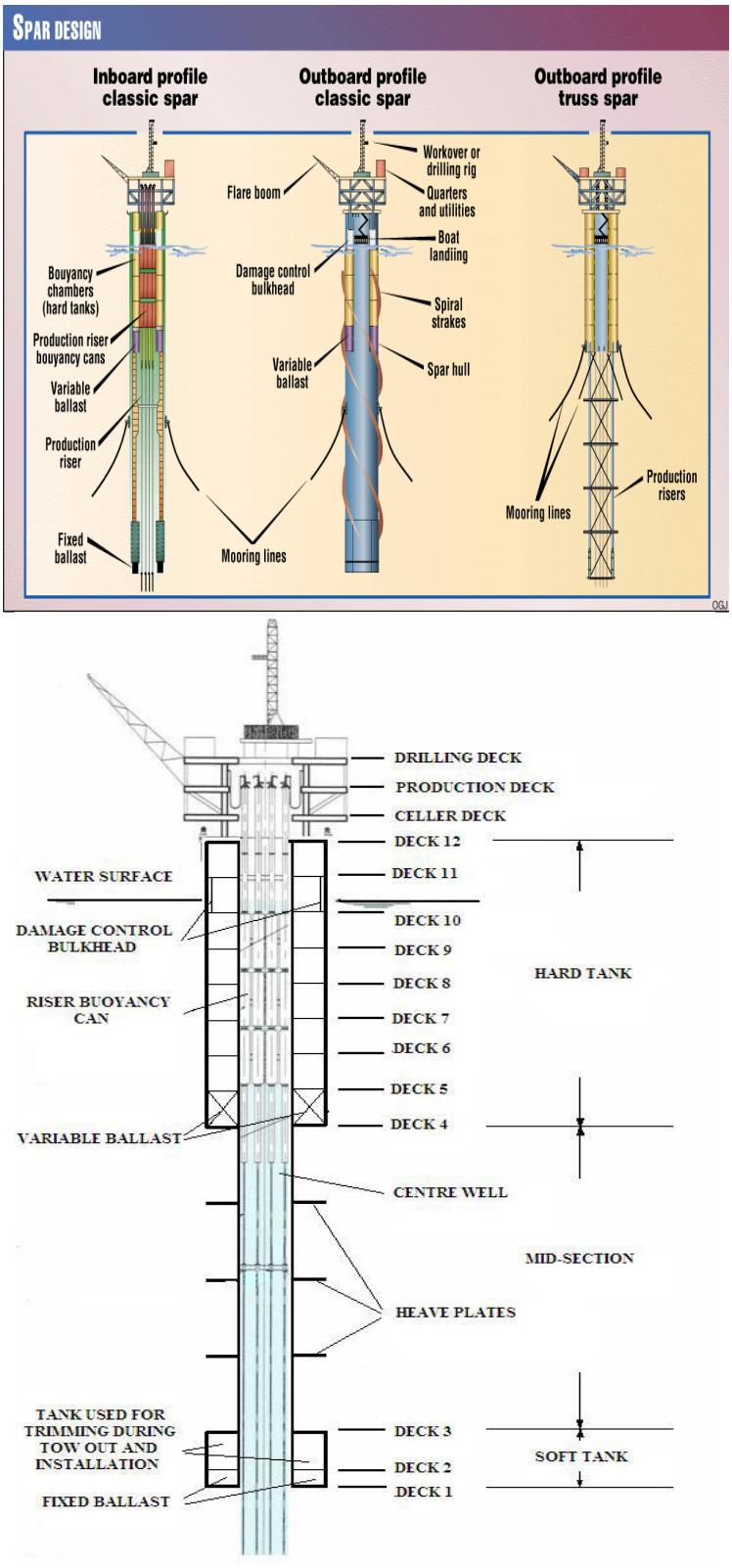

Figure 1.8: Spar platforms (up) classic and truss spar [8], (down) Cell spar [9].

Spar platforms are connected to the seabed like TLP platforms, but the difference between them is that TLPs have vertical tension mooring cables, whereas spar platforms have more conventional mooring cables. The spar platforms have more ingrained stability than TLPs due to the large counterweight at the bottom of spar platforms. Also, spar platforms do not depend on the mooring cables to hold it upright. Further, spar platforms have the ability to adjust their horizontal position by changing the mooring cable tensions, using chain-jacks which are connected between the mooring cables and the seabed anchors.

1.2.7 Offshore Wind Power (Turbine)

Offshore wind power is designed to generate electricity from wind. Floating wind turbines are the major type of offshore wind power in deep-water areas, see Figure 1.9.

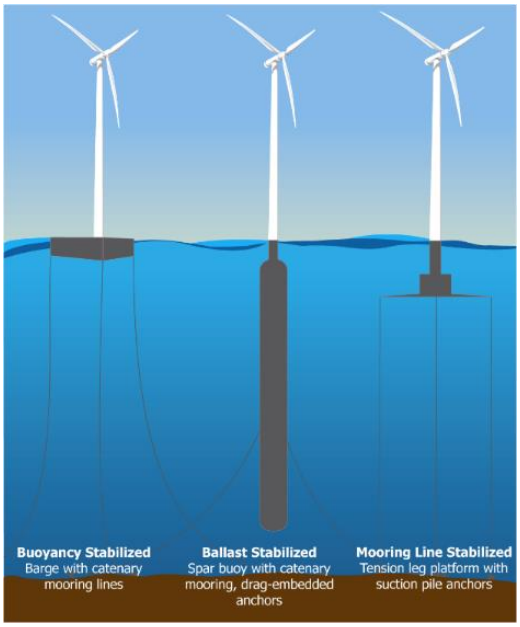

Figure 1.9: Offshore wind turbines [10].

1.3 Floating Cable-Driven Platform (FCDP)

In all cases, offshore platforms consist of two parts: a semi-submerged structure and a mooring system that is used to anchor the platforms to seabed. Offshore platforms however, have certain limitations [1, 2], one of which is their inability to change their horizontal position on the sea surface. Therefore, this study explores the idea of using adaptable mooring cables (through a reel/motor arrangement on the floating structure) to move these floating platforms along the sea surface for the purpose of developing moving offshore platforms. The new system's name is formulated as the floating cable-driven platform (FCDP); see the following figure which represents a general floating cable-driven platform, see Figure 1.10.

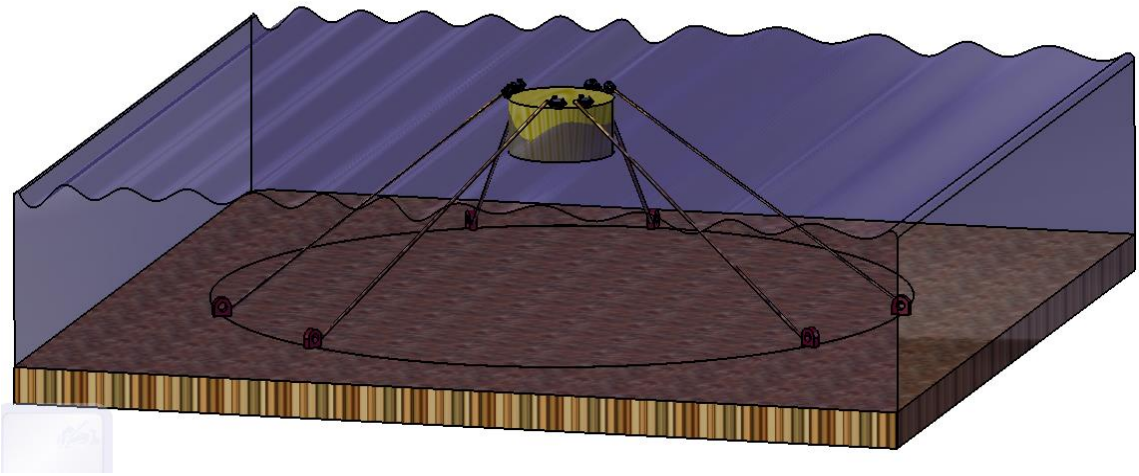

Figure 1.10: General floating cable-driven platform (FCDP).

CHAPTER 2
LITERATURE REVIEW

2.1 Introduction

In this chapter, related research on the aspects of the dynamic analysis of floating offshore platforms is discussed. These studies are categorized into three general research directions, which are spar platforms, mooring cables, and sea water waves.

2.2 Literature Review

Floating marine platforms are key structures for offshore oil and gas exploration and production, particularly, in deep seas. These platforms' operation depends on harmonious management of the mooring cables (the mooring system). Mooring systems are used to anchor the platform to the seabed. They also restore the floating platforms' stability when it is exposed to marine environmental loads. Spars are floating marine platforms; they are moored to the seabed, with conventional mooring cables that can be a taut mooring system or a catenary mooring system.

Understanding the dynamic behavior of floating marine platforms is critical for their design and operation. Predominantly, rigid body dynamics has been employed, which consider the floating marine platform as a rigid body having six degrees of freedom. The floating platform motion can be divided into horizontal platform dynamics (surge, sway, and yaw motions), which occur at the water wave frequency, and vertical platform dynamics (heave, roll, and pitch), which occur at high frequencies.

The important previous studies, on spar platforms, mooring cables and sea water waves are reported in the following sections.

2.2.1 History of Spar Platforms

Shell's Brent spar was the first large spar in the oil industry. It was installed in the North Sea in the 1970's and it was used for oil storage and offloading [11, 12]. Although further research was conducted by some oil companies on the spar concept, no other spar platforms were constructed until 1996, when Neptune was anchored in the Gulf of Mexico at a depth up to 590 m. Hunter et al. [13] described a turn-key drilling spar which was developed for the Gulf of Mexico. This spar platform was also used for production.

Several papers discussed the analysis, behavior, and design of spars [11, 14]. Among these studies, Glanville et al. [15] introduced the details of the installation, construction and concept of a spar platform. They concluded that the needed of flexibility in the selection of well oil systems and its drilling strategies can be addressed using the spar platform.

Several spar concepts reviewed by Horton and Halkyard [14] emphasized the platform's design aspect. Berteaux [16] presented general analysis procedures and designs for subsurface and surface buoys. Also, he presented analysis procedures and designs for spar buoys. It should be noted that the spar platform concepts have not been limited to deep water applications or to drilling and/or production systems exclusively.

The French Bouee Laboratoire I [16] and the Marine Physical Laboratory MPL [17] are laboratories for the measurement of spar-types that can be deployed at any depth of water. However, this is limited by their drafts when they are in their upright positions. These platforms have stability in the heave and pitch directions in the most common sea states.

A cost-effective spar buoy flare (SBF) system has been designed by Korloo [18]. Large quantities of gas are remotely flared off by an SBF system from a fixed offshore production platform 150 m away. The SBF was fabricated, designed and installed in a water depth of 65 m.

Research on spar platforms began during the 1990s. Since that time, many numerical and experimental studies have been implemented to investigate the dynamic characteristic response of spar platform. Most of the early numerical studies were applied to a classic spar platform, which is the first generation of spar. Extensive experimental work was conducted to validate these studies, through the Joint Industry Project (JIP) spar by Johnson [19] at the Offshore Technology Research Center (OTRC). At the wave frequency, the spar buoy responses are small, even when near the spectrum peak frequency, but are relatively large when near the natural frequencies [20, 21].

The second order diffraction theory [22, 23] has been used to compute the second order wave loading on the platforms. As an example, the JIP spar motions were calculated by Ran et al. [24] using the higher order boundary element method (HOBEM) [25]. Several nonlinearities, such as computations in the instantaneous displaced position, nonlinear drag damping, and wave drift damping were considered. The linear wave body interaction theory was found to be inadequate when used alone. For the reliable prediction of spar platform, the second order wave body interaction theory had to be used.

In deep water, the behavior of a spar was studied by Johnson et al. [26] and Mekha et al. [27, 28]. In their work, they used the Morison equation to investigate the sea wave forces and they considered the effect of several second order and wave kinematics. They also

inspected the effect of neglecting the hydrodynamic forces acting on the mooring cables by modeling them as nonlinear springs. They used bichromatic, regular and random waves in their work to predict the response. Then they compared the results with the experimental data to see the effect of each individual second order on the spar response. In these studies, they neglected the second order temporal acceleration.

The slender body approximation method proves to be an attractive analysis tool for a spar when it is subjected to various environmental conditions. This was shown by a work of Chitrapu et al. [29] concerned with the nonlinear response of a spar under different environmental conditions like regular/random waves and current. This study was conducted using a time domain simulation model. Several nonlinear effects could be considered in the model. The Morison equation was used to find the hydrodynamic forces and moments. Reliable prediction of platform response was obtained when the Morison equation is used, with accurate prediction of kinematics of wave particles and the calculations of force in the displaced position of the spar platform.

A study by Xu et al. [30] of truss spar motions based on the full slender body formulation incorporating all nonlinear terms was conducted. For this purpose, a code written in MatLab was developed by extending the code for a classic spar. Satisfactory agreement was achieved between the predicted results and limited experiment results. In addition, different simplified methods for estimating the forces on the truss section and the hard tank were studied. It was found that only the full slender body formulation led to reasonable results.

The forces and wave kinematics acting on a spar platform can be found by various approximation methods. The difference between these methods were investigated by Anam and Roesset [31]. In this study, three approximation methods were considered, those being the hybrid wave, stretching and extrapolation model.

A method for resolving incident free-wave components from wave elevations measured around a spar offshore platform was discussed in [32]. The importance of this method was proven by a comparison between full scale measurements of motions for the Moomvang Truss spar and the analytical predictions. Particular attention was given to the wave frequency response. Results revealed an excellent match between the measured and analytically predicted spar response when the measured waves were inserted into the numerical model.

In [33], two models have been used to study the spar motion response in the direction of the wave environment. These two models are a directional hybrid wave model (DHWM) and a unidirectional hybrid wave model (UHWM). Several numerical results have been conducted from these two models and the comparisons between the results indicated that the slow drifting motion in surge direction and pitch direction are slightly smaller in DHWM than those based on UHWM. In the heave direction, the slow drifting using the two models was almost the same, and the reason for the motion in the heave direction was mainly dependent on the pressure applied on the bottom of the spar structure. This pressure made almost no difference in the two models.

Chitrapu et al. [34] used a large diameter spar platform to study the motion response, using a time domain simulation model, in the presence of a current and random directional waves.

They considered several nonlinearities for determining the motion response. These nonlinearities were the displaced position force computation, the free surface force calculation, and the effect of wave current interaction and nonlinearities in the equation of motion. They studied the spar response in the surge and pitch direction due to the effect of wave directionality. They concluded that there is a significant effect on the predicted response for both the wave energy directional spread and the interaction of wave-current.

Results from a study by Leira et al. [35] on the analysis of the dynamical response of a spar platform subjected to wave and wind forces were presented. The motions were considered in surge and pitch directions. Anam [36] studied the differences between time domain analysis and frequency domain analysis in predicting the spar slow drift responses using the Morison equation.

Lake et al. [37] investigated three possible configurations of TLP/spar platforms and the results demonstrated that the addition of a disk to the base of the column can enhance the damping, but does little to increase the added mass. Separating the disk and cylinder nearly doubles the added mass and increases the damping ratio by 58 percent over the attached cylinder disk platform, and increases an impressive 344 percent over the single column.

Prislin et al. [38] experimentally studied the variation of added mass and damping of both a single plate and multi plate arrangement for a spar platform. The effect of the vertical column was not included. The results showed that the coefficient of drag of an oscillating plate is dependent on the Reynolds number. At a higher Reynolds number, the drag coefficient does not vary significantly with the Reynolds number, and it is significantly lower than the drag coefficient measured at a lower Reynolds number.

Magee et al. [39] discussed the application of a squared plate to a truss spar. The experimental results and numerical predictions showed that square plates significantly help to reduce the heave response of a truss spar. It was also observed that the loads on the square plates can be predicted accurately by using the Morison equation. The heave damping augmentation effect on the heave behavior of a classic spar was studied experimentally by Fischer and Gopalkrishnan [40].

The importance of heave damping augmentation for spars, and the possibility of achieving this augmentation via the use of circular plate sections protruding from the spar hull, were studied. The tests had two main goals: one was to determine whether more than one plate could be added with an effect, and the other to find the optimum spacing between plates for more than one plate. The results showed that, with a number of damping plates, each additional plate increased the total damping; however, the largest increase was achieved with the first plate added to the cylinder. With respect to the optimum spacing between two plates, the results showed that the optimum spacing was approximately one cylinder diameter; a further increase in spacing does not significantly increase the damping.

The effect of different types of heave plates on the dynamic response of a truss spar platform was studied experimentally by Downie et al. [41]. Four types of plates were used in the experiment. Two of them were perforated (large and small) and two were solid (large and small). It was found that, over most of the considered range, the heave response was smaller for the spar platform with the larger and solid plates than for those with perforated and smaller plates. This was because of the large added masses of the large and solid plates compared to the small and perforated ones. This led to lower natural frequencies far removed from the resonant behavior and the peak wave energy.

An alternative solution to increase the viscous damping of a classic spar in the vertical direction is to change the hull shape. A study by Tao et al. [42] investigated different alternative hull shapes prolocationd by Haslum and Faltinsen [43] in reducing the heave resonant response. Based on potential theory, a hydrodynamic software package called SESAM [44] was used to calculate the added mass, the wave forces and radiation damping. The Navier-Stokes equation was used, based on the finite difference method, to calculate the nonlinear viscous damping in the heave direction. It was concluded that the use of alternative hull shapes reduced the resonant response in the heave direction and this was done by increasing the damping mechanism. This was achieved by keeping the natural period of heave response direction outside the range of wave energy.

To assess the importance of the wave drift damping and viscous forces to be included in the dynamic analysis of spar platforms, Alok et al. [45] predicted, analytically, the spar buoy platform's response motion and compared the analytical results with experimental ones. The North Sea and the Gulf of Mexico's extreme wave conditions were used in their study. Their numerical model considered nonlinear diffraction loads, linear stiffness and damping characteristics of a spar platform with a multi-degree-of-freedom model. Also, the effect of the viscous forces was studied for the spar platform. The predicted results were used to improve the model test results.

An experimental study was performed by Lim et al. [46] to study the cell spar platform motion characteristics. During the experiments it was observed that the pitch response motion, at a certain time range, became unstable. It was thought that due to the nonlinearity, the kinetic energy was transferred from the heave direction mode to the pitch direction mode. The predictions of numerical results, apart from the unstable time range of the pitch

motion, agreed well with the experimental results. Agarwal and Jain [47] studied the spar platform's nonlinear coupled dynamic response under regular sea waves, and modeled the mooring cable as a nonlinear horizontal and vertical spring located at the fairleads along the spar center.

Some cell spar model basin tests by Finn et al. [48] indicated that multiple cells, forming a column, can be less susceptible to water vortices when the spacing between cells permits interstitial flow of water through their spaces. The effect of heave plates was experimentally conducted on the cell spar platform hydrodynamic response performance by Zhang et al. [49].

A new model combined variations of the cell spar concept with several heave plates and a truss section at the lower part of the spar were modeled and tested. Different design aspects of the heave plates were modeled by changing the types and the shapes of the plates. The newest spar configuration is the cell-truss spar. This new concept was introduced by the State Key Laboratory of Ocean Engineering (SKLOE) in Shanghai Jiaotong University (SJTU), intending to take advantage of two spar types: the typical truss spar and the cell spar. A nonlinear time domain dynamic coupled analysis program, called SESAM (developed by DNV software), was used by Zhang et al. [50] to investigate the global performance and mooring cable tensions of the new spar concept. A basic test with a 1:100 scale model was also conducted in a wave basin at SKLOE to calibrate the numerical approach. It was found that the new model configuration has the same advantages of its first spar generations and its motions could be restricted in a satisfactory region. As the research on cell-truss spar was being conducted in SKLOE at SJTU, the new concept was subjected to numerous studies. Based on the hybrid model testing technique, a model test

of a cell-truss spar was conducted by Su et al. [51]. The numerical predictions measurements agreed well with the experimental data. In addition to the preceding studies on cell-truss spars at SJTU, a comparison between three numerical schemes have been performed for a cell-truss spar by Zhang et al. [52]. These three schemes are a time domain semi-coupled analysis, a fully-coupled analysis, and a frequency domain analysis. The aim of these comparisons was to find the applicability of the different approaches to predict the motions and mooring cable tensions for a cell-truss spar.

A new type of spar platform, named an S-spar, was presented by Yu and Huang [9]. Its midsection is a cylinder with the same diameter as the center well. The center well and midsection was designed as an integrated structure. Heave plates are attached appropriately along the connection section. With the unique midsection, the S-spar is suitable for operating in the special oceanic environment and ultra-deep water depths in the South China Sea. The structural design and hydrodynamic analysis for this structure were discussed. Detailed motion analysis results showed that the platform offers excellent motion characteristics, and is optimized to carry large payloads in ultra-deep water. Finally, the effect of potential and viscous damping in different region was analyzed.

Jameel et al. [53] presented a study to idealize a spar mooring integrated system as a fully and strongly coupled system. As well, they studied the effect of the damping on mooring cables and the importance of the coupling effect on a spar platform. Montasir et al. [54] investigated the effect of symmetric, as well as asymmetric, mooring configurations on the dynamic responses of the truss spar platforms.

2.2.2 Mooring Cables

There are different possible designs of mooring cable systems which are used for wave energy converters (WECs,) and those designs have been discussed by Harris et al. [55]. This discussion focused on the mooring cable anchors, components and configurations. Nielsen and Binding [56] illustrated two different mooring cable configurations: a taut leg mooring system and a conventional catenary mooring system as shown in Figure 2.1.

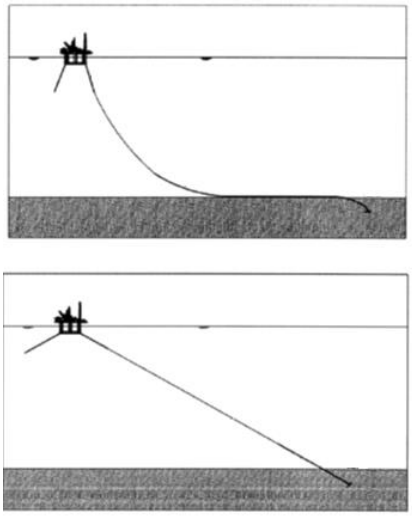

Figure 2.1: Examples of mooring cable systems: Top-catenary mooring cable; Bottom-taut mooring cable (fiber rope).

Indeed, there are three possible configurations of mooring cables system, given in Figure 2.2. The traditional configuration of a mooring cable is the catenary form. By increasing the water depth, the weight of the mooring cable increases and this increase affects the downward catenary angle at the platform which increases the required buoyancy. As a result, the installation cost increases. On the other hand, a light weight mooring cable eliminates these problems. Therefore, fiber rope is used as a light weight mooring cable; it extends from the platform down to the seabed anchor point as a taut line, and thus is called a taut mooring cable.

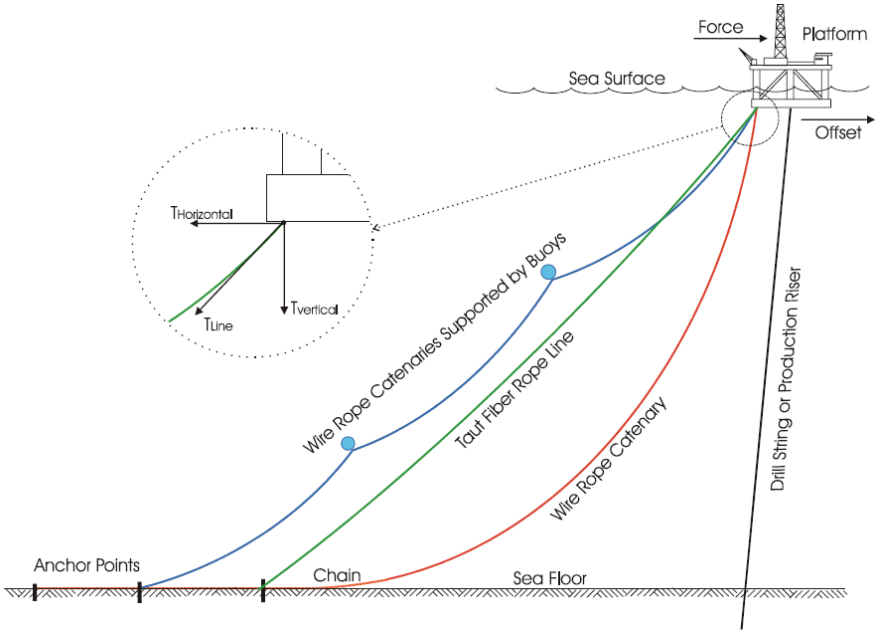

Figure 2.2: Catenary and taut mooring cable [57].

The weight of the taut mooring cable is much less, and this feature reduces the downward pull force on the platform; thus, the buoyancy which is needed to carry the platform can be less.

Gao and Moan [58] discussed different types of mooring cables which are used for floating platform structures, including catenary mooring cable and taut mooring cable systems, as shown in the Figure 2.3. In addition, buoys can be used and attached to mooring cables system to increase the buoyancy force in the mooring cables.

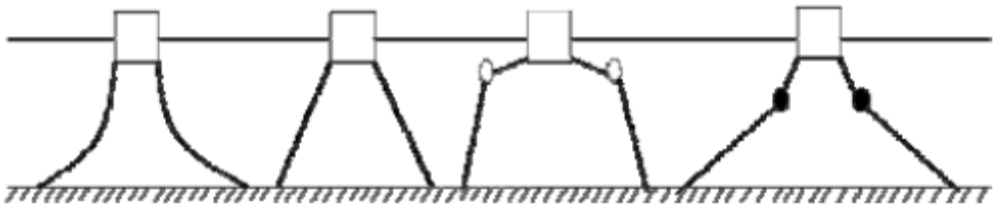

(a) (b) (c) (d)

Figure 2.3: Different types of mooring cable systems. (a) catenary mooring cable (b) taut mooring cable (c) taut mooring cable with buoys and (d) taut mooring cable with clump weights.

Ridge et al. [59] carried out an analysis to compare between a taut mooring cable and a catenary mooring cable. This comparison depended on the cost and the mass of several lines (catenary and taut) with different arrangements, and they included several different anchor configurations in their analysis.

Ji et al. [60] studied the merits and demerits of a taut mooring cable system and a modified catenary taut mooring cable system, which is a new system integrating the taut with the catenary mooring cable. They form a catenary shape at the end of the taut mooring cable, as shown in Figure 2.4, using some clumped masses.

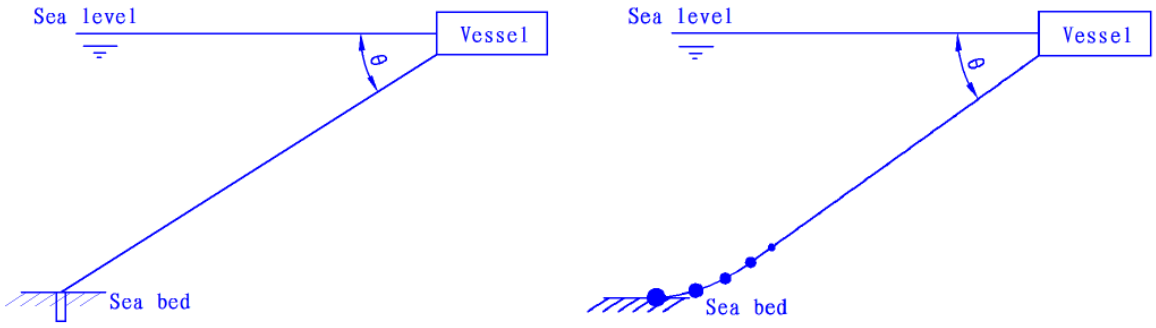

(a) (b)

Figure 2.4: Mooring cable system (a) traditional taut mooring cable (b) the new catenary taut mooring system.

Ricii et al. [61] studied and analyzed an integrated mooring system that was used for wave energy arrays. They noted some advantages of using taut mooring cable systems, such as the benefit of having a small size of footprint and large stiffness.

Weller et al. [62] discussed the mooring cable types and they mentioned the key advantage of fiber ropes, which are used as taut mooring cable, over a chain mooring cable is their relatively low cost. Also, they mentioned that the taut mooring cable requires less tension to keep the platform in its position, as the following figure shows, and this result is due to its light weight.

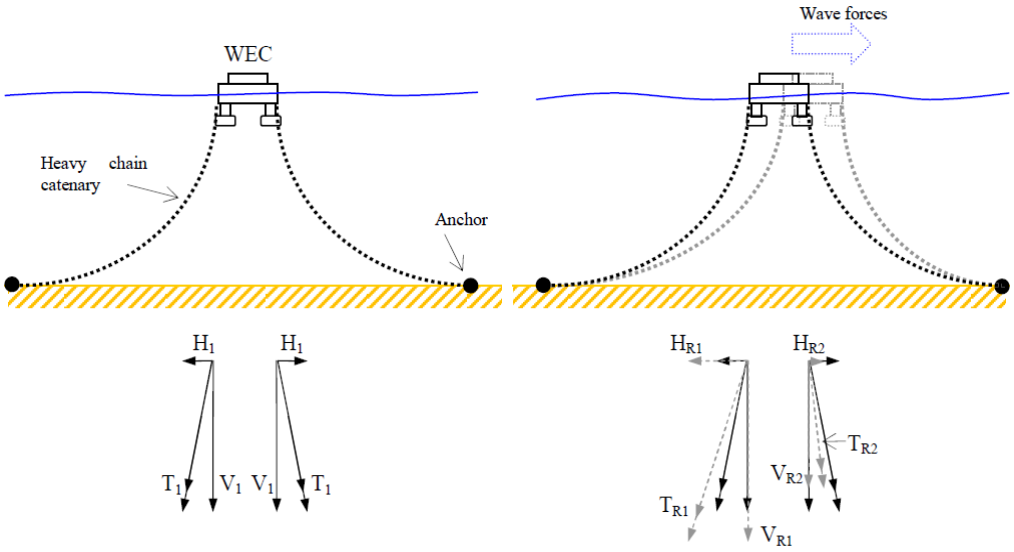

(a) A heavy catenary mooring cable requires a high tension.

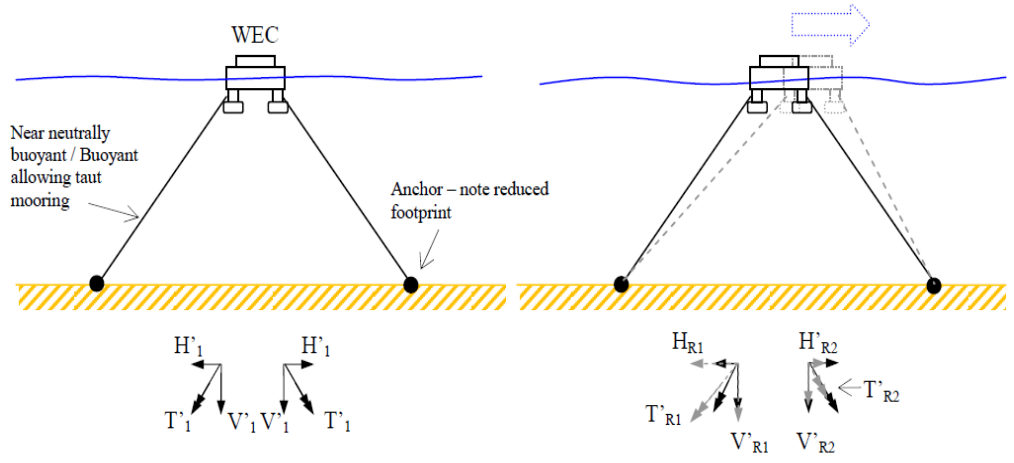

(b) A light taut mooring cable requires a low tension

Figure 2.5: Diagram showing difference between taut and catenary mooring cables [62].

2.3 Sea Waves

The assumptions that a fluid is in-viscid and incompressible are used to develop the water wave theory. In addition, there are many assumptions which are: a wave is periodic, a wave motion is irrotational and a wave is uniform in time.

The water wave depends on different parameters such as water depth (d), height of the water wave (H) or water wave amplitude (A), wavelength (λ) or wavenumber (k), water wave velocity (C), water wave period (T) or water wave angular frequency (ω).

If the regular water wave is periodic, then the following equation can be used:

$$C = \frac{\lambda}{T} \tag{2.1}$$

Under the force of gravity, the surface gravity waves propagates faster with an increasing wavelength. For a certain wavelength, waves in shallower water have a lower phase speed than those in deeper water. The water waves' generalized dispersion relation is represented in the following equation [63]:

$$\omega^2 = kg \tan(kd) \tag{2.2}$$

The important parameters that describe the water waves are their height, time period (see Figure 2.6), and the water depth over which they are propagating. Other quantities, like water wave velocity and acceleration, can be determined theoretically from the wave height and the wave time period quantities.

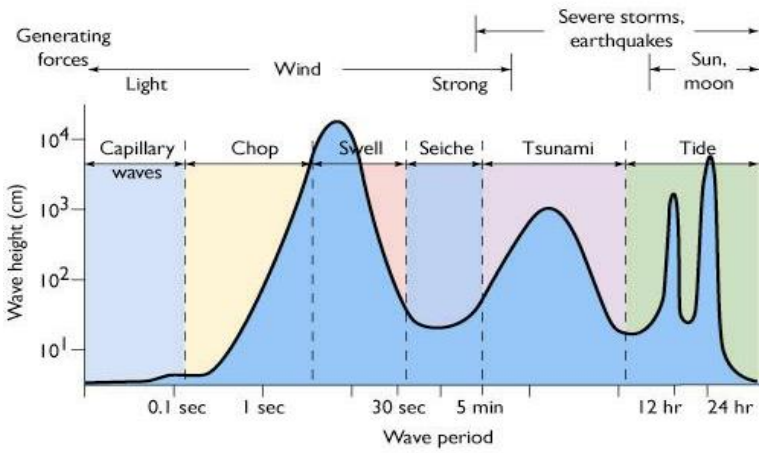

Figure 2.6: Idealized Wave Spectrum [64].

Table 2.1 and Figure 2.7 represent the important parameter values of the sea waves used in this study; the parameters were taken from several studies conducted on sea waves in the Arabian Gulf [65-67]:

Table 2.1: Arabian Gulf sea wave parameters.

Parameters	H (m)	$T\ (sec)$	$d\ (m)$
Values	1	5	50

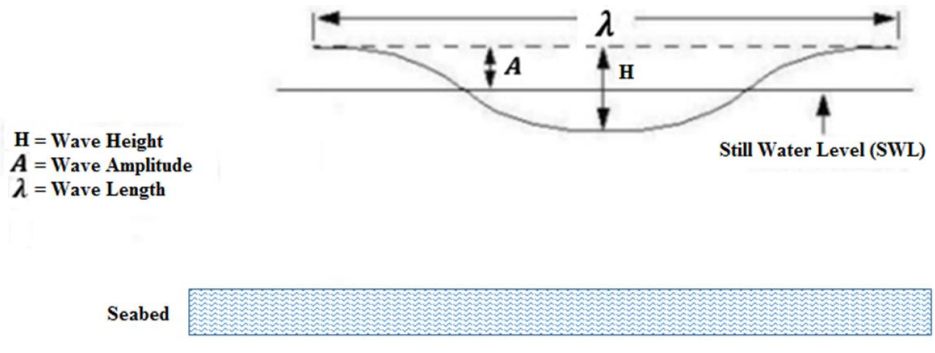

Figure 2.7: Water Wave Parameters.

2.4 Research Objectives

This dissertation attempted to study and enhance the effectiveness of the floating platforms in marine environments. The general objectives of this dissertation are

- Introducing a concept of adaptable mooring cables, through reel/motor devices arrangement on the floating structure in marine environment, and come up with a general approach to describe the kinematics and dynamics of any floating cable driven/moored platforms (FCDPs) in a static and wavy water environment.
- Establishing the mass, stiffness, and damping matrices of FCDPs as a function of the platform position, estimate the offshore environmental loads. Finding the solution for the equation of motion of the FCDPs, and conducting an experimental study to verify the developed mathematical model of the FCDPs dynamics.
- Studying the kinematic and dynamic analysis of two types of FCDPs in marine environments. These are: a floating movable cylindrical platform (FMCP), and a movable spar platform (MSP).
- Checking the degree of rigidity and mobility (minimum natural frequency and minimum submerged depth) of the FCDPs within their effective area.
- Investigating the effect of mooring system strengths, mooring system pre-tensions, and mooring cables failure on the dynamic performance of the FCDPs.

2.5 Scope of the Study

Understanding the dynamic behavior of FCDPs is critical for their design and operation. Predominantly, rigid body dynamics has been employed, considering the FCDP as a single rigid body having six degrees of freedom. The FCDP motion can be divided into the translation platform dynamics (surge, sway, and heave motions) and the rotational platform dynamics (roll, pitch and yaw). All figures and tables present the fluctuation of the platform's dynamic response.

Different assumptions are considered in the analysis.

- Water is incompressible, inviscid, and it has a constant density and temperature.
- Water waves are unidirectional and the motion is irrotational.
- Water waves have a small amplitude compared to their wave length.
- Damping coefficients ξ_i are assumed to be small due to the slow motion.
- Motor positions are assumed to be on (u, v) plane at the center of gravity.
- The number of mooring cables/bundles should equal the number of degrees of freedom to have a fully constrained platform in the sea [68].
- Offshore platform risers are not considered.
- A taut mooring cable is considered.
- Linear springs are used to represent the mooring cables' restoring force.

- The Jacobean matrix should be nonsingular for any marine platform configuration.

2.6 Dissertation Organization

This dissertation is divided into seven chapters as follows:

- **Chapter 1: Introduction:** It provides a general introduction about the topic.
- **Chapter 2: Literature Review:** This provides a general literature review on topics related to spar platforms, mooring cables and sea waves. The literature review is followed by dissertation research objectives, then a dissertation organization.
- **Chapter 3: Mathematical Analysis:** From mathematical mode, the mass, stiffness, and damping matrices of floating marine platforms as a function of the platform position are obtained. Also, the offshore environmental loads are estimated. Finally, the solution for the equation of motion of the FCDPs is reported and discussed.
- **Chapter 4: Analysis of Floating Movable Cylindrical Platform:** This chapter presents the static and dynamic analysis of the floating movable cylindrical platform, followed by an analysis of the effective area and degree of rigidity. A parametric study is carried out on the change of mooring cable stiffness and pre-tension.
- **Chapter 5: Experimental Study:** In this chapter, an experimental study is conducted to verify the developed mathematical model of the FCDPs.
- **Chapter 6: Analysis of Movable Spar Platform:** This chapter presents the dynamic analysis of the movable spar platform followed by an analysis of the

effective area and degree of rigidity. Failure analysis is discussed when a failure of the mooring cables occurs. The influence of the mooring cable configuration on the MSP dynamic response is investigated.

- **Chapter 7: Conclusions and Recommendations:** This chapter provides the main conclusions and followed by recommendation for future work.

CHAPTER 3

Mathematical Analysis

3.1 Introduction

Equations of motion of floating cable-driven platforms (FCDPs) consist of the mass, stiffness, and damping matrices, and force vector. In this study, time domains have been used to find the FCDP dynamic' response in the considered degrees of freedom.

Taut mooring cables are used to connect the FCDP to the seabed. These mooring cables contribute to the FCDP's motion by providing restoring forces to restrain the system. The taut mooring cables' contribution to the damping is assumed to be small and can be neglected, so, the taut mooring cables are modeled as linear springs.

In section 3.2, the frame of references and the degree of freedom of the FCDP are described in detail. Section 3.3 describes the degree of rigidity of the submerged object in terms of center of buoyancy and center of gravity.

Mass matrix is treated in Section 3.4. Strip theory and the flat disk approach are used to find the added mass matrix. Section 3.5 represents the damping matrix of the FCDP. In this study, the structural damping is considered, while the damping that comes from the mooring cables is assumed to be negligible.

Section 3.6 treats the stiffness matrix as three parts. The first part is due to the mooring cables' strength, the second part is due to the mooring cables' tension, and the third part is

due to the water effect (added stiffness). In this section, the manipulators concept (the Jacobean concept) is used to find the stiffness matrix.

The forces which act on the FCDP are discussed in Section 3.6, followed by rigid dynamic analysis in Section 3.7. This is followed by an analytical solution, which is adopted to predict the FCDP motion response.

Finally, the effective area of a FCDP on a sea water surface is discussed in Section 3.9, followed by a global analysis (Section 3.10). Degree of rigidity analysis, in terms of minimum natural frequency, is treated in Section 3.11.

The FCDP is analyzed within the context of rigid body dynamics. Hence, the governing equation of the motion is

$$\mathbf{M}(\mathbf{x})\,\ddot{\mathbf{x}} + \mathbf{C}(\mathbf{x})\,\dot{\mathbf{x}} + \mathbf{K}(\mathbf{x})\,\mathbf{x} = \mathbf{F}(\mathbf{x}, \mathrm{t}) \tag{3.1}$$

where $\mathbf{x} = [x \quad y \quad z \quad \psi \quad \theta \quad \varphi]^T$ is a vector of displacements. While surge (x), sway (y), heave (z) represent the translation motion, roll (ψ), pitch (θ) and yaw (φ) represent the Euler rotation angles between the fixed and the movable Cartesian frames of reference. $\mathbf{F} = [F_x \quad F_y \quad F_z \quad M_x \quad M_y \quad M_z]^T$ is the force and moment vector applied on the platform. $\mathbf{M}(\mathbf{x})$, $\mathbf{C}(\mathbf{x})$, and $\mathbf{K}(\mathbf{x})$ are the inertia, damping, and stiffness matrices of the movable platform at the location **x,** respectively. Dots in Equation (1) represent differentiation with respect to time. The inertia, the damping and the stiffness matrices should be calculated at each location, the platform presents at. $\ddot{\mathbf{x}}$ and $\dot{\mathbf{x}}$ represent velocity and acceleration vectors, respectively.

3.2 Frame of References and DOF

Understanding the dynamic behavior of FCDPs is critical for their design and operation. Predominantly, rigid body dynamics are employed, and the FCDP is considered as a single rigid body having six degrees of freedom under the loads of sea waves.

The FCDP motion can be divided into the horizontal platform dynamics (surge, sway, and yaw motions), which occur at the water wave frequency, and the vertical platform dynamics (heave, roll, and pitch), which occur at height frequencies, as shown in Figure **3.1**

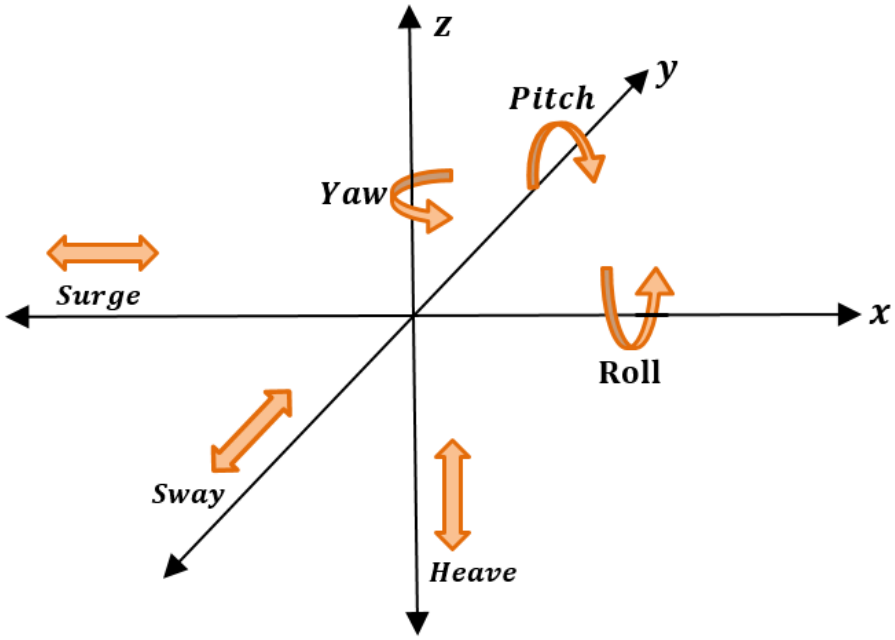

Figure 3.1: Degree of freedom of the FCDP.

The parameters and frames of reference of the FCDP are depicted in Figure **3.2**. The FCDP is assumed to work in a sea with mean water depth of d, and its submerged depth is b. A fixed Cartesian frame of reference **ψ**(X, Y, Z) is located at the center of an imaginary circle on the seabed. All mooring cables are anchored to the seabed at points $A^{(i)}$ which are located on the imaginary circle perimeter. A movable Cartesian frame of reference

$\boldsymbol{\Gamma}$(u, v, w) is located at the center of gravity (CG) of the floating cylindrical structure of the FCDP. All mooring cables are driven by sets of reel-motor devices, which are hosted at points $B^{(i)}$ which are positioned on the (u,v)-plane. The translation position vector **p**, with respect to the fixed frame **ψ**(X, Y, Z), represents the distance and the direction between the fixed and the moving Cartesian frames of the FCDP. In the following formulations, all the vectors will be defined with respect to the fixed frame.

$\boldsymbol{u}^{(i)}$is a unit vector along the ith mooring cable , $i = 1,\cdots,n$, from its attachment point $A^{(i)}$ to point $B^{(i)}$. Vector $\boldsymbol{e}^{(i)}$ is a unit vector in the direction from the moving platform center point to the attachment point $B^{(i)}$.

Euler angles ($\psi, \theta, and\ \varphi$) have been used to represent the angles at which the moving structure is oriented with respect to the fixed frame **ψ**(X, Y, Z) and $\beta^{(i)}$ are angles have been used to represent the orientation of vector $\boldsymbol{e}^{(i)}$ with respect to the u axis in the uv plane. Vector $\boldsymbol{a}^{(i)}$ is the position vector of point $A^{(i)}$; $b^{(i)}$is the length of the line between the moving platform center point and the attachment point $B^{(i)}$, and $l^{(i)}$ is the length of ith mooring cable.

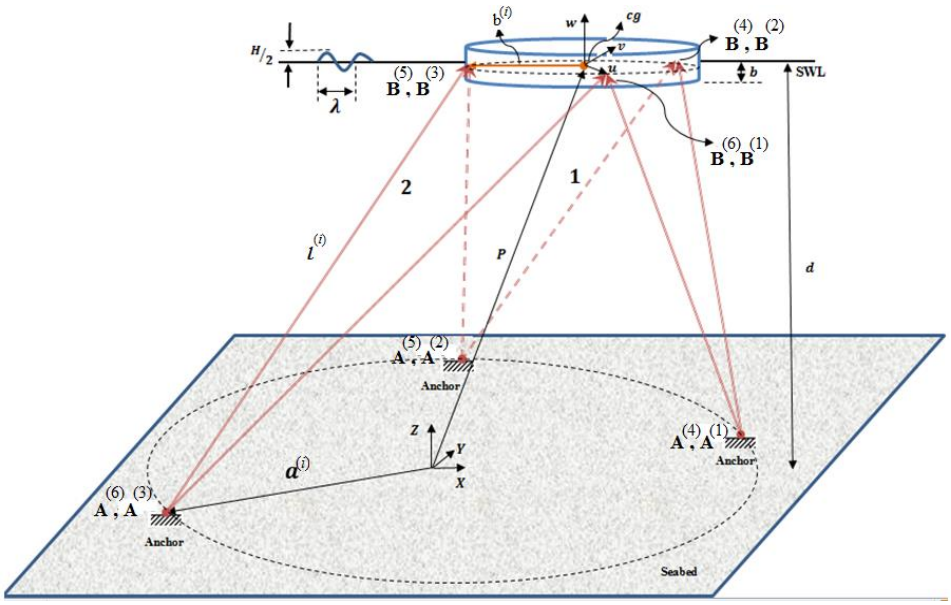

(General schematic)

.

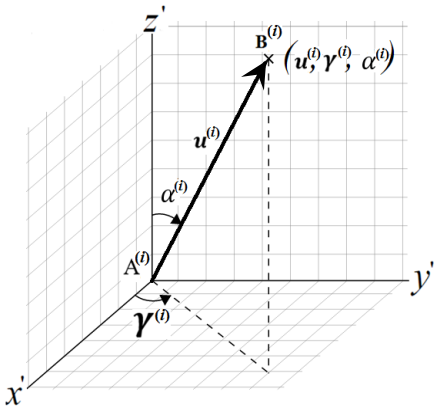

(Mooring cable direction)

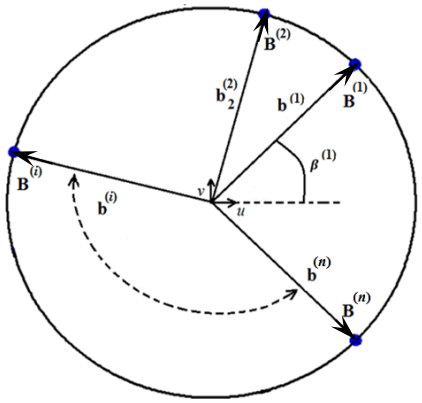

(Top view of moving structure)

Figure 3.2: Coordinates and variables for the FCDP.

3.3 Center of Buoyancy and Center of Gravity

The center of buoyancy (CB), $(\bar{x}_{CB}, \bar{y}_{CB}, \bar{z}_{CB})$, is known as the point at which the buoyancy force acts on the body and this center is equivalently the submerged portion's geometric center of the body.

$$\bar{x}_{CB} = \frac{M_x}{V} \tag{3.2}$$

$$\bar{y}_{CB} = \frac{M_y}{V} \tag{3.3}$$

$$\bar{z}_{CB} = \frac{M_z}{V} \tag{3.4}$$

where

$$M_x = \int x_c \, dV$$

$$M_y = \int y_c \, dV$$

$$M_z = \int z_c \, dV$$

$$V = \int y \, z \, dx = \int x \, z \, dy = \int x \, y \, dz$$

V: is the submerged volume.

The center of buoyancy changes dependent on the volume of the submerged portion of the platform. As a platform rolls, pitches and yaws, the center of buoyancy moves according to the "new" shape of the submerged platform.

The center of gravity (CG), $(\bar{x}_{CG}, \bar{y}_{CG}, \bar{z}_{CG})$, is known as the point at which the weight force acts on the body and is equivalently the body's geometric center.

$$\bar{x}_{CG} = \int x_c \, dm \tag{3.5}$$

$$\bar{y}_{CG} = \int y_c \, dm \tag{3.6}$$

$$\bar{z}_{CG} = \int z_c \, dm \tag{3.7}$$

where m is the platform mass.

A platform metacenter is known as the intersection between the two lines of action of the buoyancy force. Basically, when a platform rolls with an angle, θ, the center of buoyancy changes as shown in Figure 3.3. It is known that, as the buoyancy direction is always vertical, there is a point at which the two lines of action for the different center of buoyancy must cross. This point is known as the metacenter of the platform, denoted by MC as illustrated in Figure 3.3.

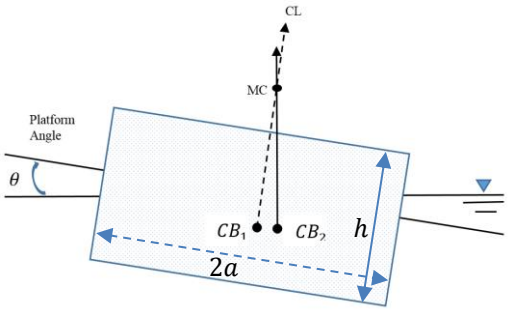

Figure 3.3: The metacenter with the buoyancy force.

The distance between the center of buoyancy and the metacenter ($\overline{BM}$) can be found using the following equations:

$$\overline{BM} = \frac{I}{V_d} \tag{3.8}$$

$$\overline{MC} = CB + \overline{BM} \tag{3.9}$$

where $I = \frac{1}{12}h(2a)^2$ is the transverse moment of inertia of the platform's water plane about its own centerline (CL) and V_d is the platform's displaced volume.

Equation 3.10 represents the distance between the CG and the MC, known as the metacentric height ($\overline{GM}$). Metacentric height is the distance measured from the metacenter to the center of gravity. The platform is stable if the metacentric height is positive; however, the platform is unstable if the metacentric height is negative. If the metacentric height is large, then the platform is considered to be "stiff" in roll – indicating that there will be a

large righting moment as a result of small roll angles. In contrast, if the metacentric height is small then the platform rolls due to a small moment.

$$\overline{GM} = MC - CG \tag{3.10}$$

3.4 Mass Matrix

In the case of floating cable-driven platforms, the mass matrix consists of two inertial components: (i) The structural mass matrix and (ii) The hydrodynamic mass matrix (known as the added mass matrix).

3.4.1 Structural Mass Matrix

The structural mass matrix is a diagonal matrix with components that are lumped for each platform degree of freedom.

$$\mathbf{M}_s(\mathbf{x}) = \begin{bmatrix} m_1 & 0 & 0 & 0 & 0 & 0 \\ 0 & m_2 & 0 & 0 & 0 & 0 \\ 0 & 0 & m_3 & 0 & 0 & 0 \\ 0 & 0 & 0 & I_4 & 0 & 0 \\ 0 & 0 & 0 & 0 & I_5 & 0 \\ 0 & 0 & 0 & 0 & 0 & I_6 \end{bmatrix} \tag{3.11}$$

where the subscripts 1, 2,…, 6 refer to the six degrees of freedom: surge, sway, heave, roll, pitch and yaw, respectively. $m_{i,\ i=1,2,3} = \pi\rho_f ba^2$ is the total mass of the floating structure, $I_4 = \frac{1}{12}m(3a^2 + h^2)$ is the total principal axis floating mass moments of inertia about the x-axis, $I_5 = \frac{1}{12}m(3a^2 + h^2)$ is the total principal axis floating mass moments of inertia about the y-axis, $I_6 = \frac{1}{2}ma^2$ is the total principal axis floating mass moments of inertia about the z-axis, and h is the height of the platform (from the top to the bottom of the floating structure).

3.4.2 Added Mass Matrix

The hydrodynamics mass matrix (added mass matrix) represents the fluid domain around the floating structure of marine platform which puts additional inertia on the movable floating platform. The strip theory, as described by Faltinsen [69] and Newman [70], is used to obtain the added mass coefficients in the surge and sway directions. Additionally, the flat disk approach, which is presented by Mansouri et al. [71], is applied to find the added mass coefficient in the heave direction.

Figure 3.4 represents a floating structure of a FCDP. For a general case, the center of gravity has been assumed assumed to be under the floating structure. $\overline{KG}$ is the distance from the center of gravity (CG) of the floating structure to the still water level (SWL); C_a is the added mass coefficient which depends on the body shape (shown in Figure 3.4); a is the radius of the floating structure, and ρ is the water density.

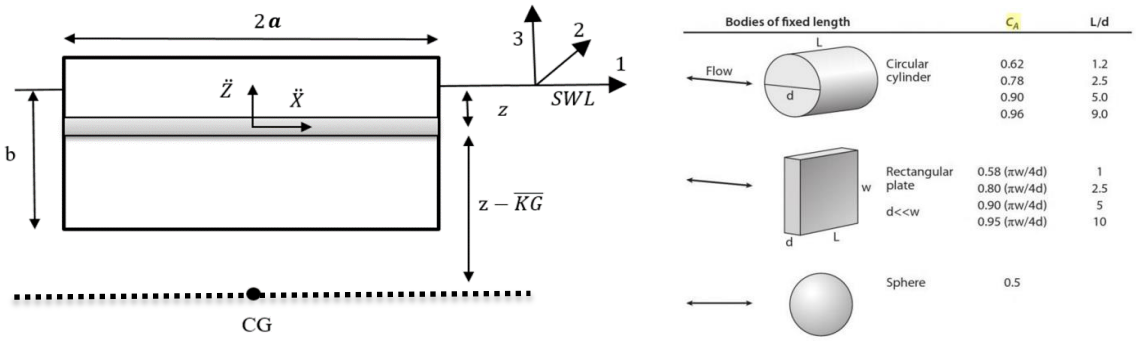

(a) (b)

Figure 3.4: Cylindrical floating structure (a) local coordinates and variables (b) the added mass coefficient for different shapes [72].

For the purpose of compactness, the notations 1-6 refer to the degrees of freedoms of surge, sway, heave, roll, pitch and yaw respectively.

Using strip theory, the added mass force in the surge direction (F_{11}) is given as

$$F_{11} = \int_{-b}^{0} \pi C_a \rho a^2 d_z . \ddot{X} \tag{3.12}$$

Therefore, the added mass is given as

$$m_{11} = \pi C_a \rho a^2 b \tag{3.13}$$

In the heave direction, the added mass becomes, using the flat disk approach [71],

$$m_{33} = \frac{4}{3} \rho a^3 \tag{3.14}$$

The cable-driven marine platform is a vertical and symmetrical body, therefore:

$$F_{13} = F_{31} = 0 \tag{3.15}$$

$$m_{13} = m_{31} = 0 \tag{3.16}$$

To obtain the added mass in the pitch direction, strip theory has been used.

$$F_{51} = -\int_{-b}^{0} \pi C_a \rho a^2 (z - \overline{KG}) dz . \ddot{X} \tag{3.17}$$

$$F_{51} = \pi C_a \rho a^2 b (\overline{KG} + {}^{b}/_{2}) \ddot{X} \tag{3.18}$$

Therefore, the added mass is given as

$$m_{51} = \pi C_a \rho a^2 b (\overline{KG} + {}^{b}/_{2}) \tag{3.19}$$

The floating cable-driven platform is a vertical and symmetrical body, therefore:

$$F_{53} = F_{35} = 0 \tag{3.20}$$

$$m_{53} = m_{35} = 0 \tag{3.21}$$

On the other hand, the same criteria is used to find m_{15}

$$dF_{15} = -\pi C_a \rho a^2 (z - \overline{KG}) dz \, \ddot{\theta} \tag{3.22}$$

Therefore, the added mass is given as

$$m_{15} = \pi C_a \rho a^2 b(\overline{KG} + {}^{b}/_{2}) \tag{3.23}$$

The added mass of the platform in the pitch direction is as follows:

$$dF_{55} = -dF_{15}(z - \overline{KG}) \tag{3.24}$$

Therefore,

$$dF_{55} = \pi C_a \rho a^2 (z - \overline{KG})^2 dz\, \ddot{\theta} \tag{3.25}$$

Therefore, the added mass is given as

$$m_{55} = \pi C_a \rho a^2 (\frac{b^3}{3} + \overline{KG}^2 + \overline{KG} b^2) \tag{3.26}$$

When using previous analytical methods for evaluation of the components of the added mass matrix, one needs to pay attention to the following facts [73]:

(i) The inertial force in the x- and y-directions of a floating circular cylindrical structure are equal. (ii) The mass moment about the x-axis is also equivalent to that about the y-axis, therefore the added mass in the sway direction is equal to the added mass in the surge direction. Hence, the added mass related to the sway direction is given as

$$m_{22} = m_{11} = \pi C_a \rho a^2 b$$

$$m_{44} = m_{55} = \pi C_a \rho a^2 (\frac{b^3}{3} + \overline{KG}^2 + \overline{KG} b^2)$$

$$m_{23} = m_{13} = 0$$

$$m_{32} = m_{31} = 0$$

$$m_{24} = m_{15} = \pi C_a \rho a^2 b(\overline{KG} + {}^{b}/_{2})$$

$$m_{42} = m_{51} = \pi C_a \rho a^2 b(\overline{KG} + {}^{b}/_{2})$$

$$m_{34} = m_{35} = 0$$

$$m_{43} = m_{53} = 0$$

All other added masses are equal to zero because the FCDP is vertical and symmetrical. Hence, the final added mass matrix of the FCDP is

$$\mathbf{M}_{\boldsymbol{a}}(\mathbf{x}) = \begin{bmatrix} m_{11} & 0 & 0 & 0 & m_{15} & 0 \\ 0 & m_{22} & 0 & m_{24} & 0 & 0 \\ 0 & 0 & m_{33} & 0 & 0 & 0 \\ 0 & m_{42} & 0 & m_{44} & 0 & 0 \\ m_{51} & 0 & 0 & 0 & m_{55} & 0 \\ 0 & 0 & 0 & 0 & 0 & 0 \end{bmatrix} \tag{3.27}$$

3.5 Damping Matrix

Marine structures, in general, are influenced by structural and hydrodynamic damping. While structural damping emanates from the composition of the marine platform, hydrodynamic damping is due to two factors, which are the radiation and the viscosity. While the evaluation of the damping matrix can be done using the strip theory as implemented by Incecik [74], it is noted that several researchers [47, 54, 75-77] have adopted a diagonal damping matrix with the following form:

$$\boldsymbol{C}(\mathbf{x}) = \begin{bmatrix} C_{11} & 0 & 0 & 0 & 0 & 0 \\ 0 & C_{22} & 0 & 0 & 0 & 0 \\ 0 & 0 & C_{33} & 0 & 0 & 0 \\ 0 & 0 & 0 & C_{44} & 0 & 0 \\ 0 & 0 & 0 & 0 & C_{55} & 0 \\ 0 & 0 & 0 & 0 & 0 & C_{66} \end{bmatrix} \tag{3.28}$$

where

$$C_{11} = 2\xi_{surge}\omega_{n\,surge}m$$

$$C_{22} = 2\xi_{sway}\omega_{n\,sway}m$$

$$C_{33} = 2\xi_{heave}\omega_{n\,heave}m$$

$$C_{44} = 2\xi_{roll}\omega_{n\,roll}I_{44}$$

$$C_{55} = 2\xi_{pitch}\omega_{n\,pitch}I_{55}$$

$$C_{66} = 2\xi_{yaw}\omega_{n\,yaw}I_{66}$$

m is the total mass of the structural platform,

I_{44} is the total mass moment of inertia about the x-axis,

I_{55} is the total mass moment of inertia about the y-axis,

I_{66} is the total mass moment of inertia about the z-axis.

ξ is the damping ratio in the specified motion direction of the platform, and

ω_n is the natural frequency of the platform in the specified degree of freedom.

3.6 Stiffness Analysis

In floating cable-driven platforms, the stiffness matrix consists of two parts. (i) the mooring cables stiffness matrix, and (ii) the hydrostatic stiffness matrix.

3.6.1 Jacobian Matrix

For the floating cable-driven platform, the Jacobian matrix **J** [78] can be represented as the relationship between the velocity of the moving platform's centroid $[\boldsymbol{V_p}\ \boldsymbol{\omega_p}]^{\boldsymbol{T}}$ and the time changes in mooring cable lengths $\dot{\mathbf{l}}$.

$$\dot{\mathbf{l}} = \mathbf{J}\dot{\boldsymbol{r}} \tag{3.29}$$

where

$\dot{\mathbf{l}} = \left[\dot{l}^{(1)},\ \dot{l}^{(2)}, \ldots, \dot{l}^{(n)}\right]^T$, n: is the mooring cable number, and

$\dot{\boldsymbol{r}} = [\boldsymbol{V_p} \quad \boldsymbol{\omega_p}]^T$.

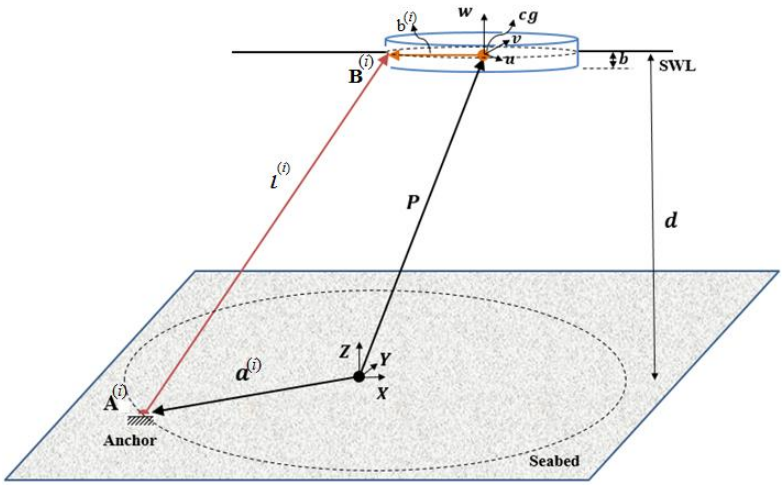

Figure 3.5: The vector loop closure of *i*th mooring cable of the FCDP.

Graphically, as shown in Figure **3.5**, the kinematics of the platform with 6 degrees of freedom (DOF) can be obtained. The vector loop closure of any platform's mooring cable can be written as follows:

$$\mathbf{P} + b^{(i)}\boldsymbol{e}^{(i)} = \boldsymbol{a}_i + l^{(i)}\boldsymbol{u}^{(i)} \tag{3.30}$$

Equation (3.31) can be found by taking the derivative of Equation (3.30) [78].

$$\mathbf{V_p} + \boldsymbol{\omega}_B \times \boldsymbol{b}^{(i)} = l^{(i)}\ \boldsymbol{\omega}^{(i)} \times \boldsymbol{u}^{(i)} + \dot{l}^{(i)}\boldsymbol{u}^{(i)} \tag{3.31}$$

where x means the cross product between the previous vectors. Eliminating $\boldsymbol{u}^{(i)}$, can be done by dot-multiplying both sides of Equation (3.31) with $\boldsymbol{u}^{(i)}$ as follows:

$$\boldsymbol{u}^{(i)} . \mathbf{V}_{\boldsymbol{p}} + \boldsymbol{u}^{(i)} . \boldsymbol{\omega}_B \text{ x } \boldsymbol{b}^{(i)} = \boldsymbol{u}^{(i)} . l^{(i)} \boldsymbol{\omega}^{(i)} \text{x } \boldsymbol{u}^{(i)} + \boldsymbol{u}^{(i)} . \dot{l}^{(i)} \boldsymbol{u}^{(i)} \tag{3.32}$$

Hence,

$$\boldsymbol{u}^{(i)} . \mathbf{V}_{\boldsymbol{p}} + \boldsymbol{b}^{(i)} \text{ x } \boldsymbol{u}^{(i)} . \boldsymbol{\omega}_B = \dot{l}^{(i)} \tag{3.33}$$

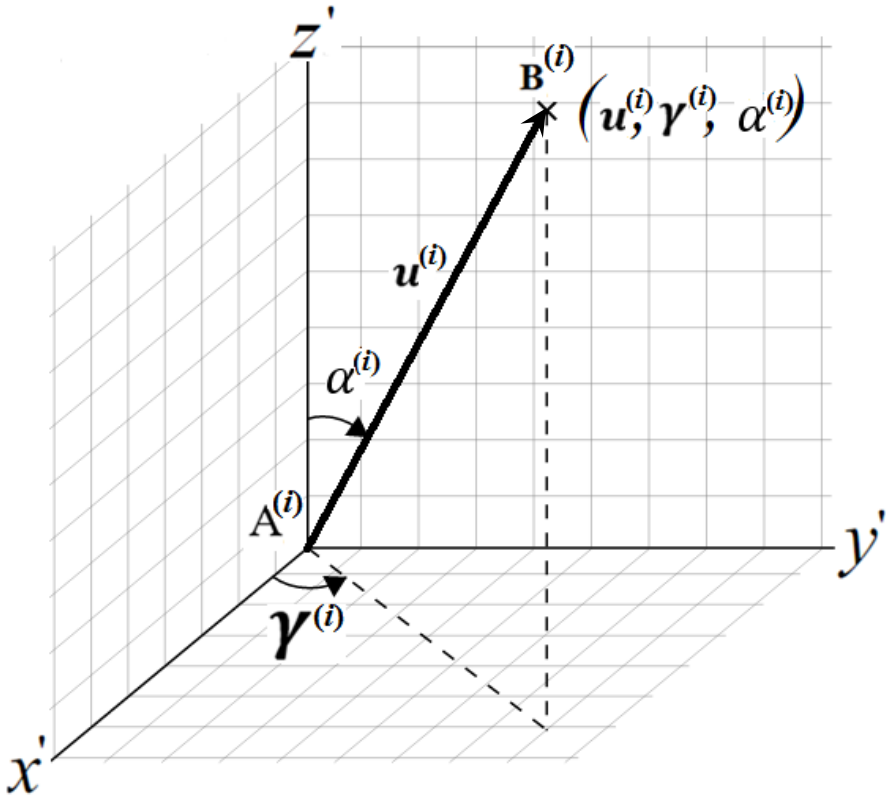

Figure 3.6: Mooring cable's coordinate.

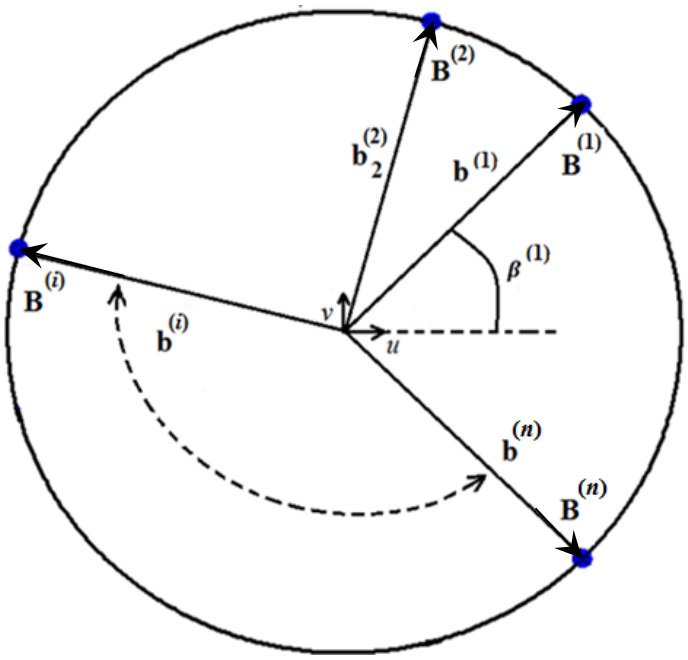

Figure 3.7: Moving structure coordinates.

Using Figure **3.6** and Figure **3.7**, vector $\boldsymbol{u}^{(i)}$ and ${}^{\Gamma}\boldsymbol{b}^{(i)}$ are represented in Equations (3.34) and (3.35)

$$\boldsymbol{u}^{(i)} = \left[\cos\gamma^{(i)} \sin\alpha^{(i)} \quad \sin\alpha^{(i)} \sin\gamma^{(i)} \quad \cos\alpha^{(i)}\right]^{T} \tag{3.34}$$

$${}^{\Gamma}\boldsymbol{b}^{(i)} = b^{(i)} \left[\cos\beta^{(i)} \quad \sin\beta^{(i)} \quad 0\right]^{T} \tag{3.35}$$

Where

$\alpha^{(i)}$ represents the angle between $\boldsymbol{u}^{(i)}$ and z' axis at point $A^{(i)}$, and

$\gamma^{(i)}$ represents the angle between the projection of $\boldsymbol{u}^{(i)}$ on the $x'y'$plane and the x' axis at point $A^{(i)}$.

Equation (3.36) introduce the transformation matrix, using roll (ψ), pitch (θ) and yaw(φ) angles, between the fixed frame and the moving frame [78]. Using Equation (3.35) and (3.36), $\boldsymbol{b}^{(i)}$ is written in terms of the fixed frame as shown in Equation (3.37).

$$ {}^{\Psi}R_{\Gamma} = \begin{bmatrix} \cos\varphi\cos\theta & \cos\varphi\sin\theta\sin\psi - \sin\varphi\cos\psi & \cos\varphi\sin\theta\cos\psi + \sin\varphi\sin\psi \\ \sin\varphi\cos\theta & \sin\varphi\sin\theta\sin\psi + \cos\varphi\cos\psi & \sin\varphi\sin\theta\cos\psi - \cos\varphi\sin\psi \\ -\sin\theta & \cos\theta\sin\psi & \cos\theta\cos\psi \end{bmatrix} \tag{3.36} $$

$$ \boldsymbol{b}^{(i)} = {}^{\Psi}R_{\Gamma}\ {}^{\Gamma}\boldsymbol{b}^{(i)} \tag{3.37} $$

The Jacobian matrix of the FCDP, which is represented in Equation (3.38), can be represented as.

$$ \mathbf{J} = \begin{bmatrix} \boldsymbol{u}^{(1)T} & \left(\boldsymbol{b}^{(1)} \times \boldsymbol{u}^{(1)}\right)^{T} \\ \boldsymbol{u}^{(2)T} & \left(\boldsymbol{b}^{(2)} \times \boldsymbol{u}^{(2)}\right)^{T} \\ \vdots & \vdots \\ \boldsymbol{u}^{(n)T} & \left(\boldsymbol{b}^{(n)} \times \boldsymbol{u}^{(n)}\right)^{T} \end{bmatrix} \tag{3.38} $$

$$ \mathbf{J} = \begin{bmatrix} \mathrm{C}\gamma^{(1)}\,\mathrm{S}\alpha^{(1)}, & \mathrm{S}\alpha^{(1)}\,\mathrm{S}\gamma^{(1)}, & \mathrm{C}\alpha^{(1)}, & C\,\alpha^{(1)}\zeta_2{}^{(1)} + S\,\alpha^{(1)}\,S\,\gamma^{(1)}\zeta_1{}^{(1)}, & \ldots \\ \mathrm{C}\gamma^{(2)}\,\mathrm{S}\alpha^{(2)}, & \mathrm{S}\alpha^{(2)}\,\mathrm{S}\gamma^{(2)}, & \mathrm{C}\alpha^{(2)}, & C\,\alpha^{(2)}\zeta_2{}^{(2)} + S\,\alpha^{(2)}\,S\,\gamma^{(2)}\zeta_1{}^{(2)}, & \ldots \\ \vdots & \vdots & \vdots & \vdots & \ldots \\ \mathrm{C}\gamma^{(n)}\,\mathrm{S}\alpha^{(n)}, & \mathrm{S}\alpha^{(n)}\,\mathrm{S}\gamma^{(n)}, & \mathrm{C}\alpha^{(n)}, & C\,\alpha^{(n)}\zeta_2{}^{(n)} + S\,\alpha^{(n)}\,S\,\gamma^{(n)}\zeta_1{}^{(n)}, & \ldots \end{bmatrix} $$

$$ \begin{bmatrix} \mathrm{C}\,\alpha^{(1)}\zeta_3{}^{(1)} - \mathrm{C}\gamma^{(1)}\,\mathrm{S}\,\alpha^{(1)}\zeta_1{}^{(1)}, & -\mathrm{C}\gamma^{(1)}\,\mathrm{S}\,\alpha^{(1)}\zeta_2{}^{(1)} - \mathrm{S}\,\alpha^{(1)}\,\mathrm{S}\gamma^{(1)}\zeta_3{}^{(1)} \\ \mathrm{C}\,\alpha^{(2)}\zeta_3{}^{(2)} - \mathrm{C}\gamma^{(2)}\,\mathrm{S}\,\alpha^{(2)}\zeta_1{}^{(2)}, & -\mathrm{C}\gamma^{(2)}\,\mathrm{S}\,\alpha^{(2)}\zeta_2{}^{(2)} - \mathrm{S}\,\alpha^{(2)}\,\mathrm{S}\gamma^{(2)}\zeta_3{}^{(2)} \\ \vdots & \vdots \\ \mathrm{C}\,\alpha^{(n)}\zeta_3{}^{(n)} - \mathrm{C}\gamma^{(n)}\,\mathrm{S}\,\alpha^{(n)}\zeta_1{}^{(n)}, & -\mathrm{C}\gamma^{(n)}\,\mathrm{S}\,\alpha^{(n)}\zeta_2{}^{(n)} - \mathrm{S}\,\alpha^{(n)}\,\mathrm{S}\gamma^{(n)}\zeta_3{}^{(n)} \end{bmatrix} \tag{3.39} $$

where

S ( ): means the sine function.

C ( ): means the cosine function.

$$ \zeta_1{}^{(i)} = b\left[cos\left(\beta^{(i)}\right)sin(\theta) - sin(\beta^{(i)})\,cos(\theta)\,sin(\psi)\right] $$

$$ \zeta_2{}^{(i)} = b\left[sin\left(\beta^{(i)}\right)\{\cos(\varphi)\cos(\psi) + \sin(\varphi)\,sin(\theta)\sin(\psi)\} + cos(\beta^{(i)})\,cos(\theta)\,sin(\varphi)\right] $$

$$ \zeta_3{}^{(i)} = b\left[sin\left(\beta^{(i)}\right)\{\cos(\psi)\sin(\varphi) - \cos(\varphi)\,sin(\theta)\sin(\psi)\} - cos(\beta^{(i)})\,cos(\theta)\,cos(\varphi)\right] $$

3.6.2 Mooring Cables Stiffness Matrix

Cable stiffness depends on the type of cable material and cable pre-tension, and it depends on the position and orientation (known as the location) of the floating structure. In the study, all mooring cables are assumed to be straight [68, 79-87]. The FCDP's static force balance can be written as

$$\mathbf{F} = \mathbf{J}^{\mathrm{T}}\boldsymbol{\tau} \tag{3.40}$$

For an FCDP with 6 DOF, the vector of $F = [F_x \quad F_y \quad F_z \quad M_x \quad M_y \quad M_z]^T$ represents of external forces along the X, Y and Z directions and external moments about the X, Y and Z directions. $\boldsymbol{\tau} = [\tau^{(1)} \quad \tau^{(2)}, \quad . \quad . \quad ., \quad \tau^{(n)}]^T$ is the vector of internal mooring cable forces and n is the mooring cable's number.

Equation (3.40) is differentiated to find the stiffness matrix as follows:

$$\delta\mathbf{F} = \mathbf{J}^{\mathrm{T}}\delta\boldsymbol{\tau} + \delta\mathbf{J}^{\mathrm{T}}\boldsymbol{\tau} \tag{3.41}$$

Equation (3.41) can be expressed as

$$\delta\mathbf{F} = \mathbf{K}\,\delta\mathbf{r} \tag{3.42}$$

where δr is the twist vector **K** is the stiffness matrix. For an FCDP, the stiffness of each mooring cable has been modelled as a simple spring. Thus, the changes in forces of the mooring cable can be written as follows:

$$\delta\boldsymbol{\tau} = \Omega\,\delta\mathbf{l} \tag{3.43}$$

where

$$\Omega = diag\left[k^{(1)},\ k^{(2)}, \ldots, k^{(n)}\right] \tag{3.44}$$

and where n is the mooring cables' number and $k^{(i)}$ is the ith mooring cable's stiffness per one meter. The relationship between the twist vector of the moving structure's centroid $\delta\mathbf{r}$ and differential changes in mooring cable lengths $\delta\mathbf{l}$ can be defined using the Jacobian matrix $\mathbf{J}$ as

$$\delta\mathbf{l} = \mathbf{J}\delta\mathbf{r} \tag{3.45}$$

where $\delta\mathbf{l} = \left[\delta l^{(1)},\ \delta l^{(2)}, \dots, \delta l^{(n)}\right]^T$, n: is the mooring cable number.

Thus, the first term on the right-hand side of Equation (3.41) can be expressed using Equations (3.43), (3.44) and (3.45) as follows:

$$\mathbf{J}^{\mathrm{T}}\delta\boldsymbol{\tau} = \mathbf{J}^{\mathrm{T}}\Omega\,\mathbf{J}\,\delta\mathbf{r} \tag{3.46}$$

For the FCDP, the translocation of the Jacobian matrix is in terms of the mooring cable orientation and the moving structure orientation [88]. Thus, $\delta\mathbf{J}^{(i)^T}$ can be written as

$$\delta\mathbf{J}^{(i)^T} = \frac{\partial\mathbf{J}^{(i)}}{\partial\alpha^{(i)}}\,\delta\alpha^{(i)} + \frac{\partial\mathbf{J}^{(i)}}{\partial\gamma^{(i)}}\,\delta\gamma^{(i)} + \frac{\partial\mathbf{J}^{(i)}}{\partial\psi}\,\delta\psi + \frac{\partial\mathbf{J}^{(i)}}{\partial\theta}\,\delta\theta + \frac{\partial\mathbf{J}^{(i)}}{\partial\varphi}\,\delta\varphi \tag{3.47}$$

where

$\mathbf{J}^{(i)^T}$ is the i th column of matrix $\mathbf{J}^{\mathrm{T}}$.

$$\delta\boldsymbol{\alpha} = \mathbf{J}_{\alpha}\ [\delta x \quad \delta y \quad \delta z \quad \delta\psi \quad \delta\theta \quad \delta\varphi]^T$$

$$\delta\boldsymbol{\gamma} = \mathbf{J}_{\gamma}\ [\delta x \quad \delta y \quad \delta z \quad \delta\psi \quad \delta\theta \quad \delta\varphi]^T$$

$\mathbf{J}_{\alpha}$ can be found by differentiating the Jacobean matrix with respect to α [88]. Hence,

$$\mathbf{J}_{\alpha} = \begin{bmatrix} \frac{\mathrm{C}(\alpha^{(1)})\,\mathrm{C}(\gamma^{(1)})}{l^{(1)}} & \frac{\mathrm{C}(\alpha^{(1)})\,\mathrm{S}(\gamma^{(1)})}{l^{(1)}} & \frac{-\mathrm{S}(\alpha^{(1)})}{l^{(1)}} & -\frac{\mathrm{S}(\alpha^{(1)})\,\zeta_2{}^{(1)} - \mathrm{C}(\alpha^{(1)})\,\mathrm{S}(\gamma^{(1)})\,\zeta_1{}^{(1)}}{l^{(1)}} \dots \\ \vdots & \vdots & \vdots & \vdots \\ \frac{\mathrm{C}(\alpha^{(n)})\,\mathrm{C}(\gamma^{(n)})}{l^{(n)}} & \frac{\mathrm{C}(\alpha^{(n)})\,\mathrm{S}(\gamma^{(n)})}{l^{(n)}} & \frac{-\mathrm{S}(\alpha^{(n)})}{l^{(n)}} & -\frac{\mathrm{S}(\alpha^{(n)})\,\zeta_2{}^{(n)} - \mathrm{C}(\alpha^{(n)})\,\mathrm{S}(\gamma^{(n)})\,\zeta_1{}^{(n)}}{l^{(n)}} \dots \end{bmatrix} \tag{3.48}$$

$$\left.\begin{matrix} -\dfrac{\mathrm{S}(\alpha^{(1)})\,\zeta_3{}^{(1)} + \mathrm{C}(\alpha^{(1)})\,\mathrm{C}(\gamma^{(1)})\,\zeta_1{}^{(1)}}{l^{(1)}} & -\dfrac{\mathrm{C}(\alpha^{(1)})\,\mathrm{C}(\gamma^{(1)})\,\zeta_2{}^{(1)} + \mathrm{C}(\alpha^{(1)})\,\mathrm{S}(\gamma^{(1)})\,\zeta_3{}^{(1)}}{l^{(1)}} \\ \vdots & \vdots \\ -\dfrac{\mathrm{S}(\alpha^{(n)})\,\zeta_3{}^{(n)} + \mathrm{C}(\alpha^{(n)})\,\mathrm{C}(\gamma^{(n)})\,\zeta_1{}^{(n)}}{l^{(n)}} & -\dfrac{\mathrm{C}(\alpha^{(n)})\,\mathrm{C}(\gamma^{(n)})\,\zeta_2{}^{(n)} + \mathrm{C}(\alpha^{(n)})\,\mathrm{S}(\gamma^{(n)})\,\zeta_3{}^{(n)}}{l^{(n)}} \end{matrix}\right]_{n\mathrm{x}6}$$

Also, $\mathbf{J}_{\gamma}$ can be found by differentiating the Jacobean matrix with respect to γ [88]. Hence,

$$\mathbf{J}_{\gamma} = \left[\begin{matrix} -\dfrac{\mathrm{S}(\alpha^{(1)})\,\mathrm{S}(\gamma^{(1)})}{l^{(1)}} & \dfrac{\mathrm{C}(\gamma^{(1)})\,\mathrm{S}(\alpha^{(1)})}{l^{(1)}} & 0 & \dfrac{\mathrm{C}(\gamma^{(1)})\,\mathrm{S}(\alpha^{(1)})\,\zeta_1{}^{(1)}}{l^{(1)}} \ldots \\ \vdots & \vdots & \vdots & \vdots \\ -\dfrac{\mathrm{S}(\alpha^{(n)})\,\mathrm{S}(\gamma^{(n)})}{l^{(n)}} & \dfrac{\mathrm{C}(\gamma^{(n)})\,\mathrm{S}(\alpha^{(n)})}{l^{(n)}} & 0 & \dfrac{\mathrm{C}(\gamma^{(n)})\,\mathrm{S}(\alpha^{(n)})\,\zeta_1{}^{(n)}}{l^{(n)}} \ldots \end{matrix}\right.$$
$$\left.\begin{matrix} \dfrac{\mathrm{S}(\alpha^{(1)})\,\mathrm{S}(\gamma^{(1)})\,\zeta_1{}^{(1)}}{l^{(1)}} & -\dfrac{\mathrm{C}(\gamma^{(1)})\,\mathrm{S}(\alpha^{(1)})\;\zeta_3{}^{(1)} - \mathrm{S}(\alpha^{(1)})\,\mathrm{S}(\gamma^{(1)})\,\zeta_2{}^{(1)}}{l^{(1)}} \\ \vdots & \vdots \\ \dfrac{\mathrm{S}(\alpha^{(n)})\,\mathrm{S}(\gamma^{(n)})\,\zeta_1{}^{(n)}}{l^{(n)}} & -\dfrac{\mathrm{C}(\gamma^{(n)})\,\mathrm{S}(\alpha^{(n)})\;\zeta_3{}^{(n)} - \mathrm{S}(\alpha^{(n)})\,\mathrm{S}(\gamma^{(n)})\,\zeta_2{}^{(n)}}{l^{(n)}} \end{matrix}\right]_{n\mathrm{x}6} \tag{3.49}$$

Equations (3.50) to (3.54) represent the Equation (3.47) terms (*i*: *i*th mooring cable).

$$\frac{\partial \mathbf{J}^{(i)}}{\partial \alpha^{(i)}} = \begin{bmatrix} 0 \ldots & \mathrm{C}(\alpha^{(i)})\,\mathrm{C}(\gamma^{(i)}) & \ldots\ 0 \\ 0 \ldots & \mathrm{C}(\alpha^{(i)})\,\mathrm{S}(\gamma^{(i)}) & \ldots\ 0 \\ 0 \ldots & -\mathrm{S}\big(\alpha^{(i)}\big) & \ldots\ 0 \\ 0 \ldots & \mathrm{C}(\alpha^{(i)})\,\mathrm{S}(\gamma^{(i)})\;\zeta_1{}^{(i)} - \mathrm{S}(\alpha^{(i)})\,\zeta_2{}^{(i)} & \ldots\ 0 \\ 0 \ldots & -\mathrm{S}\big(\alpha^{(i)}\big)\,\zeta_3{}^{(i)} - \mathrm{C}(\alpha^{(i)})\,\mathrm{C}(\gamma^{(i)})\,\zeta_1{}^{(i)} & \ldots\ 0 \\ 0 \ldots & -\mathrm{C}(\alpha^{(i)})\,\mathrm{C}(\gamma^{(i)})\,\zeta_2{}^{(i)} - \mathrm{C}(\alpha^{(i)})\,\mathrm{S}(\gamma^{(i)})\,\zeta_3{}^{(i)} & \ldots\ 0 \end{bmatrix}_{6\mathrm{x}n} \tag{3.50}$$

$$\frac{\partial \mathbf{J}^{(i)}}{\partial \gamma^{(i)}} = \begin{bmatrix} 0 \ldots & -\mathrm{S}(\alpha^{(i)})\,\mathrm{S}(\gamma^{(i)}) & \ldots\ 0 \\ 0 \ldots & \mathrm{C}(\gamma^{(i)})\,\mathrm{S}(\alpha^{(i)}) & \ldots\ 0 \\ 0 \ldots & 0 & \ldots\ 0 \\ 0 \ldots & \mathrm{C}(\gamma^{(i)})\,\mathrm{S}(\alpha^{(i)})\;\zeta_1{}^{(i)} & \ldots\ 0 \\ 0 \ldots & \mathrm{S}(\alpha^{(i)})\,\mathrm{S}(\gamma^{(i)})\;\zeta_1{}^{(i)} & \ldots\ 0 \\ 0 \ldots & \mathrm{S}(\alpha^{(i)})\,\mathrm{S}(\gamma^{(i)})\,\zeta_2{}^{(i)} - \mathrm{C}\big(\gamma^{(i)}\big)\,\mathrm{S}\big(\alpha^{(i)}\big)\;\zeta_3{}^{(i)} & \ldots\ 0 \end{bmatrix}_{6\mathrm{xn}} \tag{3.51}$$

$$\frac{\partial \mathbf{J}^{(i)}}{\partial \psi} = \begin{bmatrix} 0 & 0 & 0 & & & \\ 0 & 0 & 0 & & & \\ 0 & 0 & 0 & & & \\ 0 & 0 & 0 & -\mathrm{C}(\alpha^{(i)})\ \zeta_5{}^{(i)} & -\mathrm{S}(\alpha^{(i)})\,\mathrm{S}(\gamma^{(i)})\,\zeta_4{}^{(i)} & \cdots \\ 0 & 0 & 0 & & & \\ 0 & 0 & 0 & & & \end{bmatrix}$$

$$\begin{bmatrix} 0 & 0 \\ 0 & 0 \\ 0 & 0 \\ \mathrm{C}(\gamma^{(i)})\,\mathrm{S}(\alpha^{(i)})\,\zeta_4{}^{(i)} - \mathrm{C}(\alpha^{(i)})\,\zeta_6{}^{(i)} & \mathrm{C}(\gamma^{(i)})\,\mathrm{S}(\alpha^{(i)})\,\zeta_5{}^{(i)} + \mathrm{S}(\alpha^{(i)})\,\mathrm{S}(\gamma^{(i)})\,\zeta_6{}^{(i)} \\ 0 & 0 \\ 0 & 0 \end{bmatrix}_{6xn} \tag{3.52}$$

where

$$\zeta_4{}^{(i)} = b\ sin(\beta^{(i)})\ cos(\theta)\cos(\psi)$$

$$\zeta_5{}^{(i)} = b\ sin\left(\beta^{(i)}\right)[\cos(\varphi)\sin(\psi) - \sin(\varphi)\ sin(\theta)\cos(\psi)\ ]$$

$$\zeta_6{}^{(i)} = b\ sin\left(\beta^{(i)}\right)[\sin(\varphi)\sin(\psi) + \cos(\varphi)\ sin(\theta)\cos(\psi)\ ]$$

$$\frac{\partial \mathbf{J}^{(i)}}{\partial \theta} = \begin{bmatrix} 0 & 0 & 0 & & & \\ 0 & 0 & 0 & & & \\ 0 & 0 & 0 & & & \\ 0 & 0 & 0 & & & \cdots \\ 0 & 0 & 0 & \mathrm{S}(\alpha^{(i)})\,S(\gamma^{(i)})\,\zeta_9{}^{(i)} & -C(\alpha^{(i)})\,\zeta_7{}^{(i)} & \\ 0 & 0 & 0 & & & \end{bmatrix}$$

$$\begin{bmatrix} 0 & 0 \\ 0 & 0 \\ 0 & 0 \\ 0 & 0 \\ C(\alpha^{(i)})\,\zeta_8{}^{(i)} - C(\gamma^{(i)})\,S(\alpha^{(i)})\,\zeta_9{}^{(i)} & C(\gamma^{(i)})\,S(\alpha^{(i)})\,\zeta_7{}^{(i)} - S(\gamma^{(i)})\,S(\alpha^{(i)})\,\zeta_8{}^{(i)} \\ 0 & 0 \end{bmatrix}_{6x6} \tag{3.53}$$

where

$$\zeta_7{}^{(i)} = b\ sin(\varphi)\left[\cos\left(\beta^{(i)}\right)\sin(\theta) - \sin\left(\beta^{(i)}\right)cos(\theta)\sin(\psi)\ \right]$$

$$\zeta_8{}^{(i)} = b\ cos(\varphi)\left[\cos\left(\beta^{(i)}\right)\sin(\theta) - \sin\left(\beta^{(i)}\right)cos(\theta)\sin(\psi)\ \right]$$

$$\zeta_9{}^{(i)} = b\left[\cos\left(\beta^{(i)}\right)\cos(\theta) + \sin\left(\beta^{(i)}\right)sin(\theta)\sin(\psi)\ \right]$$

$$\frac{\partial \mathbf{J}^{(i)}}{\partial \varphi} = \begin{bmatrix} 0 & 0 & 0 & 0 \\ 0 & 0 & 0 & 0 \\ 0 & 0 & 0 & 0 \\ 0 & 0 & 0 & 0 \\ 0 & 0 & 0 & 0 \\ 0 & 0 & 0 & -\mathrm{C}(\alpha^{(i)})\,\zeta_3{}^{(i)} \end{bmatrix} \quad \cdots \quad \begin{bmatrix} 0 & 0 \\ 0 & 0 \\ 0 & 0 \\ 0 & 0 \\ 0 & 0 \\ C(\alpha^{(i)})\,\zeta_2{}^{(i)} & C(\gamma^{(i)})\,S(\alpha^{(i)})\,\zeta_3{}^{(i)} - S(\alpha^{(i)})\,S(\gamma^{(i)})\,\zeta_2{}^{(i)} \end{bmatrix}_{6xn} \tag{3.54}$$

Thus, the second term on the right-hand side of Equation (3.41) can be formulated using Equation (3.47) and Equations (3.50) to (3.54) as

$$\delta \mathbf{J}^T \boldsymbol{\tau} = \sum_{i=1}^{n} \delta \mathbf{J}^{(i)^T} \tau^{(i)} \tag{3.55}$$

Since

$$\delta \mathbf{J}^T \boldsymbol{\tau} = \sum_{i=1}^{n} \left[\frac{\partial \mathbf{J}^{(i)}}{\partial \alpha^{(i)}}\, \mathbf{J}_{\alpha} + \frac{\partial \mathbf{J}^{(i)}}{\partial \gamma^{(i)}}\, \mathbf{J}_{\gamma} + \frac{\partial \mathbf{J}^{(i)}}{\partial \psi} + \frac{\partial \mathbf{J}^{(i)}}{\partial \theta} + \frac{\partial \mathbf{J}^{(i)}}{\partial \varphi} \right] \delta \mathbf{r}\, \tau^{(i)} \tag{3.56}$$

Equation (3.55) can be expressed as follows:

$$\delta \mathbf{J}^T \boldsymbol{\tau} = \mathbf{K}_{\boldsymbol{\tau}}\, \delta \mathbf{r} \tag{3.57}$$

Using Equations (3.65) and (3.78), Equation (3.41) take the form

$$\delta \mathbf{F} = \mathbf{K}_s\, \delta \mathbf{r} + \mathbf{K}_{\tau}\, \delta \mathbf{r} \tag{3.58}$$

Using Equations (3.42) and (3.58), the entire stiffness matrix can be represented as

$$\mathbf{K}(\mathbf{x}) = \mathbf{K}_s + \mathbf{K}_{\tau} \tag{3.59}$$

Now the stiffness matrix due to mooring cable's material takes the form

$$\mathbf{K}_s = \mathbf{J}^{\mathrm{T}}\Omega\,\mathbf{J} = \sum_{i=1}^{n} k^{(i)} \begin{bmatrix} k_{11}^s & k_{12}^s & k_{13}^s & k_{14}^s & k_{15}^s & k_{16}^s \\ k_{21}^s & k_{22}^s & k_{23}^s & k_{24}^s & k_{25}^s & k_{26}^s \\ k_{31}^s & k_{32}^s & k_{33}^s & k_{34}^s & k_{35}^s & k_{36}^s \\ k_{41}^s & k_{42}^s & k_{43}^s & k_{44}^s & k_{45}^s & k_{46}^s \\ k_{51}^s & k_{52}^s & k_{53}^s & k_{54}^s & k_{55}^s & k_{56}^s \\ k_{61}^s & k_{62}^s & k_{63}^s & k_{64}^s & k_{65}^s & k_{66}^s \end{bmatrix} \tag{3.60}$$

Where

$k_{11}^s = \mathrm{C}(\gamma^{(i)})^2\,\mathrm{S}(\alpha^{(i)})^2$ | $k_{12}^s = \mathrm{C}(\gamma^{(i)})\,\mathrm{S}(\alpha^{(i)})^2\,\mathrm{S}(\gamma^{(i)})$ | $k_{13}^s = \mathrm{C}(\alpha^{(i)})\,\mathrm{C}(\gamma^{(i)})\,\mathrm{S}(\alpha^{(i)})$

$k_{14}^s = \mathrm{C}(\gamma^{(i)})\,\mathrm{S}(\alpha^{(i)})\,{\zeta_{12}}^{(i)}$ | $k_{15}^s = \mathrm{C}(\gamma^{(i)})\,\mathrm{S}(\alpha^{(i)})\,{\zeta_{10}}^{(i)}$ | $k_{16}^s = -\,\mathrm{C}(\gamma^{(i)})\,\mathrm{S}(\alpha^{(i)})\;{\zeta_{11}}^{(i)}$

$k_{21}^s = \mathrm{C}(\gamma^{(i)})\,\mathrm{S}(\alpha^{(i)})^2\,\mathrm{S}(\gamma^{(i)})$ | $k_{22}^s = \mathrm{S}(\alpha^{(i)})^2\,\mathrm{S}(\gamma^{(i)})^2$ | $k_{23}^s = \mathrm{C}(\alpha^{(i)})\,\mathrm{S}(\alpha^{(i)})\,\mathrm{S}(\gamma^{(i)})$

$k_{24}^s = \mathrm{S}(\alpha^{(i)})\,\mathrm{S}(\gamma^{(i)})\,{\zeta_{12}}^{(i)}$ | $k_{25}^s = \mathrm{S}(\alpha^{(i)})\,\mathrm{S}(\gamma^{(i)})\,{\zeta_{10}}^{(i)}$ | $k_{26}^s = -\,\mathrm{S}(\alpha^{(i)})\,\mathrm{S}(\gamma^{(i)})\;{\zeta_{11}}^{(i)}$

$k_{31}^s = \mathrm{C}(\alpha^{(i)})\,\mathrm{C}(\gamma^{(i)})\,\mathrm{S}(\alpha^{(i)})$ | $k_{32}^s = \mathrm{C}(\alpha^{(i)})\,\mathrm{S}(\alpha^{(i)})\,\mathrm{S}(\gamma^{(i)})$ | $k_{33}^s = \mathrm{C}(\alpha^{(i)})^2$

$k_{34}^s = \mathrm{C}(\alpha^{(i)})\,{\zeta_{12}}^{(i)}$ | $k_{35}^s = \mathrm{C}(\alpha^{(i)})\,{\zeta_{10}}^{(i)}$ | $k_{36}^s = -\,\mathrm{C}(\alpha^{(i)})\;{\zeta_{11}}^{(i)}$

$k_{41}^s = \mathrm{C}(\gamma^{(i)})\,\mathrm{S}(\alpha^{(i)})\,{\zeta_{12}}^{(i)}$ | $k_{42}^s = \mathrm{S}(\alpha^{(i)})\,\mathrm{S}(\gamma^{(i)})\,{\zeta_{12}}^{(i)}$ | $k_{43}^s = \mathrm{C}(\alpha^{(i)})\,{\zeta_{12}}^{(i)}$

$k_{44}^s = {\zeta_{12}}^{(i)^2}$ | $k_{45}^s = {\zeta_{10}}^{(i)}{\zeta_{12}}^{(i)}$ | $k_{46}^s = -{\zeta_{11}}^{(i)}{\zeta_{12}}^{(i)}$

$k_{51}^s = \mathrm{C}(\gamma^{(i)})\,\mathrm{S}(\alpha^{(i)})\,{\zeta_{10}}^{(i)}$ | $k_{52}^s = \mathrm{S}(\alpha^{(i)})\,\mathrm{S}(\gamma^{(i)})\,{\zeta_{10}}^{(i)}$ | $k_{53}^s = \mathrm{C}(\alpha^{(i)})\,{\zeta_{10}}^{(i)}$

$k_{54}^s = {\zeta_{10}}^{(i)}{\zeta_{12}}^{(i)}$ | $k_{55}^s = {\zeta_{10}}^{(i)^2}$ | $k_{56}^s = -{\zeta_{10}}^{(i)}{\zeta_{11}}^{(i)}$

$k_{61}^s = -\,\mathrm{C}(\gamma^{(i)})\,\mathrm{S}(\alpha^{(i)})\;{\zeta_{11}}^{(i)}$ | $k_{62}^s = -\,\mathrm{S}(\alpha^{(i)})\,\mathrm{S}(\gamma^{(i)})\;{\zeta_{11}}^{(i)}$ | $k_{63}^s = -\,\mathrm{C}(\alpha^{(i)})\;{\zeta_{11}}^{(i)}$

$k_{64}^s = -{\zeta_{11}}^{(i)}{\zeta_{12}}^{(i)}$ | $k_{65}^s = -{\zeta_{10}}^{(i)}{\zeta_{11}}^{(i)}$ | $k_{66}^s = {\zeta_{11}}^{(i)^2}$

$${\zeta_{10}}^{(i)} = \mathrm{C}(\alpha^{(i)})\,{\zeta_3}^{(i)} - \mathrm{C}(\gamma^{(i)})\,\mathrm{S}(\alpha^{(i)})\,{\zeta_1}^{(i)}$$

$${\zeta_{11}}^{(i)} = \mathrm{C}(\gamma^{(i)})\,\mathrm{S}(\alpha^{(i)})\,{\zeta_2}^{(i)} + \mathrm{S}(\alpha^{(i)})\,\mathrm{S}(\gamma^{(i)})\,{\zeta_3}^{(i)}$$

$${\zeta_{12}}^{(i)} = \mathrm{C}(\alpha^{(i)})\,{\zeta_2}^{(i)} + \mathrm{S}(\alpha^{(i)})\,\mathrm{S}(\gamma^{(i)})\,{\zeta_1}^{(i)}$$

and the stiffness matrix due to mooring cable's tensions

$$\mathbf{K}_\tau = \sum_{i=1}^{n} \tau^{(i)} \left[\frac{\partial \mathbf{J}^{(i)}}{\partial \alpha^{(i)}}\,\mathbf{J}_{\,\alpha} + \frac{\partial \mathbf{J}^{(i)}}{\partial \gamma^{(i)}}\,\mathbf{J}_{\,\gamma} + \frac{\partial \mathbf{J}^{(i)}}{\partial \psi} + \frac{\partial \mathbf{J}^{(i)}}{\partial \theta} + \frac{\partial \mathbf{J}^{(i)}}{\partial \varphi} \right] \tag{3.61}$$

$$\mathbf{K}_{\tau} = \sum_{i=1}^{n} \frac{\tau^{(i)}}{l^{(i)}} \begin{bmatrix} k_{11}^{\tau} & k_{12}^{\tau} & k_{13}^{\tau} & k_{14}^{\tau} & k_{15}^{\tau} & k_{16}^{\tau} \\ k_{21}^{\tau} & k_{22}^{\tau} & k_{23}^{\tau} & k_{24}^{\tau} & k_{25}^{\tau} & k_{26}^{\tau} \\ k_{31}^{\tau} & k_{32}^{\tau} & k_{33}^{\tau} & k_{34}^{\tau} & k_{35}^{\tau} & k_{36}^{\tau} \\ k_{41}^{\tau} & k_{42}^{\tau} & k_{43}^{\tau} & k_{44}^{\tau} & k_{45}^{\tau} & k_{46}^{\tau} \\ k_{51}^{\tau} & k_{52}^{\tau} & k_{53}^{\tau} & k_{54}^{\tau} & k_{55}^{\tau} & k_{56}^{\tau} \\ k_{61}^{\tau} & k_{62}^{\tau} & k_{63}^{\tau} & k_{64}^{\tau} & k_{65}^{\tau} & k_{66}^{\tau} \end{bmatrix} \tag{3.62}$$

where

$k_{11}^{\tau} = \mathrm{C}(\alpha^{(i)})^2\,\mathrm{C}(\gamma^{(i)})^2 + \mathrm{S}(\alpha^{(i)})^2\,\mathrm{S}(\gamma^{(i)})^2$	$k_{12}^{\tau} = -\mathrm{C}(\gamma^{(i)})\,\mathrm{S}(\gamma^{(i)})\,(\mathrm{S}(\alpha^{(i)})^2 - \mathrm{C}(\alpha^{(i)})^2)$
$k_{13}^{\tau} = -\mathrm{C}(\alpha^{(i)})\,\mathrm{C}(\gamma^{(i)})\,\mathrm{S}(\alpha^{(i)})$	$k_{14}^{\tau} = -C(\alpha^{(i)})\,C(\gamma^{(i)})\;\zeta_{20}{}^{(i)} - \zeta_{16}{}^{(i)}$
$k_{15}^{\tau} = -\mathrm{C}(\alpha^{(i)})\,\mathrm{C}(\gamma^{(i)})\;\zeta_{19}{}^{(i)} - S(\alpha^{(i)})^2\,S(\gamma^{(i)})^2\;\zeta_{1}{}^{(i)}$	$k_{16}^{\tau} = -C(\alpha^{(i)})\,C(\gamma^{(i)})\;\zeta_{21}{}^{(i)} + S(\alpha^{(i)})\,S(\gamma^{(i)})\;(\zeta_{18}{}^{(i)} - \zeta_{17}{}^{(i)})$
$k_{21}^{\tau} = -\mathrm{C}(\gamma^{(i)})\,\mathrm{S}(\gamma^{(i)})\,(\mathrm{S}(\alpha^{(i)})^2 - \mathrm{C}(\alpha^{(i)})^2)$	$k_{22}^{\tau} = \mathrm{C}(\alpha^{(i)})^2\,\mathrm{S}(\gamma^{(i)})^2 + \mathrm{C}(\gamma^{(i)})^2\,\mathrm{S}(\alpha^{(i)})^2$
$k_{23}^{\tau} = -\mathrm{C}(\alpha^{(i)})\,\mathrm{S}(\alpha^{(i)})\,\mathrm{S}(\gamma^{(i)})$	$k_{24}^{\tau} = -\mathrm{C}(\alpha^{(i)})\,\mathrm{S}(\gamma^{(i)})\;\zeta_{20}{}^{(i)} + \mathrm{C}(\gamma^{(i)})^2\,\mathrm{S}(\alpha^{(i)})^2\;\zeta_{1}{}^{(i)}$
$k_{25}^{\tau} = -\mathrm{C}(\alpha^{(i)})\,\mathrm{S}(\gamma^{(i)})\;\zeta_{19}{}^{(i)} - \zeta_{16}{}^{(i)}$	$k_{26}^{\tau} = -\mathrm{C}(\alpha^{(i)})\,\mathrm{S}(\gamma^{(i)})\;\zeta_{21}{}^{(i)} - \mathrm{C}(\gamma^{(i)})\,\mathrm{S}(\alpha^{(i)})\;(\zeta_{18}{}^{(i)} - \zeta_{17}{}^{(i)})$
$k_{31}^{\tau} = -\mathrm{C}(\alpha^{(i)})\,\mathrm{C}(\gamma^{(i)})\,\mathrm{S}(\alpha^{(i)})$	$k_{32}^{\tau} = -\mathrm{C}(\alpha^{(i)})\,\mathrm{S}(\alpha^{(i)})\,\mathrm{S}(\gamma^{(i)})$
$k_{33}^{\tau} = \mathrm{S}(\alpha^{(i)})^2$	$k_{34}^{\tau} = \mathrm{S}(\alpha^{(i)})\;\zeta_{20}{}^{(i)}$
$k_{35}^{\tau} = \mathrm{S}(\alpha^{(i)})\;\zeta_{19}{}^{(i)}$	$k_{36}^{\tau} = \mathrm{S}(\alpha^{(i)})\;\zeta_{21}{}^{(i)}$
$k_{41}^{\tau} = -\mathrm{C}(\alpha^{(i)})\,\mathrm{C}(\gamma^{(i)})\;\zeta_{20}{}^{(i)} - \zeta_{16}{}^{(i)}$	$k_{42}^{\tau} = -\mathrm{C}(\alpha^{(i)})\,\mathrm{S}(\gamma^{(i)})\;\zeta_{20}{}^{(i)} + \mathrm{C}(\gamma^{(i)})^2\,\mathrm{S}(\alpha^{(i)})^2\;\zeta_{1}{}^{(i)}$
$k_{43}^{\tau} = \mathrm{S}(\alpha^{(i)})\;\zeta_{20}{}^{(i)}$	

$k_{44}^{\tau} = \zeta_{20}{}^{(i)^2} - l^{(i)}\,\mathrm{C}(\alpha^{(i)})\,\zeta_{5}{}^{(i)} + \mathrm{C}(\gamma^{(i)})^2\,\mathrm{S}(\alpha^{(i)})^2\,\zeta_{1}{}^{(i)^2} - l^{(i)}\,\mathrm{S}(\alpha^{(i)})\,\mathrm{S}(\gamma^{(i)})\,\zeta_{4}{}^{(i)}$
$k_{45}^{\tau} = \zeta_{19}{}^{(i)}\zeta_{20}{}^{(i)} - l^{(i)}\,\mathrm{C}(\alpha^{(i)})\,\zeta_{6}{}^{(i)} + \zeta_{13}{}^{(i)} + l^{(i)}\,\mathrm{C}(\gamma^{(i)})\,\mathrm{S}(\alpha^{(i)})\,\zeta_{4}{}^{(i)}$
$k_{46}^{\tau} = \zeta_{20}{}^{(i)}\zeta_{21}{}^{(i)} - \zeta_{15}{}^{(i)} + l^{(i)}\,\mathrm{C}(\gamma^{(i)})\,\mathrm{S}(\alpha^{(i)})\,\zeta_{5}{}^{(i)} + l^{(i)}\,\mathrm{S}(\alpha^{(i)})\,\mathrm{S}(\gamma^{(i)})\,\zeta_{6}{}^{(i)}$
$k_{51}^{\tau} = -\mathrm{C}(\alpha^{(i)})\,\mathrm{C}(\gamma^{(i)})\;\zeta_{19}{}^{(i)} - \mathrm{S}(\alpha^{(i)})^2\,\mathrm{S}(\gamma^{(i)})^2\;\zeta_{1}{}^{(i)}$

$k_{52}^{\tau} = -\mathrm{C}(\alpha^{(i)})\,\mathrm{S}(\gamma^{(i)})\;\zeta_{19}{}^{(i)} - \zeta_{16}{}^{(i)}$	$k_{53}^{\tau} = \mathrm{S}(\alpha^{(i)})\;\zeta_{19}{}^{(i)}$

$k_{54}^{\tau} = l^{(i)}\,\mathrm{S}(\alpha^{(i)})\,\mathrm{S}(\gamma^{(i)})\,\zeta_{9}{}^{(i)} - l^{(i)}\,\mathrm{C}(\alpha^{(i)})\,\zeta_{7}{}^{(i)} + \zeta_{19}{}^{(i)}\zeta_{20}{}^{(i)} + \zeta_{13}{}^{(i)}$
$k_{55}^{\tau} = \zeta_{19}{}^{(i)^2} + l^{(i)}\,\mathrm{C}(\alpha^{(i)})\,\zeta_{8}{}^{(i)} - l^{(i)}\,\mathrm{C}(\gamma^{(i)})\,\mathrm{S}(\alpha^{(i)})\,\zeta_{9}{}^{(i)} + \mathrm{S}(\alpha^{(i)})^2\,\mathrm{S}(\gamma^{(i)})^2\;\zeta_{1}{}^{(i)^2}$
$k_{56}^{\tau} = \zeta_{19}{}^{(i)}\zeta_{21}{}^{(i)} - \zeta_{14}{}^{(i)} - l^{(i)}\,\mathrm{S}(\alpha^{(i)})\,\mathrm{S}(\gamma^{(i)})\,\zeta_{8}{}^{(i)} + l^{(i)}\,\mathrm{C}(\gamma^{(i)})\,\mathrm{S}(\alpha^{(i)})\,\zeta_{7}{}^{(i)}$
$k_{61}^{\tau} = -\mathrm{C}(\alpha^{(i)})\,\mathrm{C}(\gamma^{(i)})\;\zeta_{21}{}^{(i)} + \mathrm{S}(\alpha^{(i)})\,\mathrm{S}(\gamma^{(i)})\;(\zeta_{18}{}^{(i)} - \zeta_{17}{}^{(i)})$

$$k_{62}^{\tau} = -\mathrm{C}(\alpha^{(i)})\,\mathrm{S}(\gamma^{(i)})\;{\zeta_{21}}^{(i)} - \mathrm{C}(\gamma^{(i)})\,\mathrm{S}(\alpha^{(i)})\;({\zeta_{18}}^{(i)} - {\zeta_{17}}^{(i)})$$

$k_{63}^{\tau} = \mathrm{S}(\alpha^{(i)})\;{\zeta_{21}}^{(i)}$	$k_{64}^{\tau} = {\zeta_{20}}^{(i)}{\zeta_{21}}^{(i)} - {\zeta_{15}}^{(i)} - l^{(i)}\,\mathrm{C}(\alpha^{(i)})\;{\zeta_{3}}^{(i)}$
$k_{65}^{\tau} = {\zeta_{19}}^{(i)}{\zeta_{21}}^{(i)} - {\zeta_{14}}^{(i)} + l^{(i)}\,\mathrm{C}(\alpha^{(i)})\,{\zeta_{2}}^{(i)}$	$k_{66}^{\tau} = {\zeta_{21}}^{(i)^2} + ({\zeta_{18}}^{(i)} - {\zeta_{17}}^{(i)})^2 + l^{(i)}{\zeta_{18}}^{(i)} - l^{(i)}{\zeta_{17}}^{(i)}$
${\zeta_{13}}^{(i)} = \mathrm{C}(\gamma^{(i)})\,\mathrm{S}(\alpha^{(i)})^2\,\mathrm{S}(\gamma^{(i)})\,{\zeta_{1}}^{(i)^2}$	${\zeta_{14}}^{(i)} = \mathrm{S}(\alpha^{(i)})\,\mathrm{S}(\gamma^{(i)})\,{\zeta_{1}}^{(i)}({\zeta_{18}}^{(i)} - {\zeta_{17}}^{(i)})$
${\zeta_{15}}^{(i)} = \mathrm{C}(\gamma^{(i)})\,\mathrm{S}(\alpha^{(i)})\,{\zeta_{1}}^{(i)}({\zeta_{18}}^{(i)} - {\zeta_{17}}^{(i)})$	${\zeta_{16}}^{(i)} = \mathrm{C}(\gamma^{(i)})\,\mathrm{S}(\alpha^{(i)})^2\,\mathrm{S}(\gamma^{(i)})\,{\zeta_{1}}^{(i)}$
${\zeta_{7}}^{(i)} = \mathrm{S}(\alpha^{(i)})\,\mathrm{S}(\gamma^{(i)})\,{\zeta_{2}}^{(i)}$	${\zeta_{18}}^{(i)} = \mathrm{C}(\gamma^{(i)})\,\mathrm{S}(\alpha^{(i)})\,{\zeta_{3}}^{(i)}$
${\zeta_{19}}^{(i)} = \mathrm{S}(\alpha^{(i)})\,{\zeta_{3}}^{(i)} + \mathrm{C}(\alpha^{(i)})\,\mathrm{C}(\gamma^{(i)})\,{\zeta_{1}}^{(i)}$	${\zeta_{20}}^{(i)} = \mathrm{S}(\alpha^{(i)})\,{\zeta_{2}}^{(i)} - \mathrm{C}(\alpha^{(i)})\,\mathrm{S}(\gamma^{(i)})\;{\zeta_{1}}^{(i)}$
${\zeta_{21}}^{(i)} = \mathrm{C}(\alpha^{(i)})\,\mathrm{C}(\gamma^{(i)})\;{\zeta_{2}}^{(i)} + \mathrm{C}(\alpha^{(i)})\,\mathrm{S}(\gamma^{(i)})\,{\zeta_{3}}^{(i)}$	

3.6.3 Added Stiffness Matrix

The added stiffness matrix (hydrostatic stiffness) arise from changes in the center of buoyancy position; namely, translation in the z-direction and rotations about the x- and y-axes. Hence, an additional stiffness matrix can be written in the following form [47, 54, 71]:

$$\mathbf{K}_{\boldsymbol{a}}(\mathbf{x}) = \begin{bmatrix} 0 & 0 & 0 & 0 & 0 & 0 \\ 0 & 0 & 0 & 0 & 0 & 0 \\ 0 & 0 & k_{33} & 0 & 0 & 0 \\ 0 & 0 & 0 & k_{44} & 0 & 0 \\ 0 & 0 & 0 & 0 & k_{55} & 0 \\ 0 & 0 & 0 & 0 & 0 & 0 \end{bmatrix} \tag{3.63}$$

where

$$k_{33} = \rho g A_s$$

$$k_{44} = k_{55} = \rho g A_s D(\overline{KG} - \overline{KB})$$

$$A_s = \frac{\pi}{4} D^2$$

$\overline{KB}$ is the distance between the Center of Buoyancy and the SWL,

D is the diameter of the floating structure of the FCDP, and

g is the gravitational acceleration.

3.7 Dynamic Loads

While the external loads acting on the mooring cables are neglected in this study, there are two types of external loads, which are considered to act on the floating structure of the platform. (i) Buoyancy force, and (ii) Excitation loads caused by water wave impingement on the floating structure.

3.7.1 Buoyancy Force

When a submerged object moves through a fluid, the fluid exerts an upward force which is called a buoyancy force (F_b), as shown in Figures 3.8 and 3.9. It is equal in magnitude to the weight of the volume of the fluid displaced by the object [89].

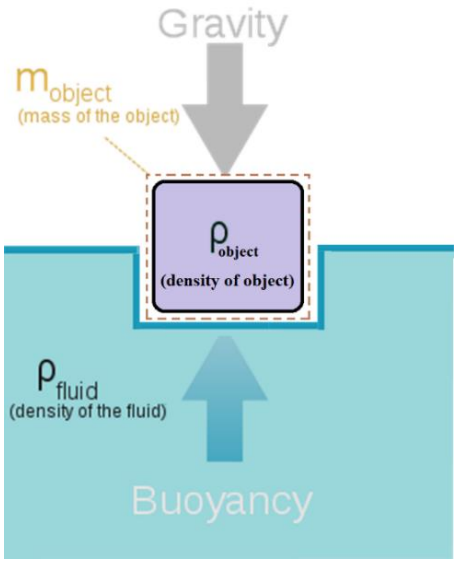

Figure 3.8: The buoyant force sketch.

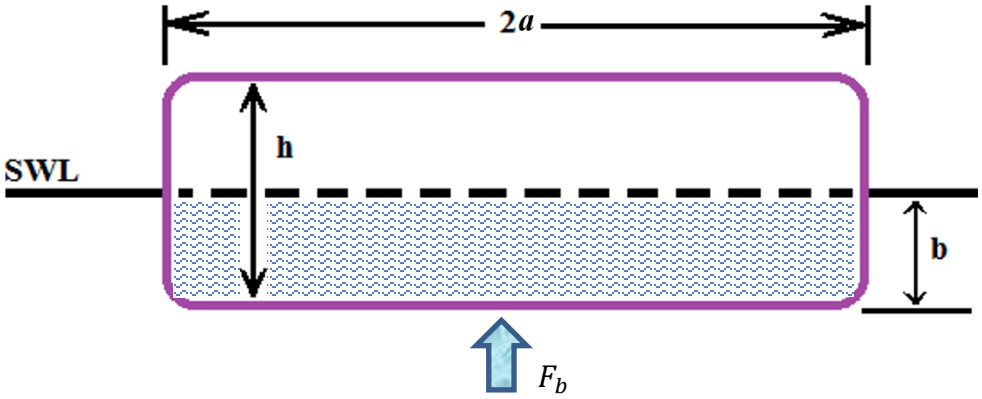

Figure 3.9: Circular cylindrical platform.

Eventually, the water exerts a static upward force (buoyancy force F_b) which equals the weight of the water displaced by the submerged part of the platform. This means that the buoyancy force equals the weight of the displaced volume of fluid.

$$F_b(\mathbf{x}) = \rho_f V_{disp} g \tag{3.64}$$

And for a floating object, the buoyancy force is as follows:

$$F_b(\mathbf{x}) = \rho_{ob}\, V_{ob}\, g \tag{3.65}$$

Where

$$\mathrm{V_{ob}} = \mathrm{h}\pi a^2$$

$$\mathrm{V_{disp}} = b\pi a^2$$

where the symbol (ob) means object, ρ_{ob} is the object density, g the gravitational acceleration, $\mathrm{V_{ob}}$ is the circular plate form volume and b is the submerged depth.

3.7.2 Water Wave Loads

The floating cable-driven platform is considered to be under the effect of sea waves caused by winds and tides. The floating circular cylindrical structure has a radius "a" and submerged depth "b", and has surge, heave, and pitch motions in response to a water wave

traveling along the x-direction. The water wave has an amplitude H/2 and a wavelength λ, as shown in Figure **3.10**.

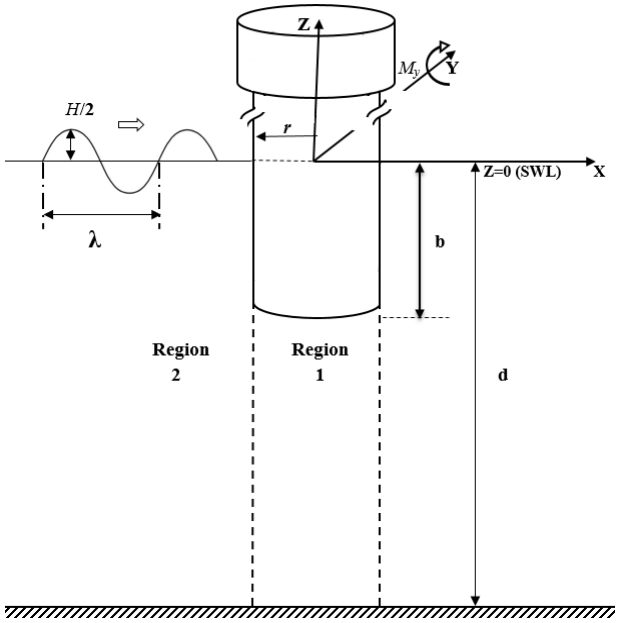

Figure 3.10: Definition sketch for isolated cylinder.

The boundary value problem technique, using the method of separation of variables, was employed by Finnegan et al. [90] to derive the velocity potentials in the fluid domain. Also, they used a Fourier transform to represent the infinite depth of the problem.

In addition to that, Havelock's expansion theorem was used to invert the complicated combined Fourier sine/cosine transform. Also, an asymptotic approximation was taken for low frequency incident waves to create their analytical solution.

Following Finnegan et al. [90], the fluid domain is divided into two regions, as shown in Figure 3.10: (i) an interior region under the floating platform (marked as 1) and (ii) an exterior region that extends to infinity in the horizontal plane (marked as 2). The solution of the scattering and radiation problem for a floating vertical cylindrical disk (in infinitely

deep water) leads to the following analytical expressions for the water wave excitation forces:

$$\boldsymbol{F}_j(\mathbf{x},\mathrm{t}) = \widehat{\boldsymbol{F}}_j\, e^{-i\omega t} \quad , \quad j = x, z \; and \; M \tag{3.66}$$

$$\widehat{\boldsymbol{F}}_x = -\frac{\pi i \rho g H a}{k}\left(J_1(ka) - \frac{J_1'(ka)}{\mathrm{H}_1'(k\,a)}\mathrm{H}_1(ka)\right)(1 - e^{-kb}) \tag{3.67}$$

$$\widehat{\boldsymbol{F}}_z = 2\pi i \rho \omega a \sqrt{\frac{2}{\pi}} \int_0^{\infty} P_0(\varkappa) \frac{I_1(\varkappa r)}{\varkappa I_0(\varkappa a)}\, d\varkappa \tag{3.68}$$

$$\begin{aligned} \widehat{\boldsymbol{F}}_M = M_y = {} & \pi i \rho g H a \left(J_1(ka) - \frac{J_1'(ka)}{\mathrm{H}_1'(k\,a)}\mathrm{H}_1(ka)\right) \int_0^{b} (z-b) e^{-kz}\, dz \\ & + \pi i \rho \omega a^2 \sqrt{\frac{2}{\pi}} \int_0^{\infty} P_1(\varkappa) \frac{I_2(\varkappa r)}{\varkappa I_1(\varkappa a)}\, d\varkappa \end{aligned} \tag{3.69}$$

where

- J_m denotes a Bessel function of the first kind of order m.
- I_m denotes a modified Bessel function of the first kind of order m.
- H_m is the Hankel function of the first kind of order m; primes denote differentiation with respect to argument.
- r is the radius of the cylinder and it is vary from zero to a.
- k is the wave number.
- ϵ_m is Neumann's number, ϵ_o= 1, ϵ_m= 2, m ≥ 1.
- $P_m(\varkappa) = -\frac{gH}{2\omega}\epsilon_m i^{m+1}\sqrt{\frac{2}{\pi}}\left(J_m(ka) - \frac{J_m'(ka)}{\mathrm{H}_m'(k\,a)}\mathrm{H}_m(ka)\right)\frac{e^{-kb}k_o}{\varkappa^2 + k^2}$.

Using Equation 3.66, Figure **3.11** to Figure **3.13** show the time history of wave forces applied on the floating structure of the FCDP at a location of $x = 0\,m;\; y = 0\,m$ with

respect to the fixed Cartesian frame of reference in Figure **3.10**. The mean water depth is d =50 m, the submerged depth of the platform is b = 0.5 m, and the floating structure mass equal 39270 Kg. Also the wave number is $k = 0.16095\, m^{-1}$, corresponding to a frequency of 0.2 Hz, and the wave height $H = 1\, m$.

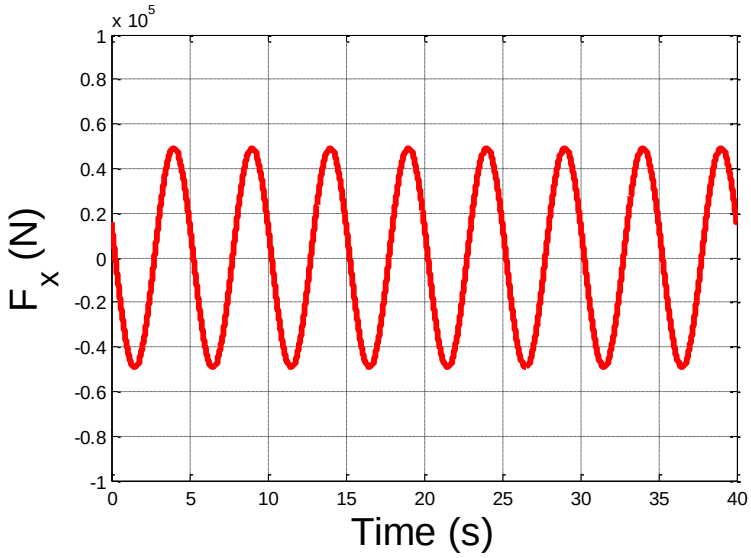

Figure 3.11: Surge time history of applied forces due to wave impinging on the FCDP.

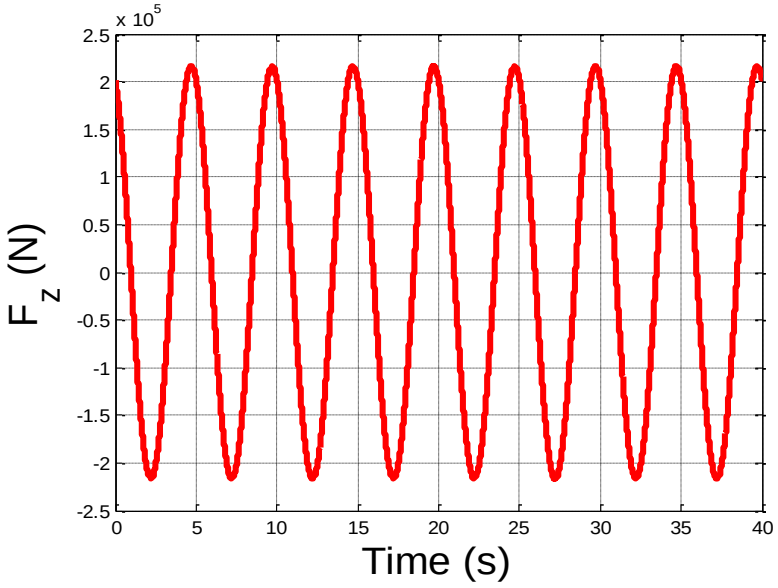

Figure 3.12: Heave time history of applied forces due to wave impinging on the FCDP.

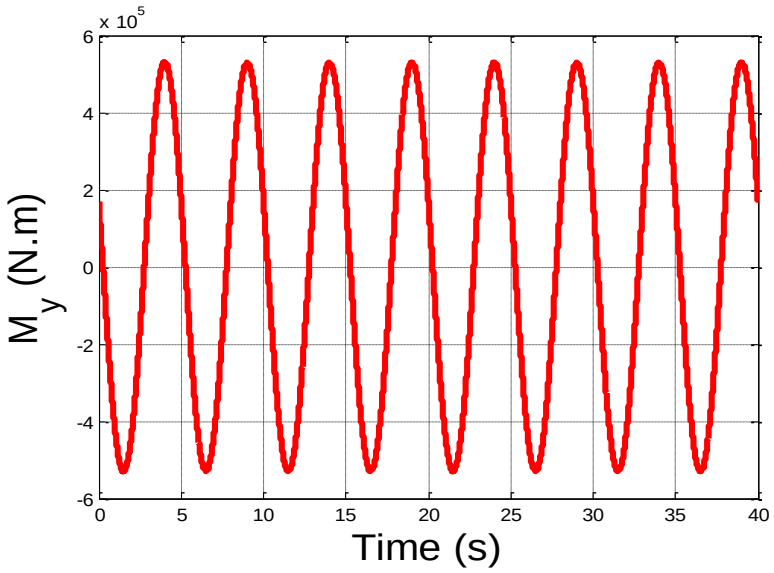

Figure 3.13: Pitch time history of applied forces due to wave impinging on the FCDP.

3.8 Modal Analysis

Modeling the FCDP as a rigid body supported by mooring cables, with known mass, damping and stiffness, the equation of motion of the FCDP can be written as:

$$\mathbf{M}(\mathbf{x})\,\ddot{\mathbf{x}} + \mathbf{C}(\mathbf{x})\,\dot{\mathbf{x}} + \mathbf{K}(\mathbf{x})\,\mathbf{x} = \mathbf{F}(\mathbf{x}, \mathrm{t}) \tag{3.70}$$

where

$$\mathbf{M}(\mathbf{x}) = \mathbf{M}_s + \mathbf{M}_a = \begin{bmatrix} m_1 & 0 & 0 & 0 & 0 & 0 \\ 0 & m_2 & 0 & 0 & 0 & 0 \\ 0 & 0 & m_3 & 0 & 0 & 0 \\ 0 & 0 & 0 & I_4 & 0 & 0 \\ 0 & 0 & 0 & 0 & I_5 & 0 \\ 0 & 0 & 0 & 0 & 0 & I_6 \end{bmatrix} + \begin{bmatrix} m_{11} & 0 & 0 & 0 & m_{15} & 0 \\ 0 & m_{22} & 0 & m_{24} & 0 & 0 \\ 0 & 0 & m_{33} & 0 & 0 & 0 \\ 0 & m_{42} & 0 & m_{44} & 0 & 0 \\ m_{51} & 0 & 0 & 0 & m_{55} & 0 \\ 0 & 0 & 0 & 0 & 0 & 0 \end{bmatrix}$$

$$\mathbf{C}(\mathbf{x}) = \begin{bmatrix} C_{11} & 0 & 0 & 0 & 0 & 0 \\ 0 & C_{22} & 0 & 0 & 0 & 0 \\ 0 & 0 & C_{33} & 0 & 0 & 0 \\ 0 & 0 & 0 & C_{44} & 0 & 0 \\ 0 & 0 & 0 & 0 & C_{55} & 0 \\ 0 & 0 & 0 & 0 & 0 & C_{66} \end{bmatrix}$$

$$\mathbf{K}(\mathbf{x}) = \mathbf{K}_s + \mathbf{K}_\tau + \mathbf{K}_a$$

$$\mathbf{K}_s = \sum_{i=1}^{n} k^{(i)} \begin{bmatrix} k_{11}^s & k_{12}^s & k_{13}^s & k_{14}^s & k_{15}^s & k_{16}^s \\ k_{21}^s & k_{22}^s & k_{23}^s & k_{24}^s & k_{25}^s & k_{26}^s \\ k_{31}^s & k_{32}^s & k_{33}^s & k_{34}^s & k_{35}^s & k_{36}^s \\ k_{41}^s & k_{42}^s & k_{43}^s & k_{44}^s & k_{45}^s & k_{46}^s \\ k_{51}^s & k_{52}^s & k_{53}^s & k_{54}^s & k_{55}^s & k_{56}^s \\ k_{61}^s & k_{62}^s & k_{63}^s & k_{64}^s & k_{65}^s & k_{66}^s \end{bmatrix}$$

$$\mathbf{K}_\tau = \sum_{i=1}^{n} \frac{\tau^{(i)}}{l^{(i)}} \begin{bmatrix} k_{11}^\tau & k_{12}^\tau & k_{13}^\tau & k_{14}^\tau & k_{15}^\tau & k_{16}^\tau \\ k_{21}^\tau & k_{22}^\tau & k_{23}^\tau & k_{24}^\tau & k_{25}^\tau & k_{26}^\tau \\ k_{31}^\tau & k_{32}^\tau & k_{33}^\tau & k_{34}^\tau & k_{35}^\tau & k_{36}^\tau \\ k_{41}^\tau & k_{42}^\tau & k_{43}^\tau & k_{44}^\tau & k_{45}^\tau & k_{46}^\tau \\ k_{51}^\tau & k_{52}^\tau & k_{53}^\tau & k_{54}^\tau & k_{55}^\tau & k_{56}^\tau \\ k_{61}^\tau & k_{62}^\tau & k_{63}^\tau & k_{64}^\tau & k_{65}^\tau & k_{66}^\tau \end{bmatrix}$$

$$\mathbf{K}_a = \begin{bmatrix} \mathbf{0} & \mathbf{0} & \mathbf{0} & \mathbf{0} & \mathbf{0} & \mathbf{0} \\ \mathbf{0} & \mathbf{0} & \mathbf{0} & \mathbf{0} & \mathbf{0} & \mathbf{0} \\ \mathbf{0} & \mathbf{0} & \boldsymbol{k_{33}} & \mathbf{0} & \mathbf{0} & \mathbf{0} \\ \mathbf{0} & \mathbf{0} & \mathbf{0} & \boldsymbol{k_{44}} & \mathbf{0} & \mathbf{0} \\ \mathbf{0} & \mathbf{0} & \mathbf{0} & \mathbf{0} & \boldsymbol{k_{55}} & \mathbf{0} \\ \mathbf{0} & \mathbf{0} & \mathbf{0} & \mathbf{0} & \mathbf{0} & \mathbf{0} \end{bmatrix}$$

$$\mathbf{F}(\mathbf{x}, \mathrm{t}) = \begin{bmatrix} F_x^{wave} + F_x^{wind} & 0 & F_z^{wave} + F_b & 0 & M_y^{wave} + M_y^{wind} & 0 \end{bmatrix}^T$$

The modal analysis method [91] is used to solve Equation (3.70) by converting the equation to uncoupled differential equations of six orders as follows:

$$\mathbf{x_i}(t) = \mathbf{U}\mathbf{q_i}(t) \tag{3.71}$$

where the $\mathbf{x_i}(t)$ are the generalized coordinates, and $\mathbf{q_i}(t)$ are the natural coordinates. Hence,

$$\mathbf{M}(\mathbf{x})\mathbf{U}\ddot{\mathbf{q}} + \mathbf{C}(\mathbf{x})\mathbf{U}\dot{\mathbf{q}} + \mathbf{K}(\mathbf{x})\mathbf{U}\mathbf{q} = \mathbf{F}(\mathbf{x}, \mathrm{t}) \tag{3.72}$$

For more simplicity, we expressed the damping matrix as a linear combination of the mass and stiffness matrices [91]:

$$\mathbf{C}(\mathbf{x}) = \alpha\mathbf{M}(\mathbf{x}) + \beta\mathbf{K}(\mathbf{x}) \tag{3.73}$$

where α and β are constants. By substituting Equation (3.73) into Equation (3.72), the following can be obtained:

$$\mathbf{U}^T\mathbf{M}(\mathbf{x})\mathbf{U}\ddot{\mathbf{q}} + [\alpha\mathbf{U}^T\mathbf{M}(\mathbf{x})\mathbf{U} + \beta\mathbf{U}^T\mathbf{K}(\mathbf{x})\mathbf{U}]\dot{\mathbf{q}} + \mathbf{U}^T\mathbf{K}(\mathbf{x})\mathbf{U}\mathbf{q} = \mathbf{U}^T\mathbf{F}(\mathbf{x}, \mathrm{t}) \tag{3.74}$$

$$\ddot{\mathbf{q}}_{\boldsymbol{i}}(t) + 2\xi_i\omega_i\mathbf{q}_{\boldsymbol{i}}(t) + \omega_i^2\mathbf{q}_{\boldsymbol{i}}(t) \;=\; \mathbf{n}_{\boldsymbol{i}}(t) \tag{3.75}$$

where

$$\mathbf{n}_i(t) = \; \mathbf{U}^T\mathbf{F}(\mathbf{x}, \mathrm{t}) \tag{3.76}$$

$$2\xi_i\omega_i = (\alpha + \omega_i^2\beta) \tag{3.77}$$

and ω_i is the ith natural frequency of the system, $\xi_i$is the modal damping ratio for the ith normal mode, **U** is the modal matrix (shape vectors), $i = 1, 2, 3 \ldots .6$.

The solution of Equation (3.75) can be written as:

$$\begin{aligned}\mathbf{q}_i(t) \;=\; e^{-\xi_i\omega_i t}&\left\{\cos\omega_{di}t + \frac{\xi_i}{\sqrt{1-{\xi_i}^2}}\sin\omega_{di}t\right\}q_i(0)\\ &+\left\{\frac{1}{\omega_{di}}e^{-\xi_i\omega_i t}\sin\omega_{di}t\right\}\dot{q}_0(0)\\ &+\frac{1}{\omega_{di}}\int_0^t \mathbf{n}_i(\tau)\,e^{-\xi_i\omega_i(t-\tau)}\sin\omega_{di}(t-\tau)\,d\tau\,,\end{aligned} \tag{3.78}$$

where $i = 1,2, \ldots . \mathrm{n}$, $\omega_{di} = \omega_i\sqrt{1-{\xi_i}^2}$

The original states vector **x** can be rewritten as:

$$\mathbf{x}_i(t) = \; \mathbf{U}\mathbf{q}_i(t) \tag{3.79}$$

The velocity and the acceleration of the FCDP can be obtained by differentiating Equation (3.79) with respect to time.

3.9 Effective Area Analysis

Let us determine the domain within which the platform floating structure can move while keeping all mooring cables under tension. The set of all locations with all mooring cables under tension defines an "effective area" beyond which the platform is deemed worthless. In order to maintain all mooring cables under tension, the submerged depth is adjusted to induce the sufficient axial forces into the cables. There is a specific minimum submerged depth for any location occupied by the floating structure within the effective area of cable-driven platform effective area. A calculation scheme is followed for specifying the minimum submerged depth and determining the effective area. Starting from the (x=0,y=0) location, an initial submerged depth is selected and cable elongations due to buoyancy and water waves acting on the platform is calculated. Then, cable tensions can be calculated from $\mathbf{T}_i = k_i \Delta L_i$, where subscript $i(= 1, \ldots, \mathrm{n})$, represents the cable number and $k_i(= \frac{EA}{L})_i$ is the mooring cable material stiffness of $30 * 10^3$ N/m. The submerged depth is reduced in steps until one or more of the cable tension(s) cross the zero tension value, and then the minimum submerged depth is determined for that location. By repeating this calculation process at all plausible locations, one can specify the effective area of the platform floating structure. Figure 3.14 shows a flowchart which is used to measure the FCDP effective area.

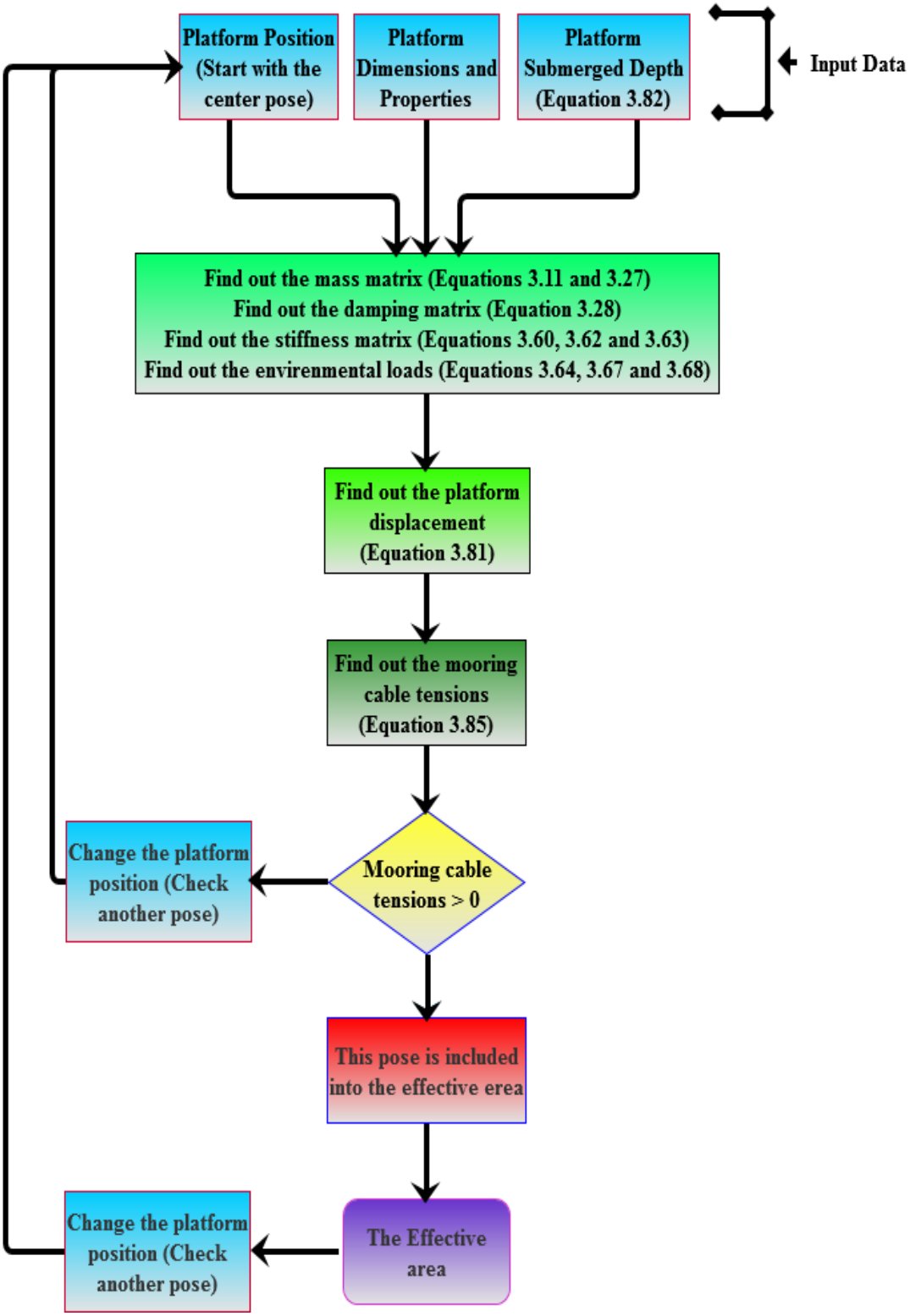

Figure 3.14: Flowchart which is used to measure the FCDP effective area.

The platform is anchored to the seabed by pre-tensioned mooring cables. Hence, the submerged depth can be calculated from

$$b = \bar{b} + b_w \tag{3.80}$$

$$\bar{b} = \frac{\bar{f}}{\rho_w \pi g a^2} \tag{3.81}$$

$$[0 \quad 0 \quad \bar{f} \quad 0 \quad 0 \quad 0]^T = \mathbf{J}\,\bar{\boldsymbol{\tau}} \tag{3.82}$$

where $\bar{b}$ is the submerged depth due to the mooring cable pre-tensions, **J** is the Jacobean matrix, $\bar{f}$ is the vertical force applied downward on the mobile platform by the mooring cable pre-tensions, $\bar{\boldsymbol{\tau}}$ is a vector of the mooring cable pre-tension, ρ_w is the water density, g is the gravitational acceleration, and b_w is the submerged depth due to platform weight.

Equation (3.83) is used to give the mooring cable tensions, at any location, which is the sufficient pre-tension needed at that location. This pre-tension is to ensure that there are non-negative mooring cable tensions when the FCDP is exposed to environmental loads. These mooring cable tensions, which include the pre-tension, balance the environmental loads and all static forces applied on the platform.

The mooring cable tensions can be obtained as:

$$\mathbf{T}_i = k\Delta L_i \tag{3.83}$$

where

$$\Delta L_i = L_{i,2} - L_{i,1}$$

$$L_{i,j} = \sqrt{\left[\boldsymbol{P_j} + \boldsymbol{b}_{i,j} - \boldsymbol{a}_i\right]^T \left[\boldsymbol{P_j} + \boldsymbol{b}_{i,j} - \boldsymbol{a}_i\right]} \qquad i = 1, \ldots, \text{n. } j = 1,2.$$

k is the mooring cable stiffness for 1 m of mooring cable length, and ΔL_i is the change in the mooring cable length due to the effect of the external forces.

3.10 Global Analysis

Since the mooring cable tensions and platform displacements vary with time, the Root Mean Square (RMS) measure will be used to quantify the tensions and displacements in each location. The RMS measure is expressed as:

$$w_{RMS} = \sqrt{\frac{1}{n}(w_1^2 + ... + w_i^2 + \cdots + w_n^2)} \tag{3.84}$$

where w_i is the value at a specific time.

3.11 Degree of rigidity Analysis

A key characteristic property of any multi-degree dynamic system is its natural frequencies. The natural frequencies of the marine platform, in Hertz, can be calculated from [92]

$$f_j^k = \frac{\sqrt{eig_j\left([\mathbf{M}(\mathrm{x})]^{-1}[\mathbf{K}(\mathrm{x})]^k\right)}}{2\pi} \tag{3.85}$$

where f_j^k is the jth natural frequency of the moving platform at certain platform location (k); $eig_j\ (matrix)$ is the jth eigenvalue of the matrix; $[\mathbf{K}(\mathrm{x})]^k$ is the stiffness matrix of the moving platform calculated at the location (k); $\mathbf{M}(\mathbf{x})$ is the mass matrix of FCDP.

In order to assess the degree of rigidity of a flexible system, one can use the system's natural frequencies as indicators. Simply, a lower natural frequency indicates lower stiffness and/or higher inertia. For the movable platform, the system's natural frequencies are functions of the floating structure location. Therefore, the platform has different degrees of degree of rigidity when the floating structure is at different locations at the sea surface.

3.12 Chapter Summary

In this chapter, an efficient universal mathematical model was developed to describe the kinematics and dynamics of any floating cable driven/moored platforms in a static/wavy water environment.

The added mass matrix was established using strip theory and the flat disk approach for the FCDP. Particular attention was given to the stiffness matrix of the FCDP; it was developed based on the Jacobean manipulator concept and it was derived in three parts: the first part is due to the mooring cables' strengths, the second part is due to the mooring cables' tensions, and the third part is due to the water's effect. Viewing previous floating marine platform literature, this is the first time that the stiffness matrix has been derived based on the manipulator concept for an FCDP. The mass, damping, and stiffness matrices were established for the FCDP as a function of the platform position.

Also, the offshore environmental loads were estimated and the solution for the equation of motion of the FCDPs was found. Finally, measures such as the degree of rigidity, mooring

cables' tensions, and minimum submerged depth were mentioned to assess the mobility and the degree of rigidity of the FCDPs within their effective area.

CHAPTER 4
Analysis of a Floating Movable Cylindrical Platform

4.1 Introduction

Based on the universal marine platform mathematical model outlined previously, a numerical model was developed for predicting the floating cable-driven platform (FCDP) motions. Therefore, it was decided to conduct several study phases in this chapter. Preliminary results were produced in a static environment, which gave a general idea about a floating movable cylindrical platform's (FMCP) characteristics and features.

In Section 4.2, two FMCP configurations are considered for static analysis. The mooring cables' tensions, effective area and the degree of rigidity of the two configurations are studied in Section 4.3 to highlight the most suitable FMCP configuration in a marine environment.

In Section 4.4 a dynamical study is conducted for the suitable FMCP configuration obtained from Section 4.3. Fluctuations in surge, sway, heave, roll, pitch and yaw motion responses are generated to show the motion of the FMCP in the sea wave frequency-exciting forces.

In Section 4.5, the FMCP effective area is studied. Also, the minimum submerged depth required, at each location in the effective area of the FMCP, is determined. In addition, the total mooring cables' tensions, the displacement motion and degree of rigidity of the FMCP are studied over its effective area.

Mooring cables lose their characteristics due to the sea's side effects and time factors. For these reasons, a parametric study is carried out, in Section 4.6, on the change of mooring cable stiffness and pre-tension, to show the effect of changing mooring cables' characteristics on the motion's response. Finally, mooring cable failure can occur due to overloads, the sea's side effects and time factors. For these reasons, a failure analysis is conducted, in Section 4.7, on the mooring system to show the effect of failure on the FMCP dynamic motion.

The purposes of this chapter are to investigate the performance of the FMCP, to provide an understanding of where a FMCP can work, and how much of its degree of rigidity is in every location in its effective area.

The general layout of the FMCP is shown in Figure 4.1. It consists of six mooring cables which are driven by reels/motors (mounted on the top surface of the moving structure of the FMCP) and in the other direction is fixed to the seabed. It consists of six mooring cables arranged in a form similar to the Stewart Gough parallel robot, depicted in Figure 4.2.

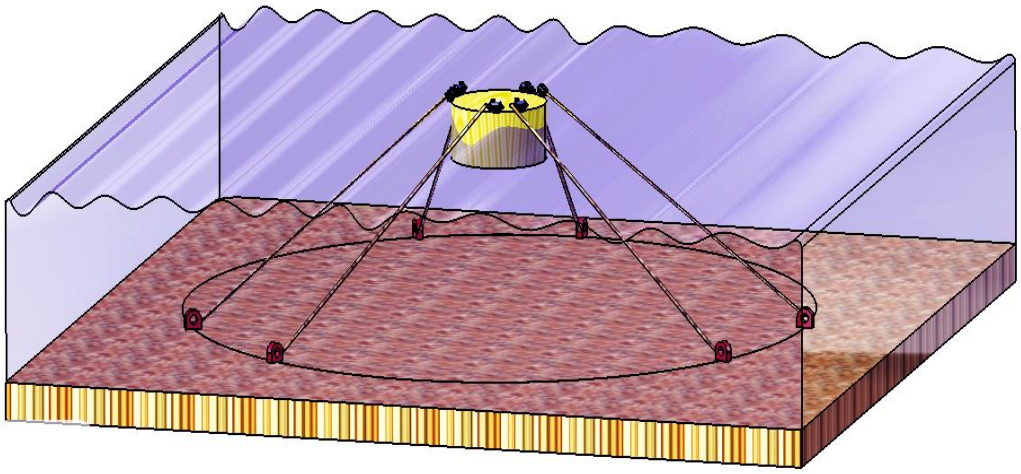

Figure 4.1: General FMCP configuration.

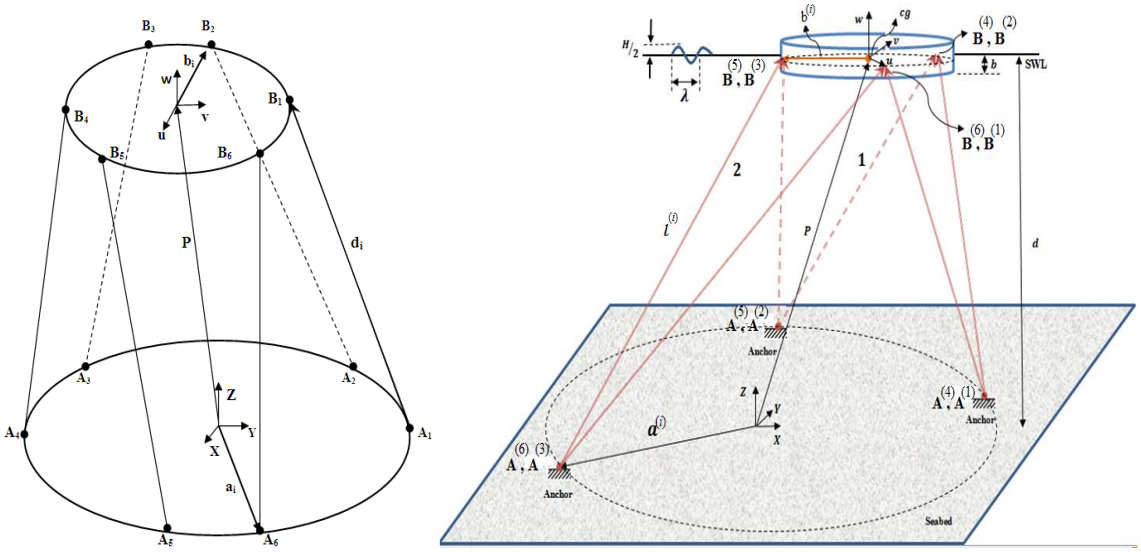

Figure 4.2: General FMCP 6-6 and 3-3 layouts.

4.2 Layouts of FMCP

Two common general layouts of the FMCP have been studied, which are shown in Figures 4.1 and 4.2. A fixed Cartesian frame of reference (X,Y,Z) is located at the center of an imaginary circle on the seabed. The six mooring cables are anchored to the seabed and these anchors are located on the imaginary circle perimeter at points $A_1, A_2, A_3, A_4, A_5,$ and A_6; see Figure 4.2. A movable Cartesian frame of reference (u,v,w) is located at the center of gravity (CG) of the moving structure. The six mooring cables are driven by six sets of reel-motor devices, which are hosted on the (u,v)-plane at points $B_1, B_2, B_3, B_4, B_5,$ and B_6.

Table 4.1 lists the important parameters' values of the FMCP and sea wave properties which are used to perform the FMCP analysis. These parameters and properties are based on several studies that were conducted in the Arabian Gulf [65-67].

Table 4.1: Simulation parameters [47, 54, 65-67, 74-76].

Designation	
Platform	
Moving Radius (a)	5 m
Seabed Radius (r)	200 m
Platform Height (h)	5 m
Platform Mass	39270 Kg
Water Depth (d)	50 m
Submerged Depth due to weight (b_w)	0.5 m
Stiffness (k_s)	30 KN/m
Damping ratio for surge	0.0027
Damping ratio for heave	0.0044
Damping ratio for sway	0.0026
Damping ratio for roll, pitch, and yaw	0.0005
Added mass coefficient (C_a)	1
Sea Wave	
Height	1 m
Time Period	5 sec

Depending on the arrangement of mooring cables, an FMCP is categorized into two different configurations, which are a 6-6 and a 3-3 FMCP. For example, the 3-3 FMCP has six mooring cables which are connected to the seabed with three different anchors' positions. At other end, every two mooring cables are connected at one position on the moving structure of the FMCP, which means that the FCDP has only three reels/motors on the moving structure. Figures 4.3 to 4.4 represent 2-D sketches for the two types of the FMCP configuration.

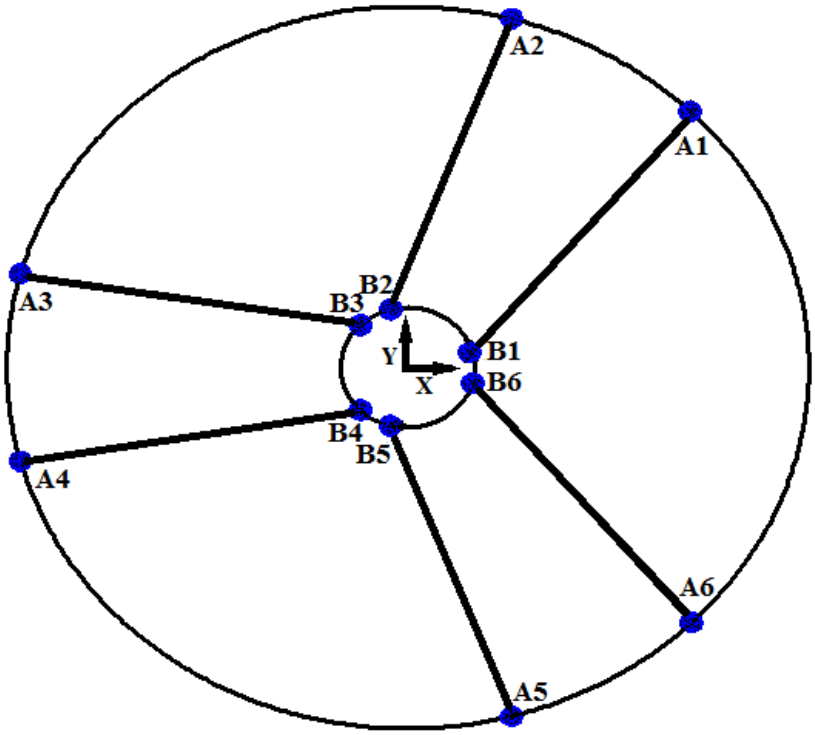

Figure 4.3: 2-D sketch for 6-6 FMCP.

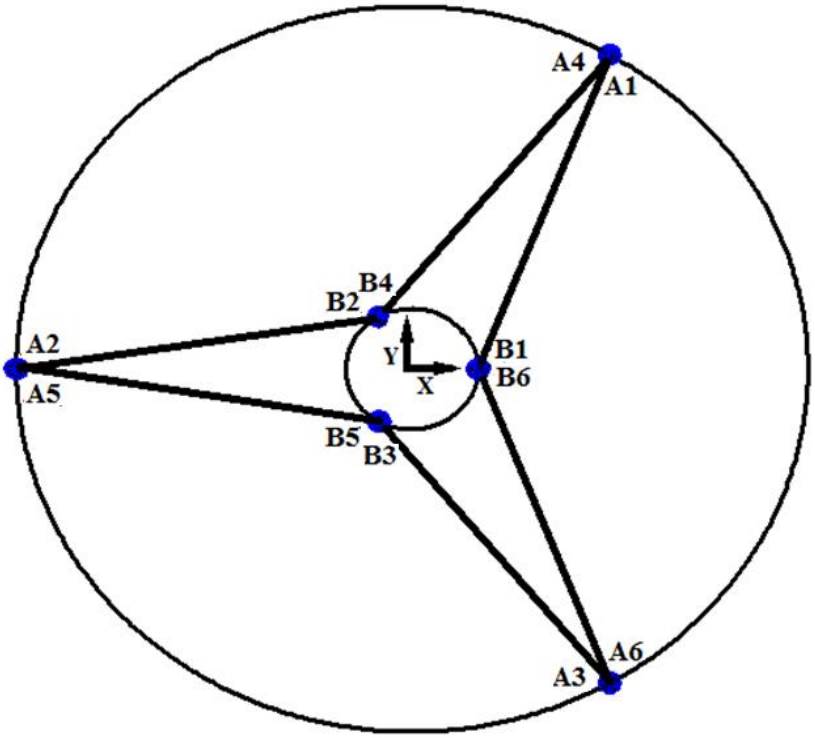

Figure 4.4: 2-D sketch for 3-3 FMCP.

Table 4.2: Anchors'/Motors' positions angles for FMCP.

Mooring cable Number\ Points	A_i (°)	B_i (°)
6-6 FMCP		
1	45	15
2	75	105
3	165	135
4	195	225
5	285	255
6	315	345
3-3 FMCP		
1	60	0
2	180	120
3	300	240
4	60	120
5	180	240
6	300	360

Table 4.2 represents the A_i and B_i position angles respectively for the two FMCP configurations to carry out the analysis. A_i values represent the angles between $a^{(i)}$ and the positive x-axis vectors (Figure 3.2). While, B_i values represent the angles between $b^{(i)}$ and the positive u-axis vectors (Figure 3.2).

Table 4.3: Natural frequencies for FMCPs, at the center location and $b = 1$ m.

Natural Frequencies (ω_n)	6-6 (rad/s)	3-3 (rad/s)
1	2.2975	2.1149
2	3.4489	5.4528
3	7.1691	7.3607
4	14.077	14.053
5	15.737	15.159
6	28.213	32.179

Table 4.3 represents the natural frequency values of the FMCP at the center location and a submerged depth of $b = 1$ m. The natural frequencies are higher than the sea wave frequency, which means there will not be a resonance or a beating phenomenon.

4.3 Static Analysis of FMCP

Two FMCP configurations are studied in this section (Figures 4.3 and 4.4) with the absence of the external environmental loads. This study is performed to see which one be the most suitable FMCP configuration, in a marine environment.

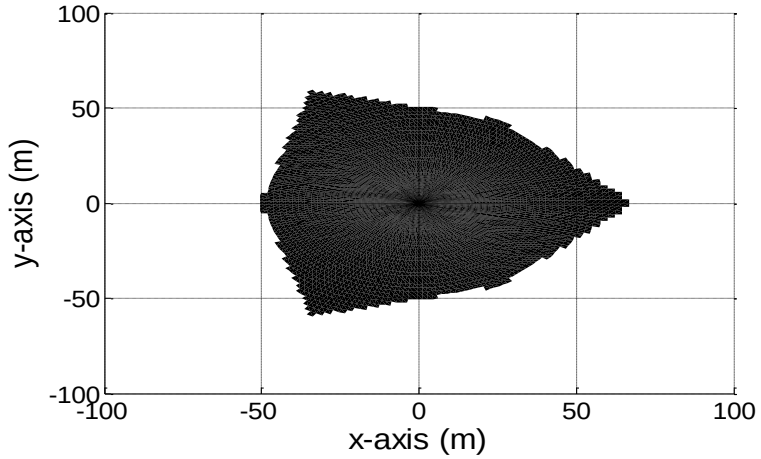

Figure 4.5: Effective area of the 6-6 FMCP.

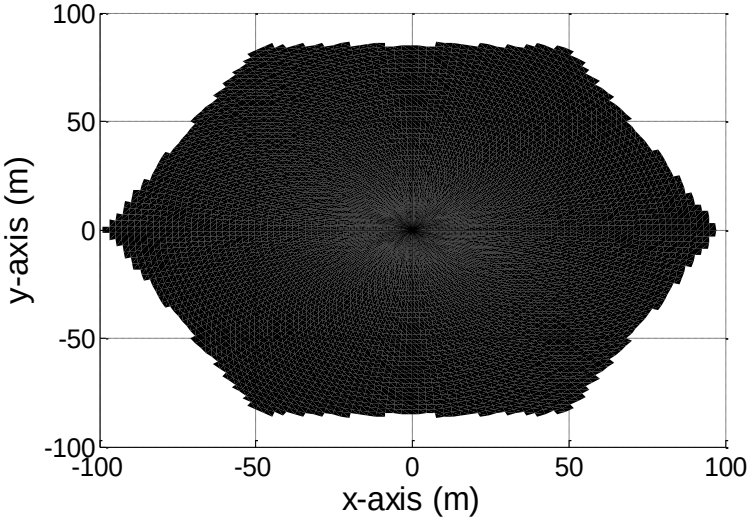

Figure 4.6: Effective area of the 3-3 FMCP.

Table 4.4: Effective area of FMCP for different configurations.

FMCP / Angles	$6-6$	$3-3$
Area (out of 40000 m^2)	22.49 %	62.75 %

Starting off, the effective area was checked for the two configurations of FMCP. To do that, it was required to have positive tensions in the mooring cables of the FMCP. Equation (3.83) is used to measure the mooring cable tensions, at all locations, to ensure non-negative mooring cable tensions. Figures 4.5 and 4.6 represent the effective area of the 6-6 FMCP and 3-3 FMCP respectively. As shown in Table 4.4, the larger effective area is acquired by the 3-3 FMCP.

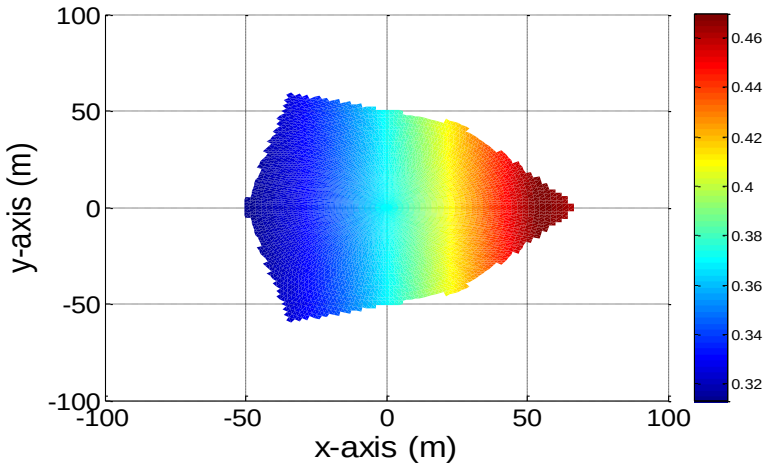

Figure 4.7: Minimum natural Frequencies (colour, Hz) of 6-6 FMCP.

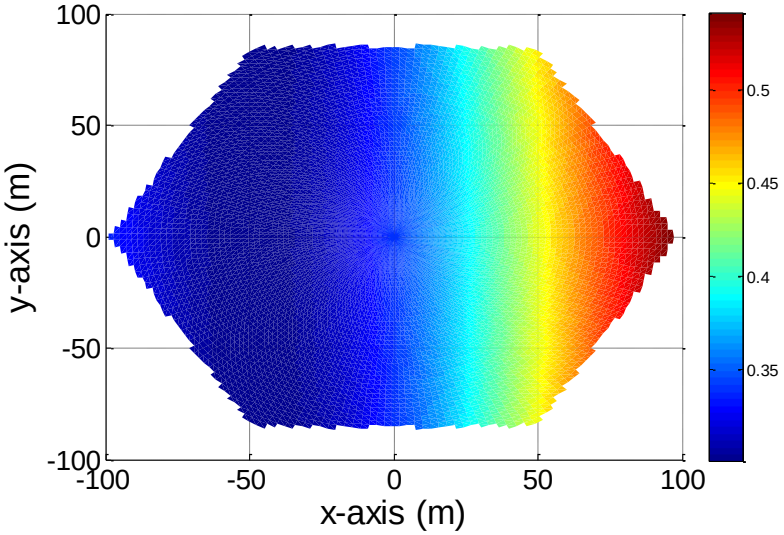

Figure 4.8: Minimum natural Frequencies (colour, Hz) of 3-3 FMCP.

The minimum natural frequency has been found, at all locations in the effective area for the two FMCP configurations, to show the FMCP degree of rigidity. Equation (3.85) is used to measure the minimum natural frequency to detect the degree of rigidity of the FMCP. Figures 4.7 and 4.8 represent the minimum natural frequency over the effective areas of the 6-6 FMCP and 3-3 FMCP respectively. As shown, the 3-3 FMCP has better degree of rigidity than the 6-6 FMCP. This means that the 3-3 FMCP is more rigid than the 6-6 FMCP.

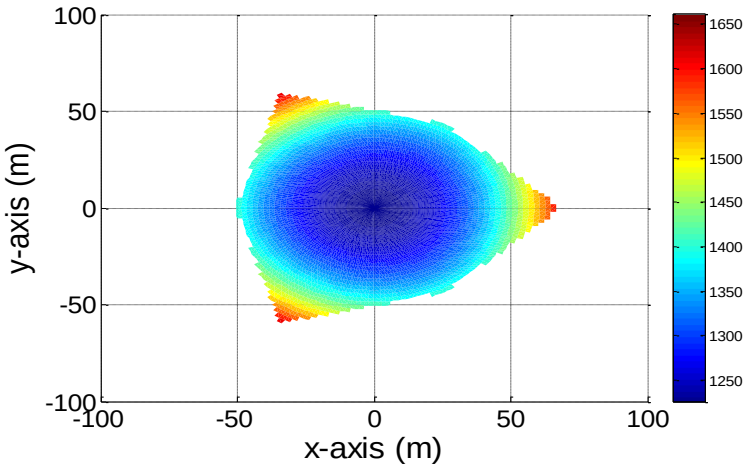

Figure 4.9: 2-norm tension values of the six mooring cables, (colour, N) at each location in the effective area of 6-6 FMCP.

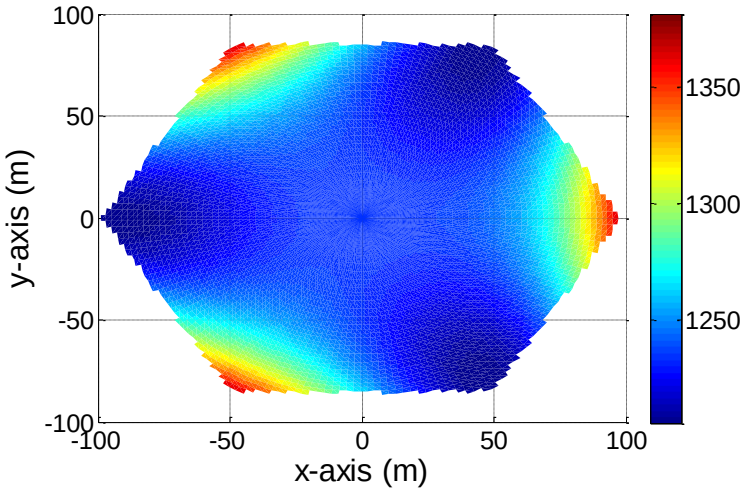

Figure 4.10: 2-norm tension values of the six mooring cables, (colour, N) at each location in the effective area of 3-3 FMCP.

The 2-norm tension values, of the six mooring cables of the FMCP were calculated at all locations in the effective area for the two FMCP configurations. Equation (3.83) was used to measure the six mooring cables' tension, then Equation (3.84) was used to find the Root Mean Square (RMS) of the six mooring cables' tensions to quantify the tensions in each location.

Figures 4.9 and 4.10 represent the 2-norm mooring cables' tensions value in the effective areas of the 6-6 FMCP and 3-3 FMCP respectively. Obviously, the 3-3 FMCP needs less mooring cable tension to work in the effective area without losing its degree of rigidity.

4.4 Dynamic Analysis of FMCP

Based on the previous section's analysis, the 3-3 FMCP is selected to do further study. The 3-3 FMCP is studied, in this section, when it is exposed to environmental loads. Figures 4.11 to 4.13 show the time history of sea wave forces applied on the floating platform, at a randomly chosen location of $x = 20\,m;\ y = 10\,m$ with respect to the fixed global coordinate frame (this location within the effective area and it chosen to have asymmetry mooring cables distribution, see Figure 4.11). Table 4.1 data is used to perform the dynamical analysis of the FMCP. In addition, the needed minimum submerged depth of b $\cong$ 0.9 m is used.

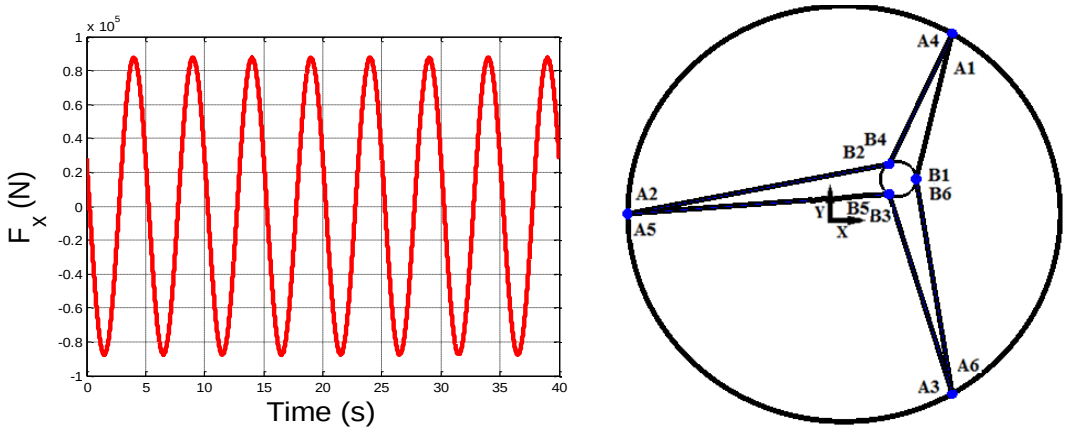

(Surge excitation force) (Top view of FMCP)

Figure 4.11: FMCP at location $x = 20\,m;\ y = 10\,m$ and b of 0.9.

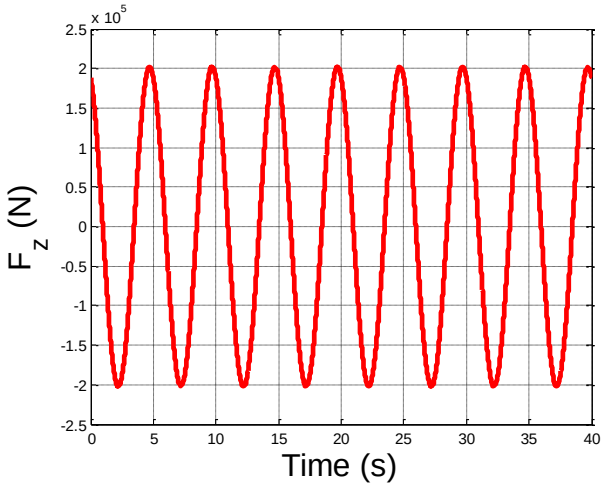

Figure 4.12: Heave excitation force on the FMCP at location $x = 20\ m;\ y = 10\ m$ and b of 0.9.

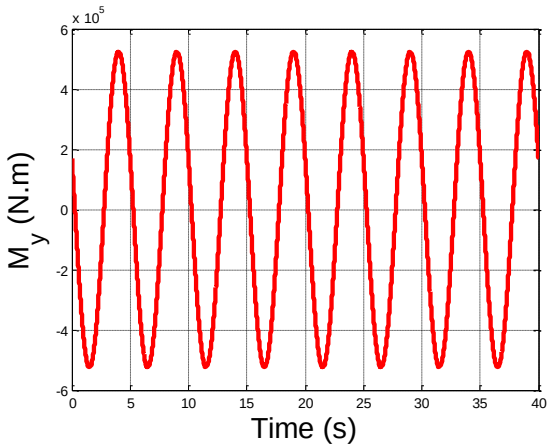

Figure 4.13: Pitch excitation force on the FMCP at location $x = 20\ m;\ y = 10\ m$ and b of 0.9.

To avoid the mooring cable slack of the 3-3 FMCP, it is required to have varying mooring cable tensions in the FMCP. Figure 4.14 shows the mooring cable tensions (calculated using Equation (3.83)) at location coordinates of $x = 20$ m, $y = 10$ m.

Using the submerged depth of b $\cong$ 0.9 m, the mooring cable pre-tensions $\bar{\tau} = [0.0629 \quad 1.7749 \quad 0.4 \quad 0.0011 \quad 1.7681 \quad 0.469]^T * 10^5\ N$ is the sufficient pre-tension needed at that location to ensure non-negative mooring cable tensions against the

dynamic wave forces. The Figure 4.14 represents the mooring cable tensions, include the pre-tension, which are needed to balance the sea wave and all static forces.

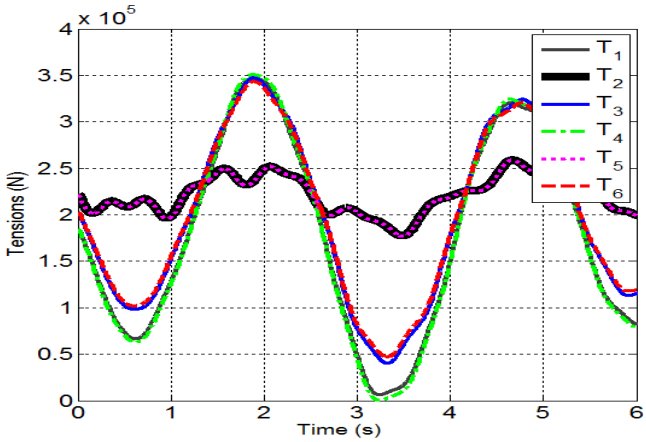

Figure 4.14: The six mooring cable tensions of the 3-3 FMCP.

As a reference case, let us consider the dynamic response of the FMCP that is excited by the sea wave loads, and whose center of gravity is located at the point (x = 20, y = 10), which indicates a submerged depth of 0.9m. The displacement responses are plotted in Figures 4.15 to 4.20, based on time steps of 0.1 second.

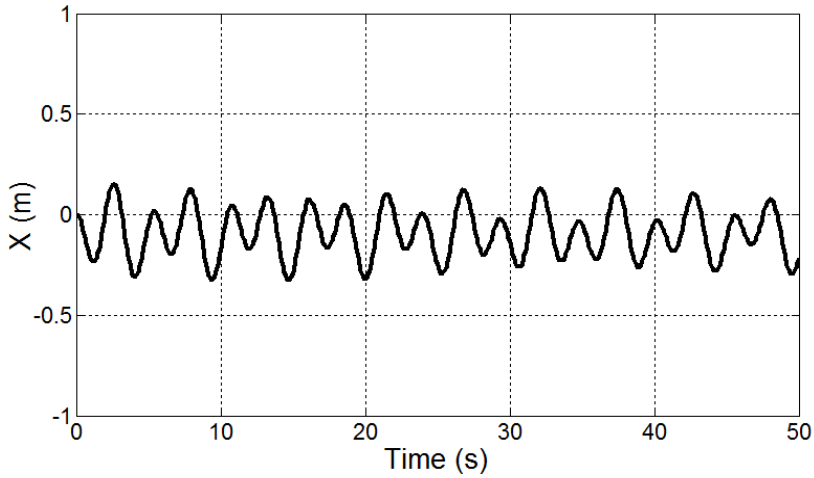

Figure 4.15: 3-3 FMCP surge displacement.

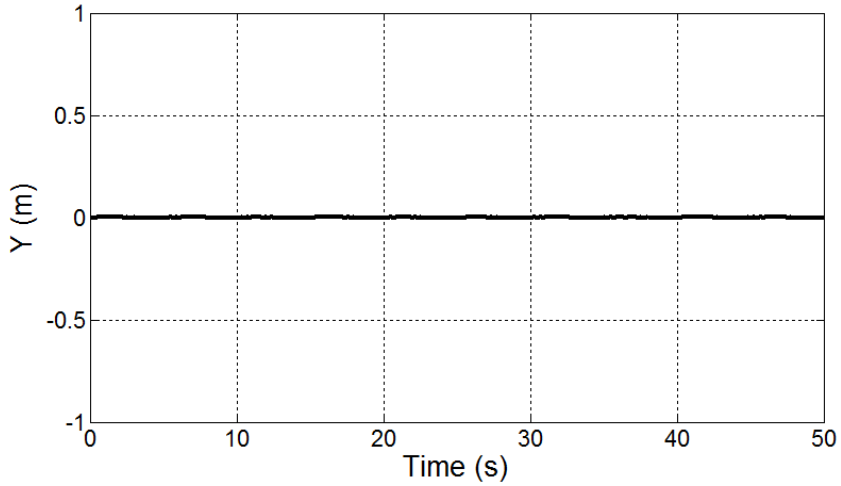

Figure 4.16: 3-3 FMCP sway displacement.

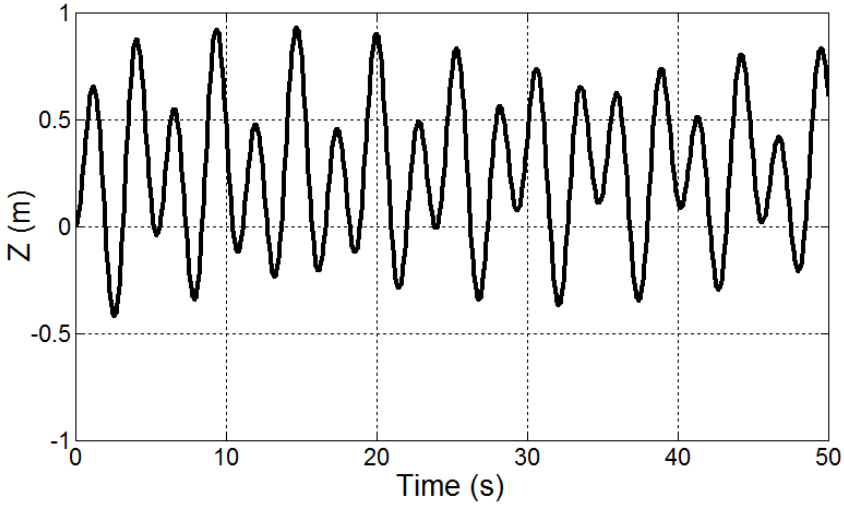

Figure 4.17: 3-3 FMCP heave displacement.

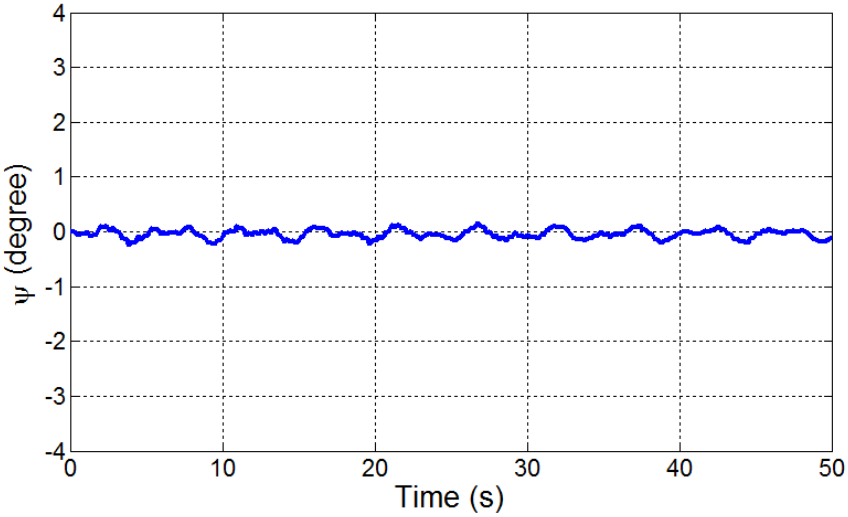

Figure 4.18: 3-3 FMCP roll rotation.

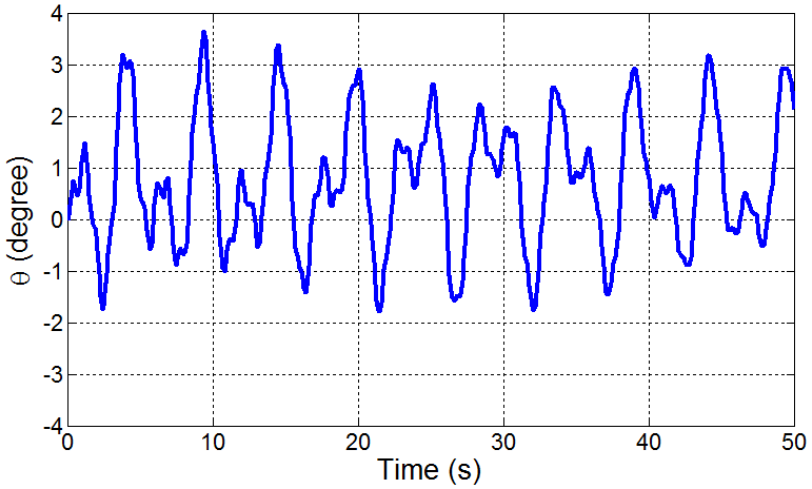

Figure 4.19: 3-3 Cable-driven marine platform pitch rotation.

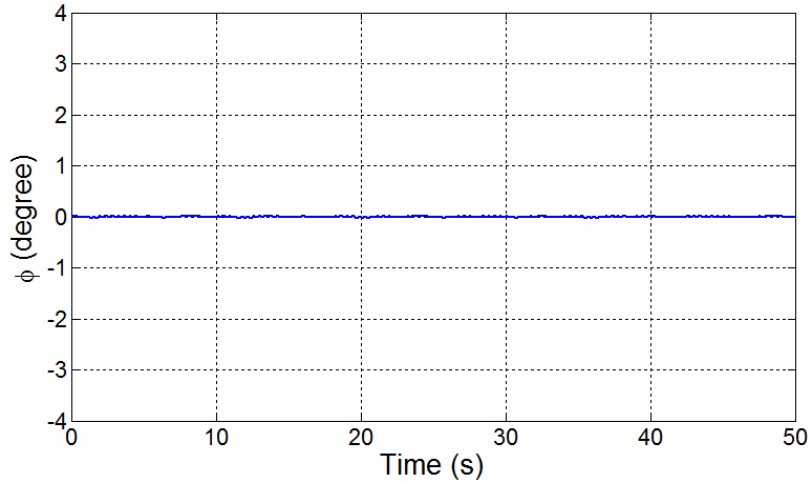

Figure 4.20: 3-3 FMCP platform yaw rotation.

The translational displacements of the platform center of gravity in the (u,v,w)-directions (surge, sway, and heave) and the rotational displacements about the (u,v,w)-axes (roll, pitch, and yaw) are shown as functions of time in Figures 4.15 to 4.20. It is observed that the dynamic response to the impinging sea waves is characterized by noticeable heave and surge and negligible sway, while performing a dominantly pitch rotation, since the rotations in the roll and yaw are negligible.

This fact is due to the cable distribution in the 3-3 FMCP configuration. As Figure 4.4 shows, the moving structure is connected with the seabed via three mooring cables, from

the positive Y direction. Likewise, three mooring cables, in the negative Y direction, are connected between the moving structure and the seabed. This connection allows the FMCP to be stiffer in the sway direction. On the other hand, the sway direction isn't directly affected by the sea wave loads and the motion response appears due to the dynamic coupling effects.

4.5 Effective Area and Degree of rigidity Analysis of FMCP

The effective area (shown in Figure 4.21) of the FMCP is represented by the area on the water surface that can allow the FMCP to work in without mooring cable slack. Figure 4.21 represents the metacentric height ($\overline{GM}$) within the effective area. The metacentric height is large at the darkest area in the effective area, then the platform is considered to be more stable in this area. It is shown that the metacentric height is small as the platform moves closer to the effective area edges, indicating less platform stability.

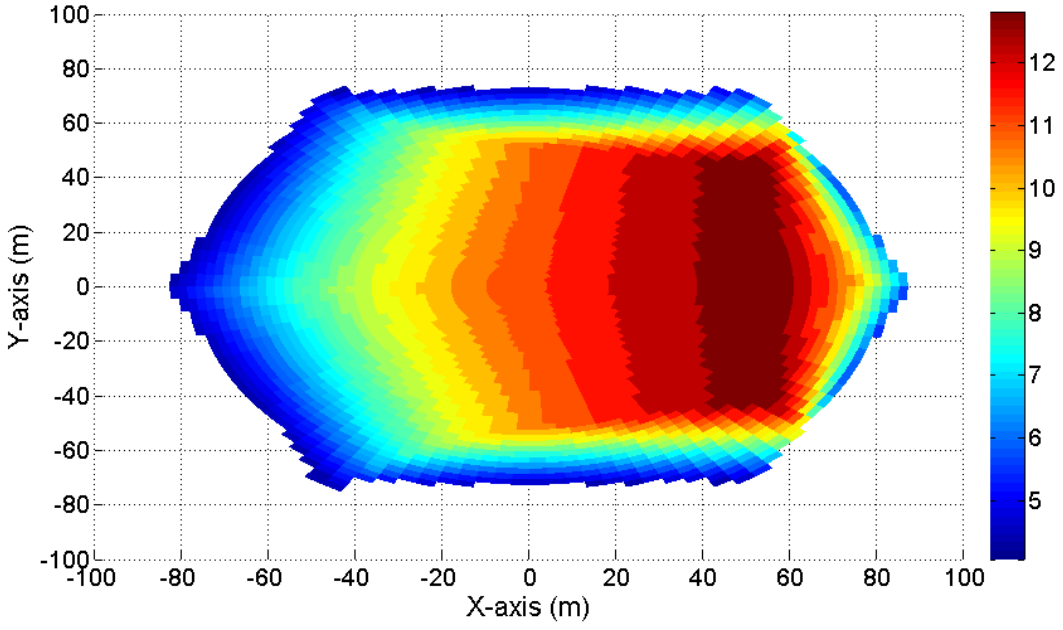

Figure 4.21: FMCP metacenter height within its effective area (m).

The dynamic analysis is performed at several discrete points, covering the effective area of the platform, to determine the variation of the FMCP dynamic performance. To keep the mooring cables taut throughout the effective area, positive tensions in the mooring cables have to be maintained by applying sufficient tensions. Because the sufficient mooring cable tensions are dependent on the location of the FMCP, the resulting submerged depth of the platform will be variable across the effective area. Figure 4.22 shows the variation of the minimum submerged depth across the effective area (shown in Figure 4.21). The minimum submerged depth increases as the FMCP moves closer to the effective area edges, due to changes in the mooring cable angle's directions (change in the stiffness of the FMCP).

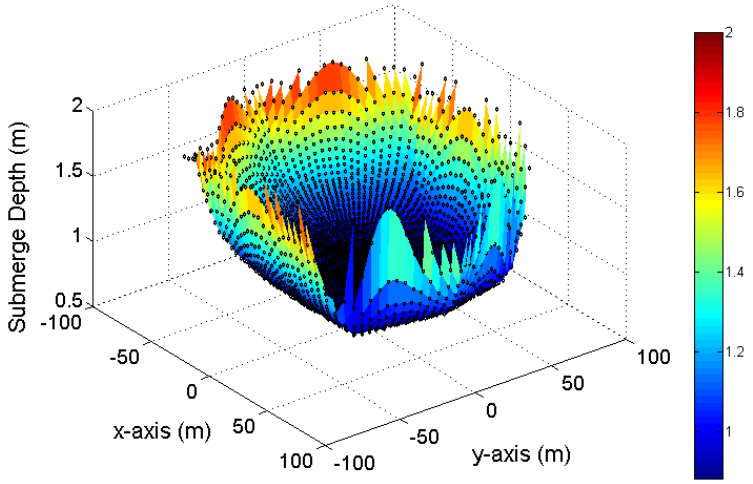

Figure 4.22: Minimum submerged depth required at each location in the effective area.

The dynamic analyses are conducted at discrete locations in the effective area, taking into account the variation of the submerged depth and mooring cable tensions. Since the mooring cable tensions and platform displacements vary with time, the Root Mean Square (RMS) measure will be used to quantify the tensions and displacements in each location. The RMS measure is expressed in Equation (3.84).

Figure 4.23 represents the 2-norm of the RMS values of the six mooring cables' tensions at each location in the effective area, for the minimum submerged depth displayed in Figure 4.22. Figure 4.23 indicates that higher mooring cable tensions are needed to avoid mooring cable slack as the platform moves closer to the effective area edges, and it is dominant as the FMCP moves to the negative X direction in the effective area.

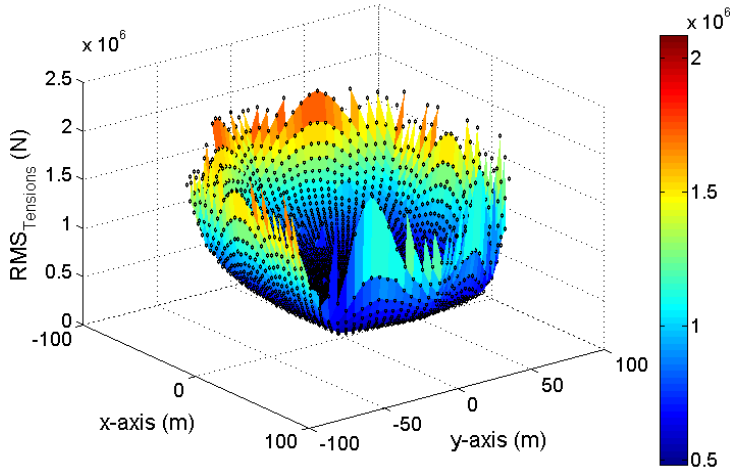

Figure 4.23: The 2-norm value of the six root mean square values of the mooring cables' tensions at each location in the effective area.

Figure 4.24 shows the minimum natural frequency of the FMCP at each location in the effective area, calculated from Equation (3.85). It is shown here that the minimum natural frequency (the stiffness) is higher as the FMCP moves to the positive X direction due to the kinematic of the mooring cables configuration.

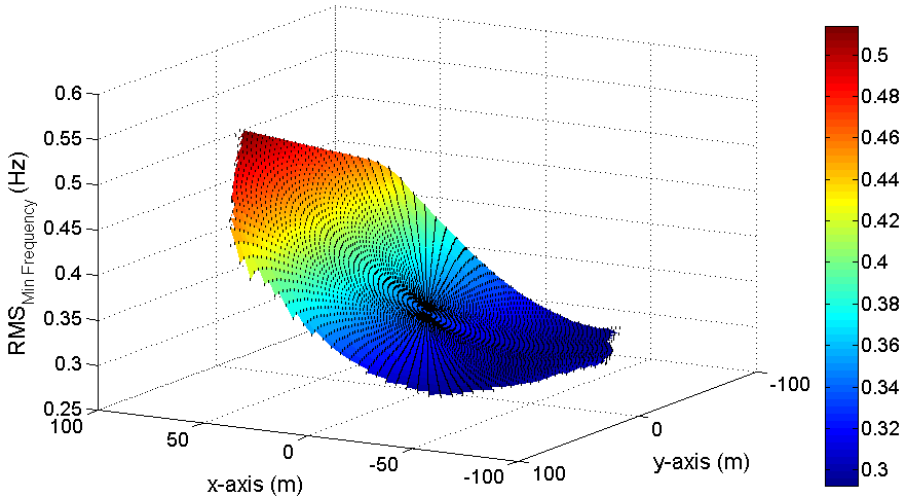

Figure 4.24: Minimum Frequency at each location in the effective area.

Figures 4.25 and 4.30 show the RMS values of the translational and rotational displacements at every location in the effective area, based on time steps of 0.1 second. It is noted that higher translational displacements are achieved in the surge and heave motions, compared to that in the sway motion, at the extreme negative x-central region of the spar platform effective area. In addition, higher rotational displacements are obtained in the roll and pitch motions, compared to the yaw motion, also at the extreme negative x-central region of the spar platform effective area.

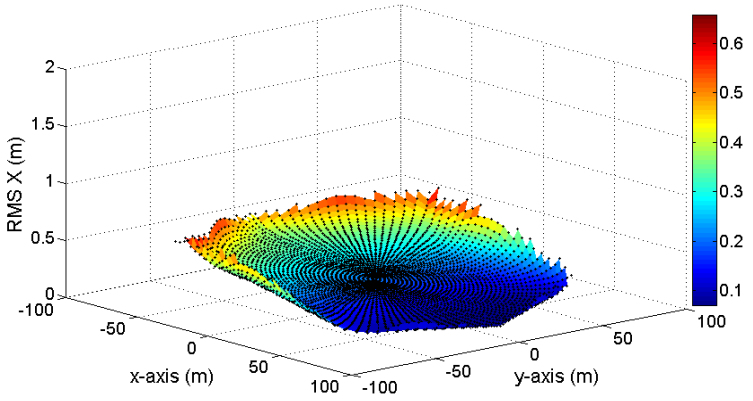

Figure 4.25: Root mean square values of FMCP surge displacement at each location in the effective area.

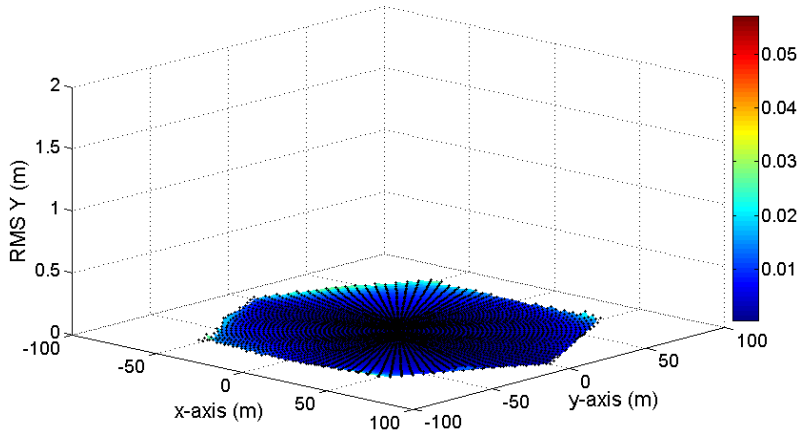

Figure 4.26: Root mean square values of FMCP sway displacement at each location in the effective area.

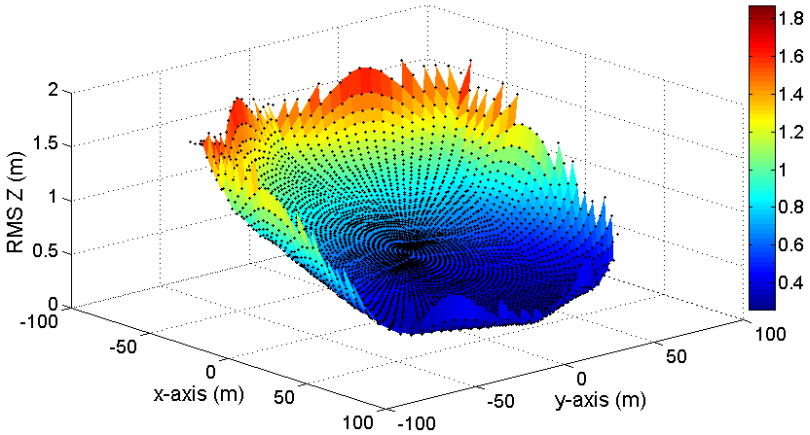

Figure 4.27: Root mean square values of FMCP heave displacement at each location in the effective area.

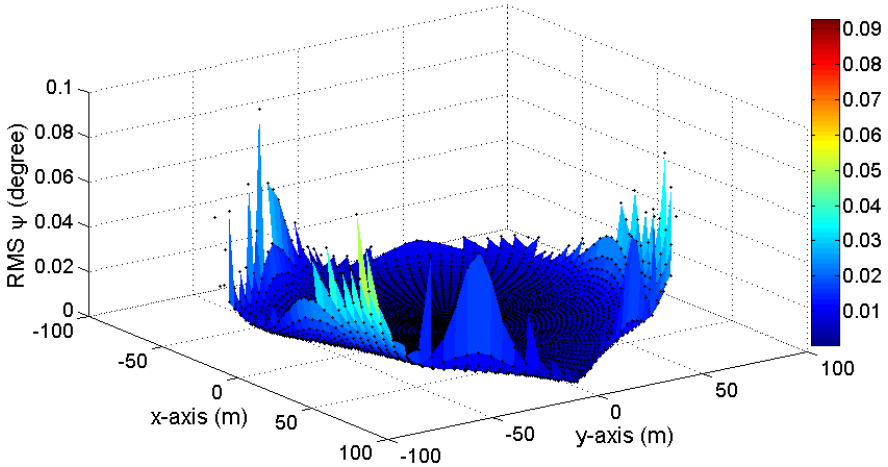

Figure 4.28: Root mean square values of FMCP roll displacement at each location in the effective area.

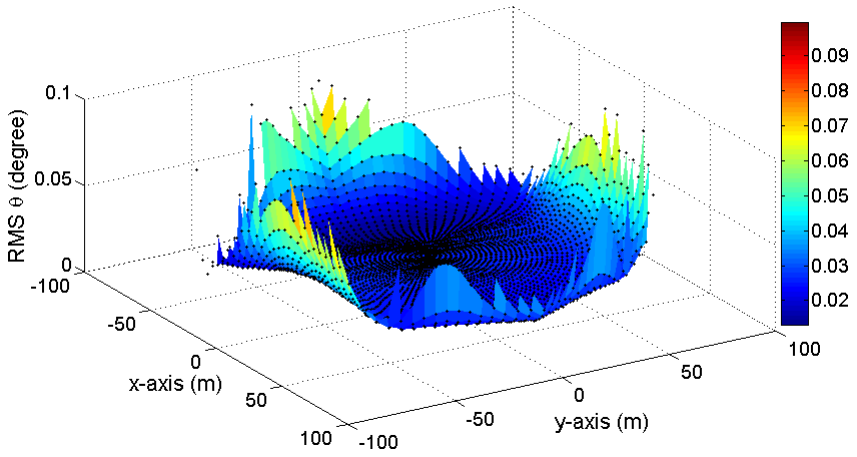

Figure 4.29: Root mean square values of FMCP pitch displacement at each location in the effective area.

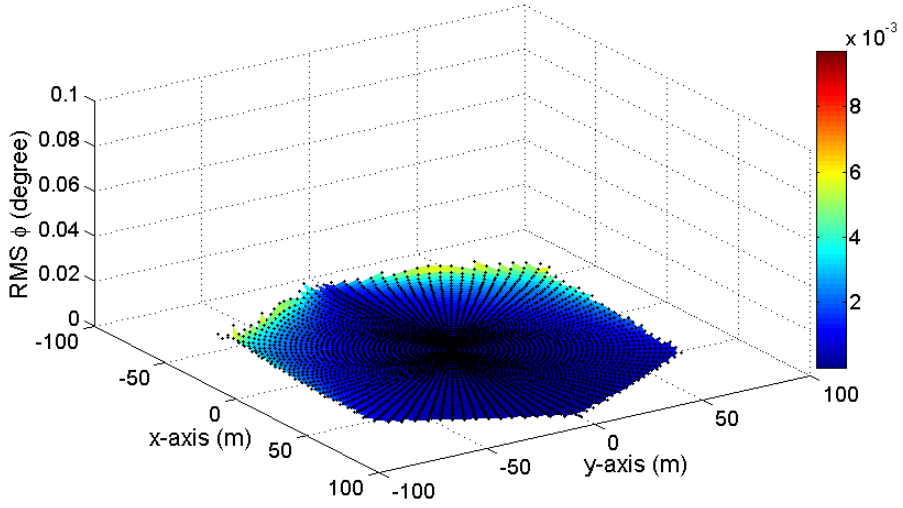

Figure 4.30: Root mean square values of FMCP yaw displacement at each location in the effective area.

4.6 Cable Stiffness and Cable Pre-Tension Effects

Naturally, mooring cables lose their characteristics due to the sea's side effects and time factors. For this reasons, a parametric study is carried out on the change of mooring cable properties (stiffness and pre-tension).

This section investigates the effect of increasing/decreasing the mooring cables stiffness and pre-tensions on the dynamic behavior of the FMCP. The mooring cable stiffness ($k_1 =$

$30 * 10^3$ N/m) used in the previous study is increased to $k_2 = 60 * 10^3$ N/m, then dynamical analysis is conducted for the two cases at a location of x = 20 m, y = 10 m, and a submerged depth of b = 0.9 m.

Figures 4.31 to 4.36 shows that increasing the mooring cable stiffness decreases the amplitude displacement of the FMCP. In addition, the displacement response are shifted to the left, due to the increase in the mooring cable stiffness. This result is in agreement with the nature of the cable.

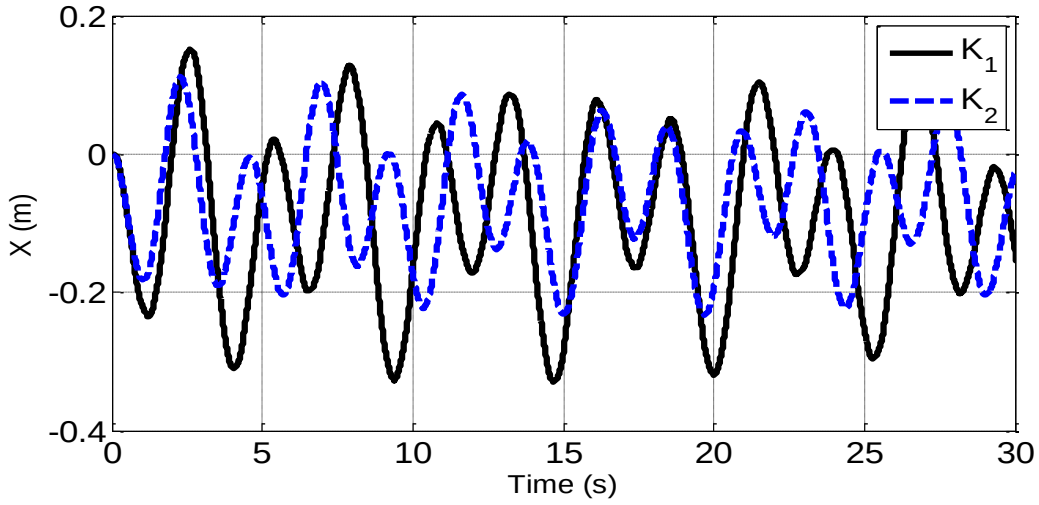

Figure 4.31: FMCP surge displacement with $k_1 = 30 * 10^3$ N/m and $k_2 = 60 * 10^3$ N/m.

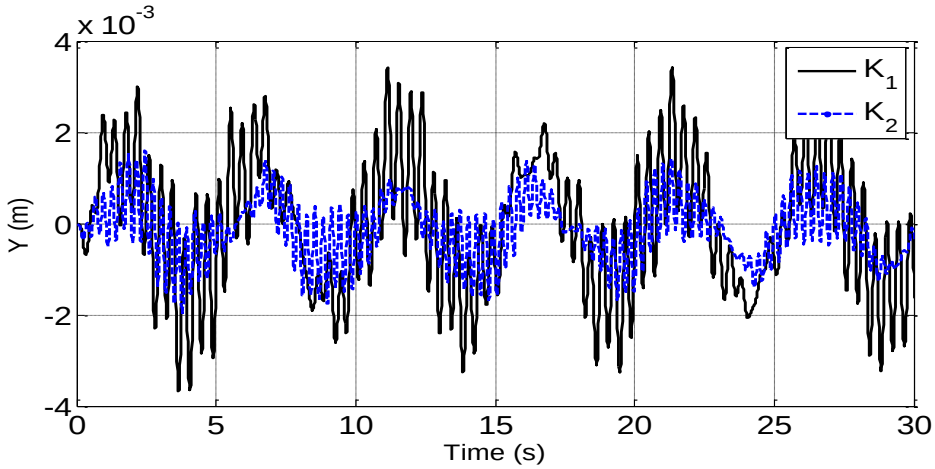

Figure 4.32: FMCP sway displacement with $k_1 = 30 * 10^3$ N/m and $k_2 = 60 * 10^3$ N/m.

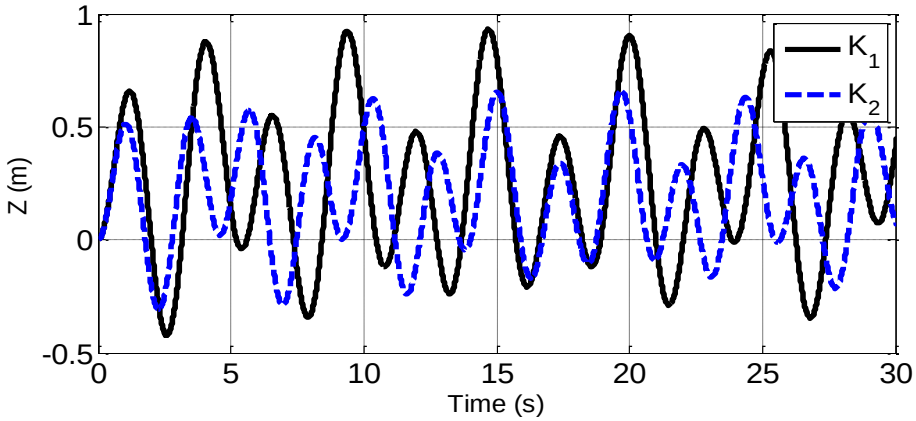

Figure 4.33: FMCP heave displacement with $k_1 = 30 * 10^3$ N/m and $k_2 = 60 * 10^3$ N/m.

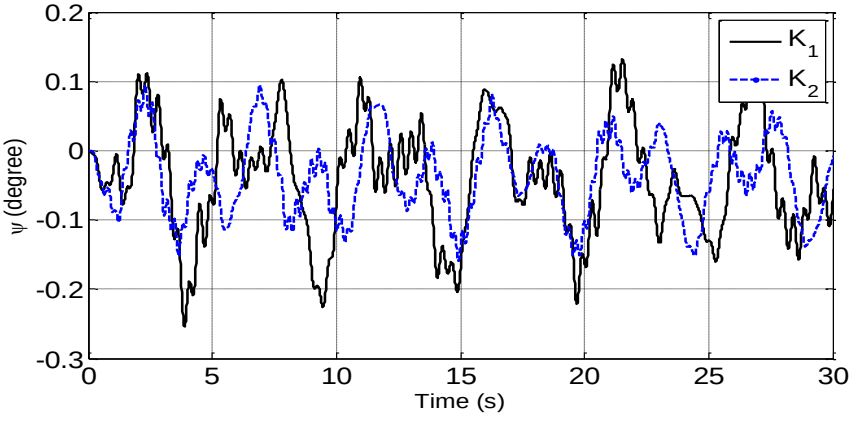

Figure 4.34: FMCP roll displacement with $k_1 = 30 * 10^3$ N/m and $k_2 = 60 * 10^3$ N/m.

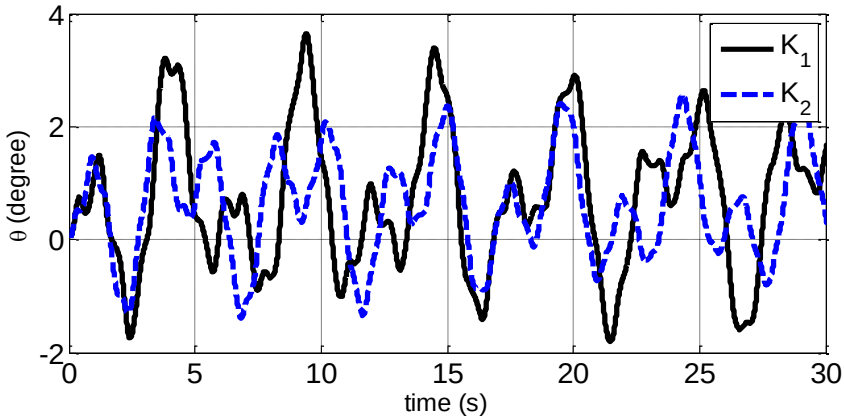

Figure 4.35: FMCP pitch displacement with $k_1 = 30 * 10^3$ N/m and $k_2 = 60 * 10^3$ N/m.

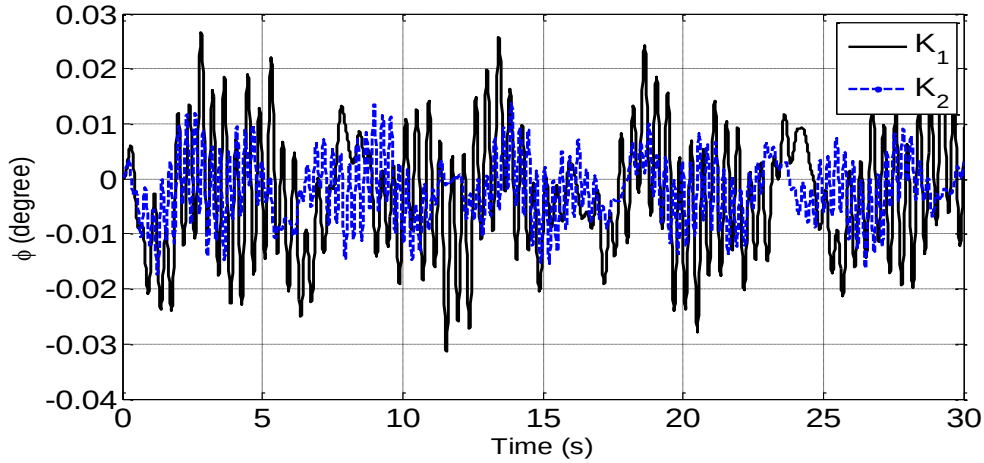

Figure 4.36: FMCP yaw displacement with $k_1 = 30 * 10^3$ N/m and $k_2 = 60 * 10^3$ N/m.

Table 4.5 represents the dynamical analysis for different mooring cables' stiffness cases. It shows the effect of varying the mooring cable stiffness on the dynamic behavior of the FMCP. The RMS values of the displacement, velocity and acceleration are calculated for different values of mooring cable stiffness at the location x = 20 m, y = 10 m and the submerged depth b = 0.9 m. Table 4.5 shows that increasing the mooring cable stiffness decreases the displacements, velocities and accelerations of the FMCP when it is exposed to the environmental loads.

Table 4.5: Effect of mooring cable stiffness on FMCP RMS dynamic displacements, velocities, and accelerations.

Stiffness (k_s) (N/m) $*10^3$	X (m)	Y (m)	Z (m)	ψ (rad)	θ (rad)	φ (rad)	$\dot{X}$ (m/s)	$\dot{Y}$ (m/s)	$\dot{Z}$ (m/s)
30	0.1515	0.0014	0.4289	0.0016	0.0257	0.0002	0.2584	0.0122	0.7193
60	0.1087	0.0007	0.3075	0.0012	0.0195	0.0001	0.2069	0.0088	0.5784
90	0.0846	0.0005	0.2392	0.0009	0.0156	0.0001	0.1767	0.0070	0.4946
120	0.0693	0.0004	0.1958	0.0008	0.0129	0.0001	0.1560	0.0060	0.4368

Stiffness (k_s) (N/m) $*10^3$	$\dot{\psi}$ $(\frac{rad}{s})$	$\dot{\theta}$ $(\frac{rad}{s})$	$\dot{\varphi}$ $(\frac{rad}{s})$	$\ddot{X}$ (m/s^2)	$\ddot{Y}$ (m/s^2)	$\ddot{Z}$ (m/s^2)	$\ddot{\psi}$ $(\frac{rad}{s^2})$	$\ddot{\theta}$ $(\frac{rad}{s^2})$	$\ddot{\varphi}$ $(\frac{rad}{s^2})$
30	0.0049	0.0453	0.0020	0.6641	0.1820	1.6426	0.0603	0.2045	0.0299
60	0.0036	0.0370	0.0014	0.6200	0.1825	1.5338	0.0593	0.1804	0.0300
90	0.0030	0.0321	0.0011	0.5929	0.1806	1.4683	0.0571	0.1678	0.0291
120	0.0026	0.0285	0.0010	0.5723	0.1768	1.4195	0.0556	0.1590	0.0284

Table 4.6 shows the effect of varying the submerged depth, due to the increase of mooring cable pre-tension on the dynamic behavior of the FMCP. The RMS values of the displacements and velocities and accelerations are calculated with different values of submerged depth $\bar{b}$ for the location x = 20 m, y = 10 m. Table 4.6 shows that increasing the pre-tension increases the displacements, velocities and accelerations of the FMCP when it is exposed to environmental loads. This is due to the fact that increasing the mooring cable tensions increases the stiffness of the FMCP.

Table 4.6: Effect of submerged depth due to mooring FMCP RMS dynamic displacements, velocities, and accelerations.

$\bar{b}$ (m)	X (m)	Y (m)	Z (m)	ψ (rad)	θ (rad)	φ (rad)	$\dot{X}$ (m/s)	$\dot{Y}$ (m/s)	$\dot{Z}$ (m/s)
0.9	**0.1515**	**0.0014**	**0.4289**	**0.0016**	**0.0257**	**0.0002**	**0.2584**	**0.0122**	**0.7193**
1.0	**0.1748**	**0.0016**	**0.4952**	**0.0019**	**0.0293**	**0.0002**	**0.2882**	**0.0130**	**0.8007**
1.1	**0.1990**	**0.0019**	**0.5639**	**0.0022**	**0.0335**	**0.0002**	**0.3188**	**0.0135**	**0.8841**
1.2	**0.2237**	**0.0022**	**0.6344**	**0.0026**	**0.0382**	**0.0003**	**0.3502**	**0.0146**	**0.9694**

$\bar{b}$ (m)	$\dot{\psi}$ $(\frac{rad}{s})$	$\dot{\theta}$ $(\frac{rad}{s})$	$\dot{\varphi}$ $(\frac{rad}{s})$	$\ddot{X}$ (m/s^2)	$\ddot{Y}$ (m/s^2)	$\ddot{Z}$ (m/s^2)	$\ddot{\psi}$ $(\frac{rad}{s^2})$	$\ddot{\theta}$ $(\frac{rad}{s^2})$	$\ddot{\varphi}$ $(\frac{rad}{s^2})$
0.9	**0.0049**	**0.0453**	**0.0020**	**0.6641**	**0.1820**	**1.6426**	**0.0603**	**0.2045**	**0.0299**
1.0	**0.0056**	**0.0506**	**0.0022**	**0.7574**	**0.1927**	**1.8382**	**0.0682**	**0.2310**	**0.0323**
1.1	**0.0063**	**0.0566**	**0.0023**	**0.8537**	**0.1982**	**2.0326**	**0.0740**	**0.2613**	**0.0337**
1.2	**0.0071**	**0.0632**	**0.0025**	**0.9484**	**0.2113**	**2.2257**	**0.0824**	**0.2941**	**0.0363**

4.7 Mooring Cable Failure Analysis

Naturally, mooring cables lose their characteristics due to the sea's side effects and time factors. For this reasons, a failure analysis is carried out on the mooring system of the FMCP. This section investigates the effect of a mooring cable failure (mooring cable break) on the dynamic behavior of the FMCP. The center location x = 0 m, y = 0 m, and the submerged depth b = 2 m were used to conduct this analysis.

Two study cases were conducted in this section. The first case is without a mooring cable failure and the second case is with the mooring cable failure; then the dynamical response

analysis of the FMCP was conducted. The FMCP position is fixed while the dynamical response was analyzed, which means the results of this particular study present only the first moment of failure to show the instability of the system after mooring cable failure.

Figures 4.37 to 4.42 show the motion response of the FMCP with and without mooring cable failure. Mooring cables 1 were chosen to conduct this analysis. As can be seen from these figures, the instability of the motion response in all degrees of freedom appear from the first moments.

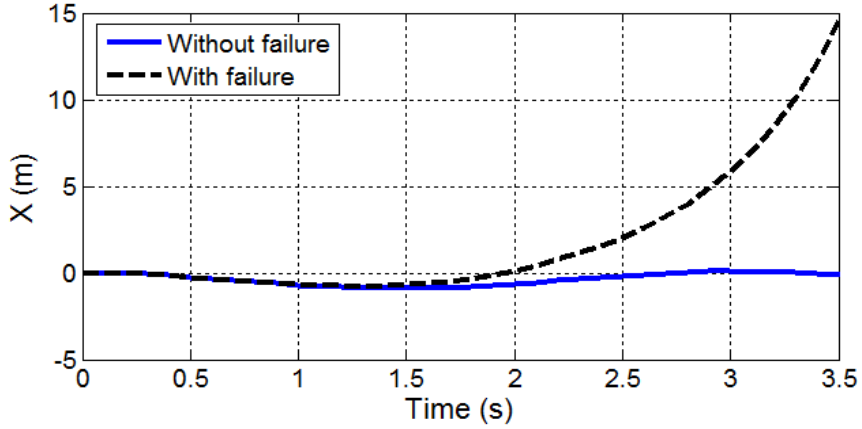

Figure 4.37: FMCP surge displacement with/without failure in mooring cable 1.

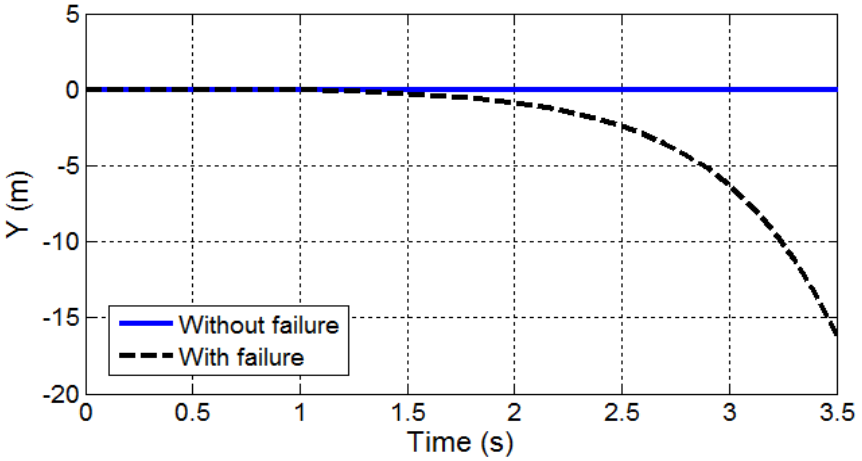

Figure 4.38: FMCP sway displacement with/without failure in mooring cable1.

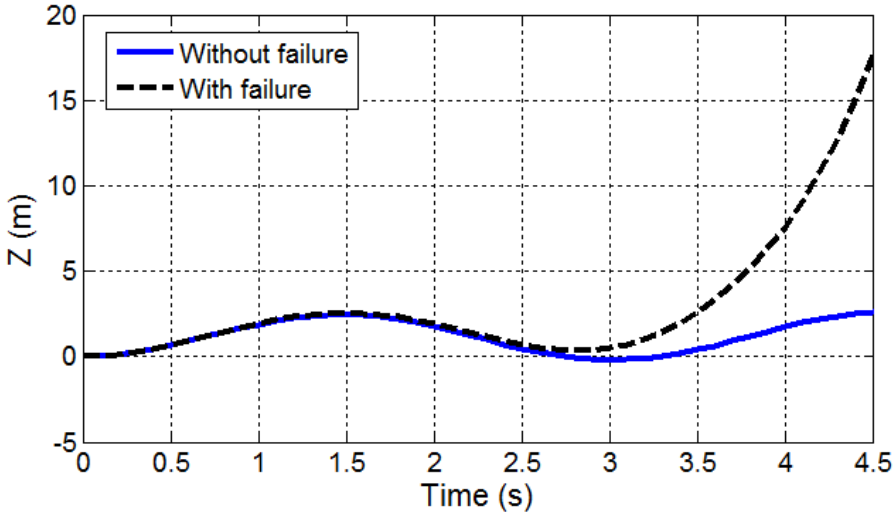

Figure 4.39: FMCP heave displacement with/without failure in mooring cable 1.

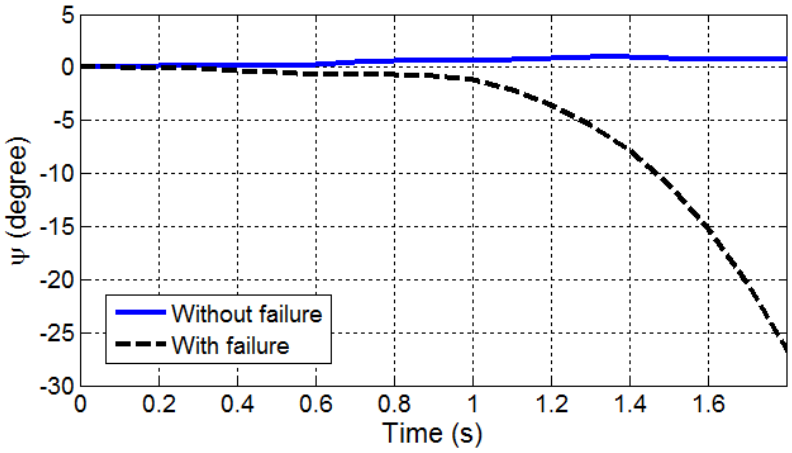

Figure 4.40: FMCP roll displacement with/without failure in mooring cable 1.

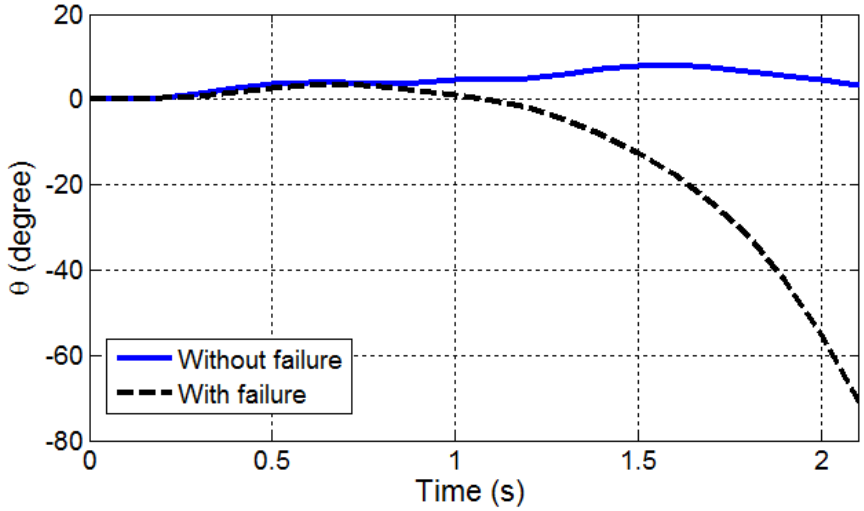

Figure 4.41: FMCP pitch displacement with/without failure in mooring cable 1.

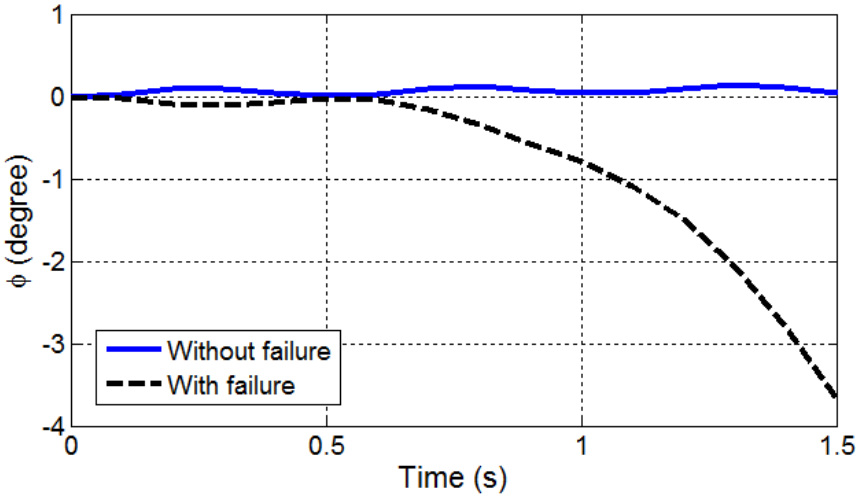

Figure 4.42: FMCP yaw displacement with/without failure in mooring cable 1.

In conclusion, the previous analysis proves the credibility of the condition mentioned in Chapter 2, which states that the number of mooring cables should be equal to the number of degrees of freedom to have a fully constrained platform in the sea [68].

4.8 Chapter Summary

The new concept of a movable marine platform was applied in this chapter. The effective area, and degree of rigidity within the effective area, were used to perform the dynamical analysis for a movable platform. Moreover, the stiffness matrix which is used in the dynamical analysis was calculated through the new approach, mentioned in chapter three.

Additionally, dynamic analysis was conducted on an FMCP in a marine environment. The FMCP was driven by six mooring cables anchored to the seabed and they were hosted by reels/motors mounted on the moving structure. Local dynamic analysis at a single location

was conducted, showing the mooring cable tensions and dynamic response when the FMCP is exposed to environmental loads.

A global dynamic analysis was conducted using RMS measures of the mooring cable tensions and FMCP displacement across the effective area. The platform positive tensions were maintained by varying the submerged depth to balance the variable sea wave forces. The minimum submerged depth, to ensure taut mooring cables, was plotted across the effective area and showed higher values near the effective area edges; this indicated that higher mooring cable tensions are required near the edges. It was also shown that increasing the mooring cable stiffness or decreasing the pre-tension results in a decrease of the RMS values of the platform displacements, velocities and accelerations. Failure analysis was conducted, at a fixed position, on the FMCP. A study of one mooring cable failure showed that the FMCP has unstable motion response in all degrees of freedom from the first moments of failure.

CHAPTER 5
Experimental Study

5.1 Introduction

As indicated previously, the mathematical model was developed for predicting the FCDP motions and the mooring cable tensions. Furthermore, an experimental study was carried out in a small basin to study the floating cable-driven platform (FCDP) behavior. A MatLab code was developed for the FCDP dynamics. The numerical results obtained from the code were compared with the corresponding experimental measurements. This comparison mainly aimed to verify the mathematical model developed.

In this chapter, experimental setup of the FCDP, mooring cable system and environment basin are described. Moreover, the data acquisition systems and the instrumentation for the test are highlighted.

5.2 Experimental Study

This model test was conducted for two purposes. One was to investigate the performance of the FCDP in a static environment and the other was to provide experimental data for mathematical model validation.

5.2.1 Test Facilities and Instrumentations

5.2.1.1 Basin

The Laboratory is equipped with a small square basin of 1195 mm length and width. The small basin, (shown in Figure 5.1), is constructed from 15 mm Plexiglas sheets. The sheets

are bonded together via a special cementing compound. The external dimensions of the Plexiglas tub are 1195mm x 1195mm x 615mm.

The frame of the tube is constructed from high-end waterproof aluminum extrusions for the sake of assembly, adjustment, and future expansion and reconfiguration. Structural angle brackets or gussets of adequate size reinforced the frame connections. The frame serves many structural requirements: holding the Plexiglas tub, raising the tub above the floor, providing foot-pad adjustment for uneven ground, holding an inspection camera and lights, and providing adjustable anchor points for the mooring cable-ends.

The external dimensions of the frame are 1290mm x 1290mm x 1690mm. The vertical dimension includes the height of the camera and lighting bridge, which measures roughly 845mm. The mount for the camera system is adjustable, as are the location of the anchor points of the mooring cable-ends.

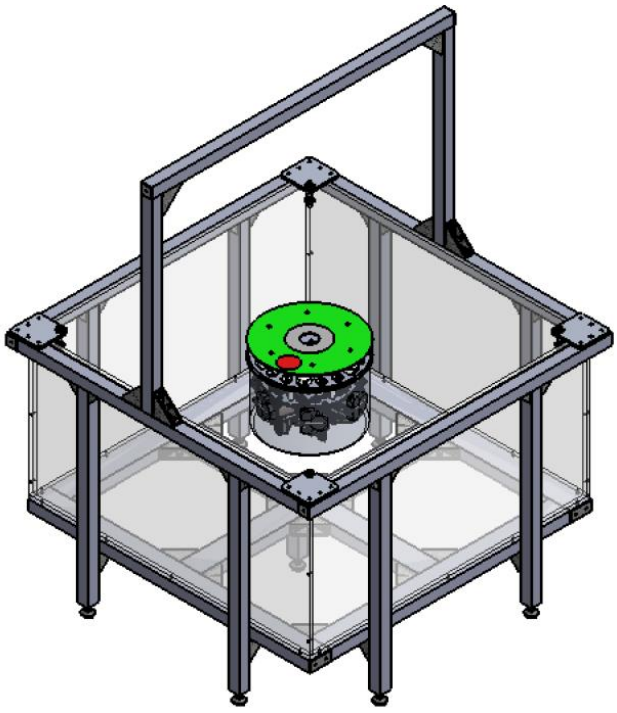

Figure 5.1: Small basin for experimental study.

5.2.1.2 Platform

A splash proof cylindrical platform, (shown in Figure 5.2), was constructed to house six mooring cable actuators, along with the necessary electronics to drive the actuators (motors). Moreover, the platform houses six tension sensors, two tilt sensors and an IMU. Six mooring cables exit the platform through specialized ports that could be relocated on the platform top plate. The top-most plate of the platform is a vision plate with engineered landmarks essential for the vision localization system. Two forced air vents are also installed on the platform to allow proper thermal conditions within the platform. An umbilical cord connects the center of the platform to the bridge of the platform through which all the electronic power and signals are conveyed between the platform and the

driving electronic devices. The platform's external dimensions (including the vision plate) are 361mm in diameter and 309mm in height.

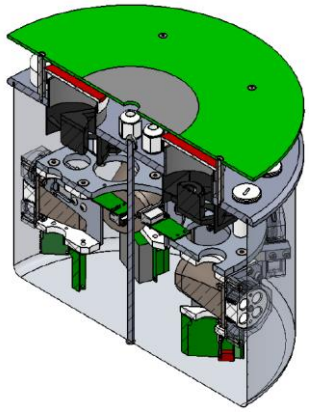

Figure 5.2: Cylindrical platform houses the drive system and electronics

The platform is driven by stepper motors and stepper motor drives (shown in Figures 5.3 and 5.4).

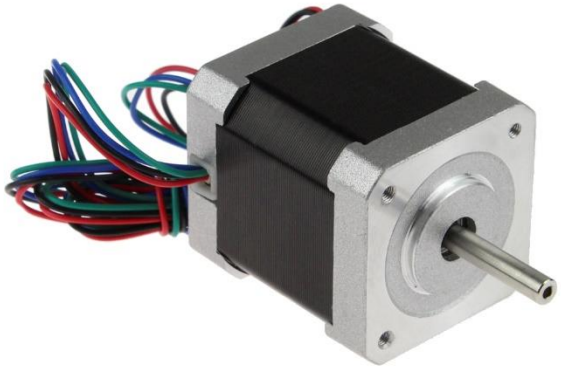

Figure 5.3: Stepper motors used in the system

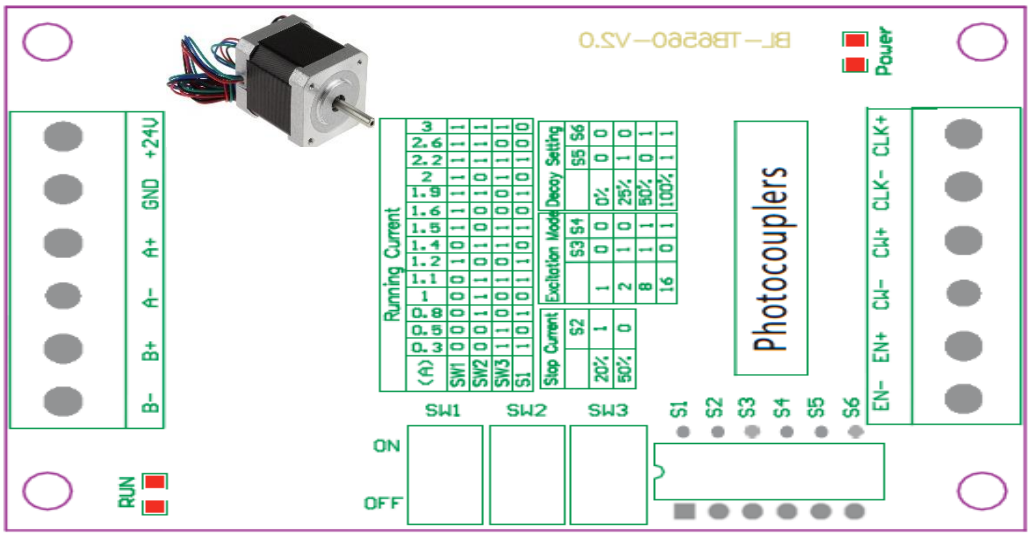

Figure 5.4: Stepper motor drive

5.2.1.3 System Brain

The brain of the system is housed in an NI PXIe-1071 4-slot 3U Express Chassis (shown in Figure 5.5), which is a compact 4-slot chassis featuring a 4-slot wide system controller slot, which can accept either an embedded controller or a remote controller.

Figure 5.5: The brain of the system and 2.5 GHz Dual Core Embedded Controller.

5.2.1.4 Sensors

The MTI-G (shown in Figure 5.6) by XSENS is a miniature Inertial Navigation System (INS) with integrated 3D magnetometers (3D compass), with an embedded processor capable of calculating roll, pitch and yaw in real time, as well as outputting calibrated 3D linear acceleration, rate of turn (gyro) and (earth) magnetic field data.

Figure 5.6: The XSENS MTI-G Inertial Navigation System

The camera is a dome-shaped CCTV type camera made by Vision (shown in Figure 5.7). In order to observe the entire scene, a wide-angle lens is used which features a focal length of 2.1mm. The maximum angle of view of the camera is 150 degrees. The image sensor is a 1/3" Sony CCD. The minimum illumination is 0.001Lux/F2.0, and the video output resolution is composite 1.0 Vp-p.

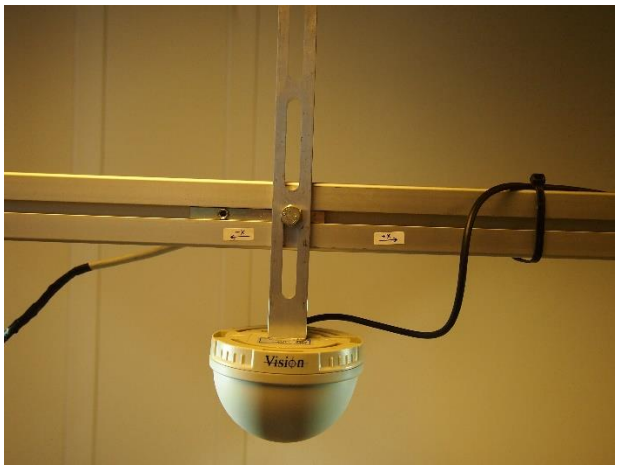

Figure 5.7: CCTV dome camera with wide-angle lens (2.1 mm)

The T7 (as shown in Figure 5.8) by US Digital is a solid-state absolute inclinometer that senses tilt angles over a full 360^0 range in a single axis. The T7 incorporates a number of technological advances to create a new type of inclinometer that is rugged, compact, fast, flexible and easy to use. The T7 is available in several interface and protocol options. The physical interface selected is RS232, with solid-state technology - no moving parts; it is

field programmable with full 360^0 range, and its temperature compensated from 0 ^oC to 70 ^oC with $\pm 0.1^oC$ accuracy, and 0.01^oC resolution.

Figure 5.8: T7 inclinometer by US Digital

The tension sensors (shown in Figure 5.9) consist of a full bridge load cell interfaced to the HX711, a precision 24-bit analog-to-digital converter (ADC) designed for weigh scales and industrial control applications.

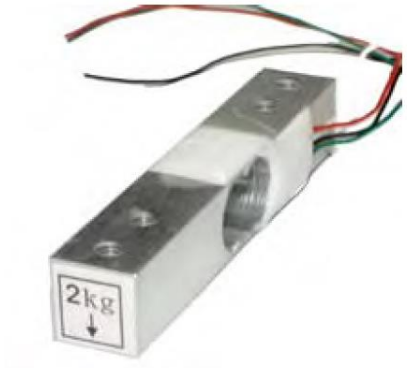

Figure 5.9: Load cell.

5.2.1.5 Electrical Panel Board

This section describes the electrical panel and the connections between the panels and the platform. Figure 5.10 is a photo picture of the electrical panel board housing the motion

interface boards to the left, the data acquisition interface board in the middle, the PXI controller (brain) to the right, power supplies and electrical fuses and breakers on the top right and interface board to the platform on the bottom left. The electrical panel board (EPB) main power arrives through a breaker that will cut power on all devices when tripped. The power to the entire system (except the PXI) can be turned off using the emergency button. Finally, the power to the motors can be activated or deactivated using the key switch. The internal connections in the EPB are permanent and there is no need to disconnect these when moving the system. The external connection to the platform is done at a single location (bottom left corner).

Figure 5.10: Electric panel

5.2.1.6 The Software

A code was developed using LabView 2013. A project called FCDP was built and it contains all the required sub-VIs needed to operate the system. The architecture of the delivered software is described in this section.

The Main tab on the front panel (shown in Figure 5.11) is used to operate and monitor the system. Each section of the Main tab is responsible for the different tasks described below.

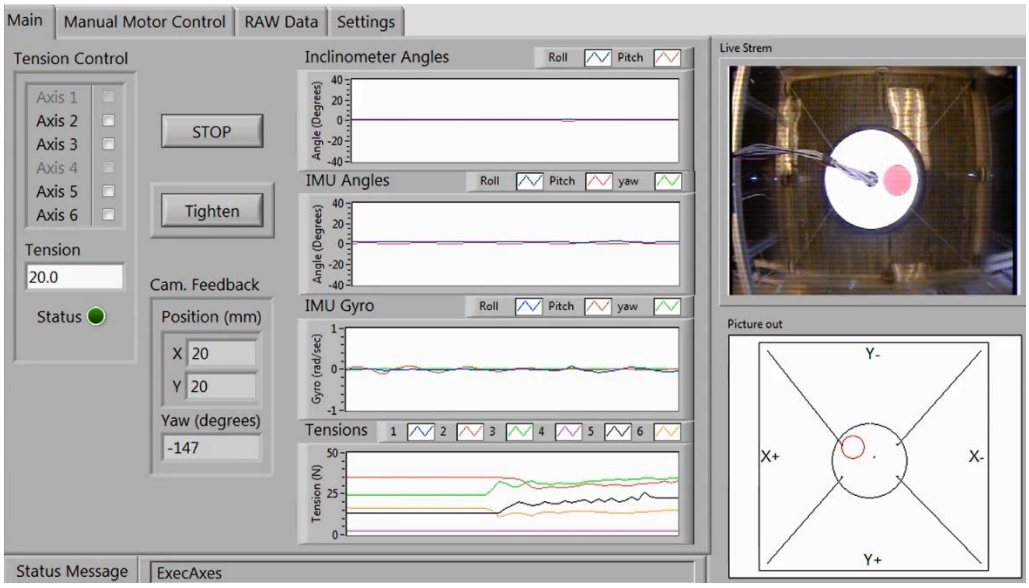

Figure 5.11: 'Main' tab.

Tension Control: this section controls which motor should be operating in tension control, the value of the tension that needs to be maintained throughout tension control, and an indicator that turns ON if the tension control is active.

The user should select which motor needs to be operated under tension control by clicking the checkbox near the desired motor. A disabled motor can be enabled from the Settings tab. The status indicator turns ON as soon as the user selects a motor from the check box list described earlier. Tension control is automatically disabled if the user switches tabs to prevent un-operated tension control.

- Tighten button: the Tighten button is used to add tension to all the cables in the system in a sequential manner. The timeout for tightening can be setup from the Settings tab.
- STOP button: is used to stop the operation of the software.

- Position Control: The user enters the desired absolute position in this control. The desired position is measured with respect to the center of the water basin.
- GO button: the GO button will execute the desired position movement from the platform's current position to the position entered in the Position Control.
- HOME button: the Home button executes a movement command from the platform's current position to the home position (0, 0), which is located at the center of the water basin.
- Cam. Feedback: the Cam. Feedback indicator displays the platform's current position (mm) and Yaw orientation (degrees) based on digital image processing from the camera feedback.
- IMU Angles: the IMU Angles chart displays the IMU readings of the Roll, Pitch, and Yaw of the platform.
- IMU Gyro: the IMU Gyro chart displays the IMU readings of the Gyro (rad/sec) of the 3 axes.
- Tensions: the Tensions chart displays the tension sensor readings of the 6 cable-driven systems.
- Live Stream: the Live Stream video indicator displays a live video stream of the floating platform.
- Picture out: the Picture out image displays the constructed tracked platform position and orientation. The positive and negative axes directions are also shown on this indicator.

The source code of the experiment was specified. This code is written on the block diagram of the Main.vi and is shown in Figure 5.12.

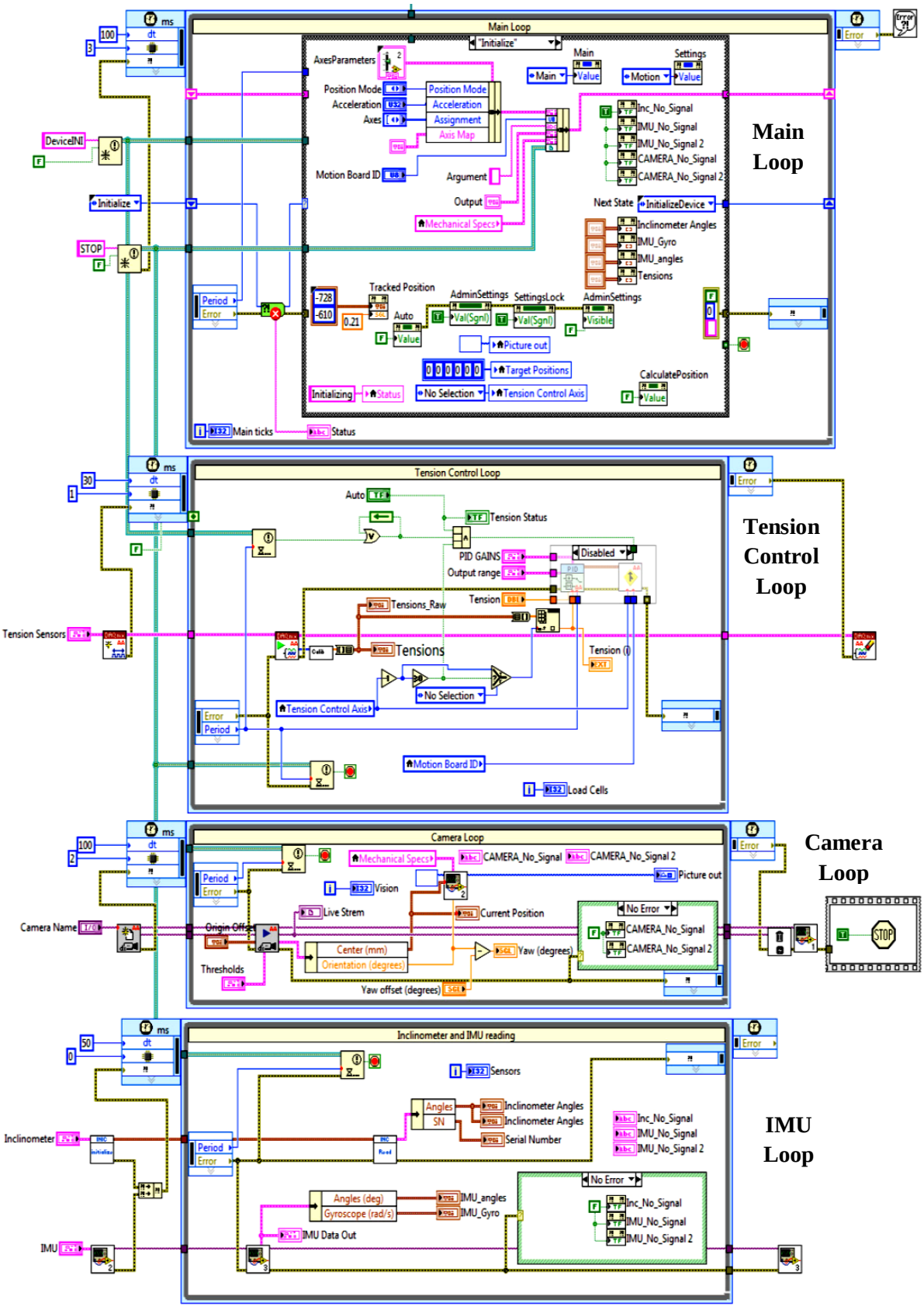

Figure 5.12: The block diagram of the MainVI.

The block diagram is divided in to 4 timed loops, each running on a processor thread as seen in Figure 5.12:

- Main loop: is the master loop in the software. It is built on a state machine architecture and is responsible for the following actions:
    - Capturing user activity and acting accordingly
    - Executing motion control of the platform
    - Controlling the execution of the slave loops
- Tension control loop: is a slave loop responsible for the following actions:
    - Acquiring and calibrating the tension signals
    - PID control of the tension control
- Camera loop: is a slave loop responsible for the following actions:
    - Acquiring and displaying video stream
    - Digital image processing of the acquired stream
    - Determining the location and orientation of the platform
- IMU reading loop: is a slave loop responsible for the following actions:
    - Acquiring and displaying the IMU angles and gyro signals

5.2.2 Experimental Study Configuration

The mooring cable configuration were used to conduct the experimental study is shown in Figures 5.13 and 5.14; it had four mooring cable to control three DOF which are the surge, sway, and yaw DOF. A static offset test was carried out to determine the mooring system's stiffness and tensions. Load cells were used to measure the mooring cable tensions. The model was pulled horizontally from its side. Accordingly, the horizontal movements and

the readings from the load cells were recorded simultaneously. Using these data, the mooring cables' stiffness was configured using Equation (3.88).

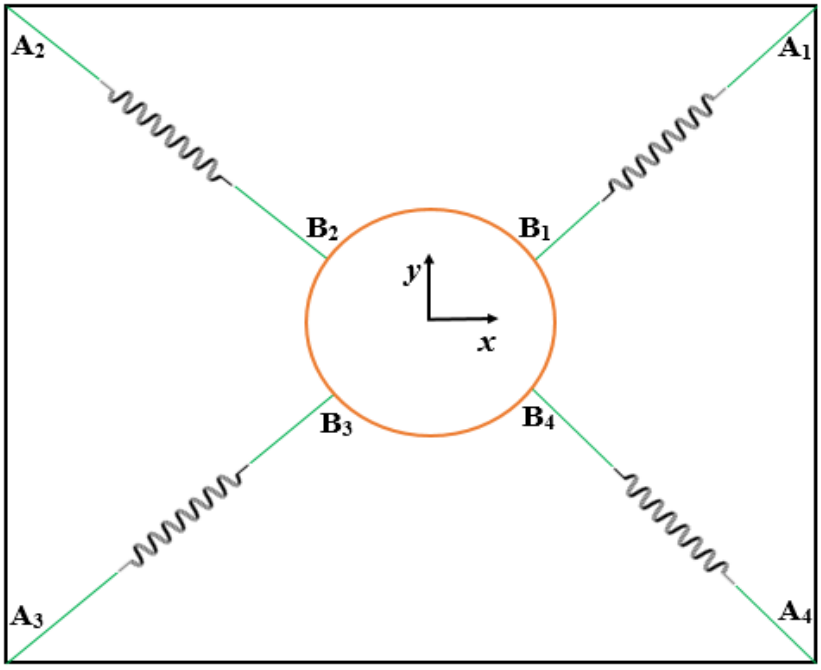

Figure 5.13: Experimental FCDP model configuration.

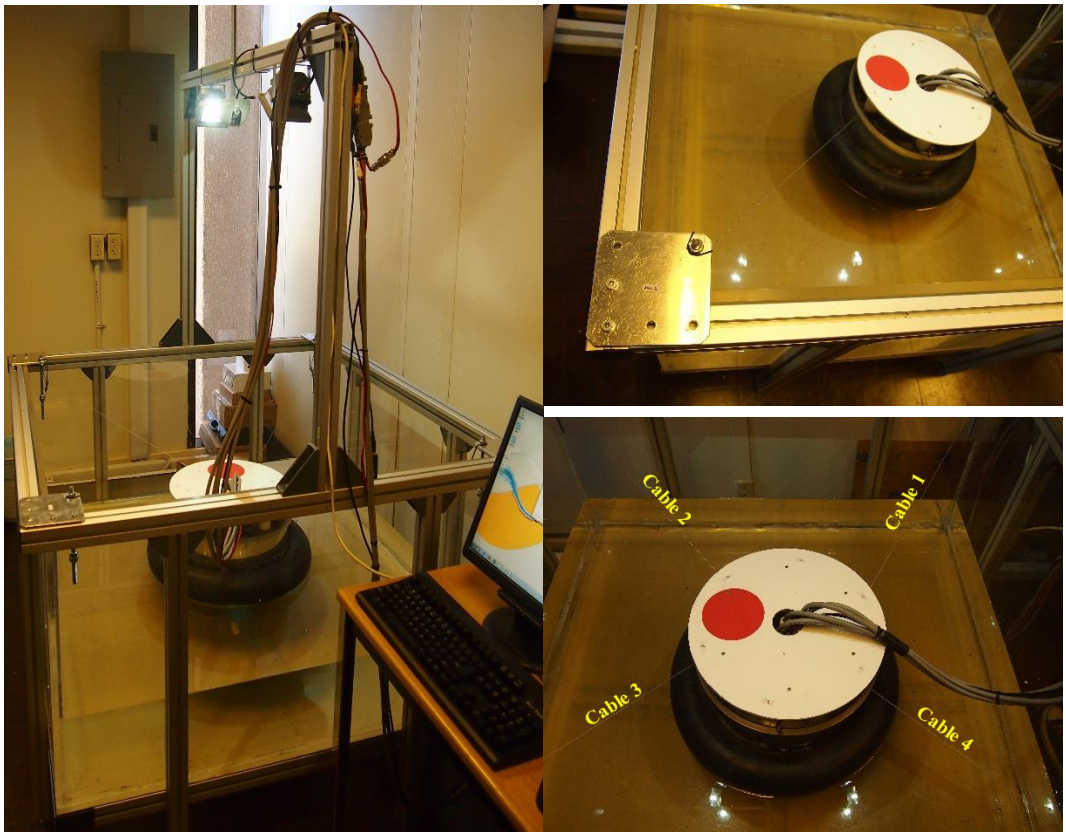

Figure 5.14: The FCDP model during test.

Table 5.1: Anchors'/Motors' position angles for FCDP.

Mooring cable Number\ Points	A_i (°)	B_i (°)
1	45	30
2	135	150
3	225	210
4	315	330

Table 5.1 represents the A, and B values respectively for the FCDP configuration as shown in Figure 5.13. While A values represent the angles between $a^{(i)}$ and the positive x-axis vectors (see Figure 3.2), B values represent the angles between $b^{(i)}$ and the positive u-axis

vectors (see Figure 3.2). The Table 5.2 represents the important parameters values of the FCDP for experimental/numerical study.

Table 5.2: FCDP platform parameters.

Designation	
Moving Radius (a)	0.15 m
Platform Weight (W)	15 Kg
Platform height (h)	0.31 m
Seabed Radius (r)	0.537 m
Water Depth (d)	0.22 m
Submerged depth (b)	0.12 m
Damping ratio for surge	0.05
Damping ratio for sway	0.05
Damping ratio for yaw	0.05
Added mass coefficient (Ca)	1

The platform moved experimentally from the center location to the location of $x = 40$ mm, and $y = 45$ mm. Accordingly, the camera was used to record the horizontal displacement of the platform with respect to time data, as shown in Figure 5.15. Due to the camera resolution, measurements can be taken, only, every 5 cm horizontal displacement increment. The load cell readings were recorded accordingly with the movement of the platform. These measurements were used as input data to run the MatLab numerical code.

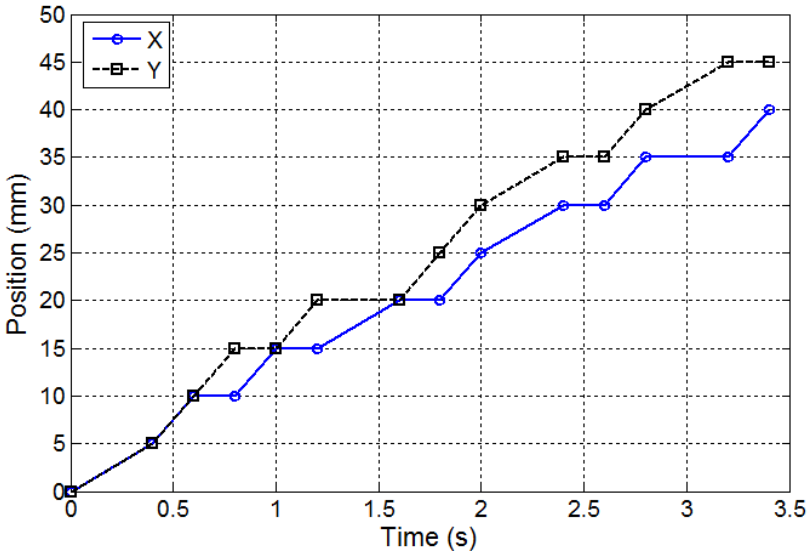

Figure 5.15: Horizontal displacement increment.

5.3 Mathematical Model

In order to compare between a numerical and an experimental result, the mathematical model, which mentioned in chapter three, are diminished to be a 3 degree-of-freedom (surge, sway, and yaw) model as follows:

$$\mathbf{M}(\mathbf{x})\,\ddot{\mathbf{x}} + \mathbf{C}(\mathbf{x})\,\dot{\mathbf{x}} + \mathbf{K}(\mathbf{x})\,\mathbf{x} = \mathbf{F}(\mathbf{x}, \mathrm{t}) \tag{5.1}$$

where

$$\mathbf{M}(\mathbf{x}) = \mathbf{M}_{\boldsymbol{s}} + \mathbf{M}_{\boldsymbol{a}} = \begin{bmatrix} m_{11} & 0 & 0 \\ 0 & m_{22} & 0 \\ 0 & 0 & I_{66} \end{bmatrix} + \begin{bmatrix} m_{11} & 0 & 0 \\ 0 & m_{22} & 0 \\ 0 & 0 & 0 \end{bmatrix}$$

$$\mathbf{C}(\mathbf{x}) = \begin{bmatrix} C_{11} & 0 & 0 \\ 0 & C_{22} & 0 \\ 0 & 0 & C_{66} \end{bmatrix}$$

$$\mathbf{K}(\mathbf{x}) = \mathbf{K}_{\boldsymbol{s}} + \mathbf{K}_{\boldsymbol{\tau}} = \sum_{i=1}^{n} k^{(i)} \begin{bmatrix} k_{11}^{s} & k_{12}^{s} & k_{16}^{s} \\ k_{21}^{s} & k_{22}^{s} & k_{26}^{s} \\ k_{61}^{s} & k_{62}^{s} & k_{66}^{s} \end{bmatrix} + \sum_{i=1}^{n} \frac{\tau^{(i)}}{l^{(i)}} \begin{bmatrix} k_{11}^{\tau} & k_{12}^{\tau} & k_{16}^{\tau} \\ k_{21}^{\tau} & k_{22}^{\tau} & k_{26}^{\tau} \\ k_{61}^{\tau} & k_{62}^{\tau} & k_{66}^{\tau} \end{bmatrix}$$

$$\mathbf{F}(\mathbf{x}, \mathrm{t}) = [0 \quad 0 \quad \bar{f} \quad 0 \quad 0 \quad 0]^{T}$$

$\bar{f}$ is the vertical force applied downward on the mobile platform by the mooring cable pre-tensions

5.4 Results and Discussion

In order to compare between a numerical and an experimental result, mooring cable stiffness was found from the static offset test, then it was used as an input for the numerical model. The stiffness of mooring cable 1, 2, 3, and 4 is equal to 8.94, 3.4, 3.74, and 1.75 N/m respectively. Before the experiment start, the mooring cables were tightened and the pre-tension of the mooring cable 1, 2, 3, and 4 was equal 22.87, 13, 7.83, and 9.75 N/m respectively and these values are used in the numerical analysis.

As can be seen from the Figures 5.16 to 5.19, the mooring cables' tension motions were fairly well predicted by the numerical model. The trend of the tensions is in a good agreement with the measured values. While the tension results of mooring cable 1 and 2 are in a good agreement, the numerical tension results of mooring cable 3 and 4 followed the same experimental results trend, but it gave relatively higher/lower tensions values at some points. For the four cables, the coefficients of variation of the root mean squared error CVs (RMSE) between the numerical and experimental cable tensions data are 0.214, 0.0023, 0.0214, and 0.0043, respectively.

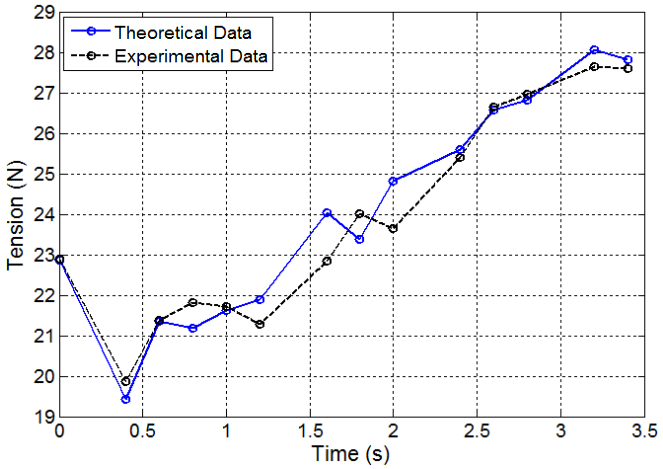

Figure 5.16: Mooring cable 1 tension.

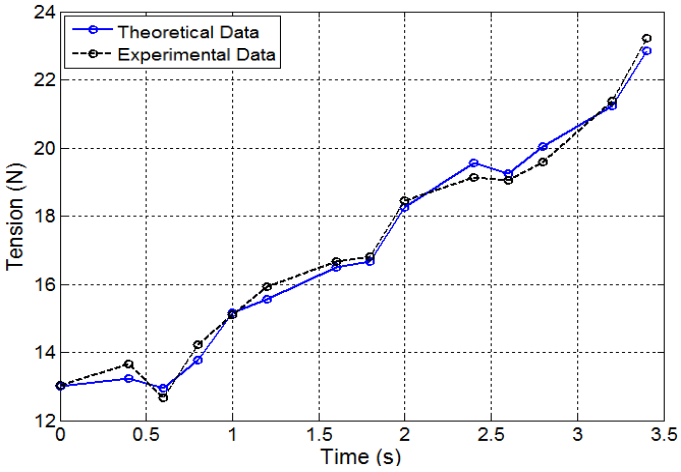

Figure 5.17: Mooring cable 2 tension.

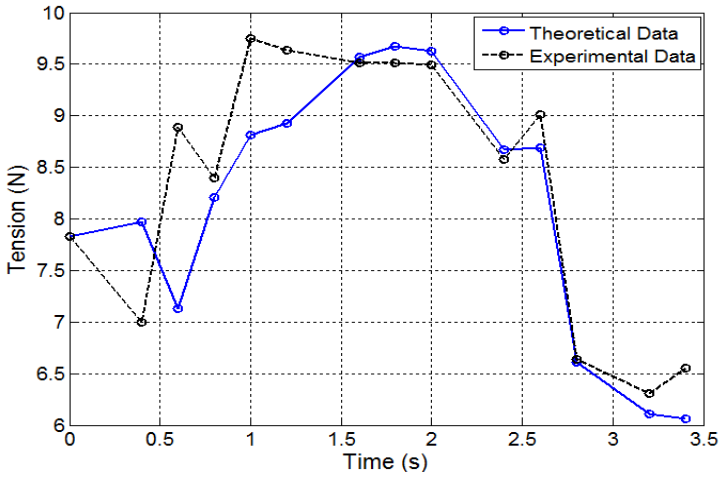

Figure 5.18: Mooring cable 3 tension.

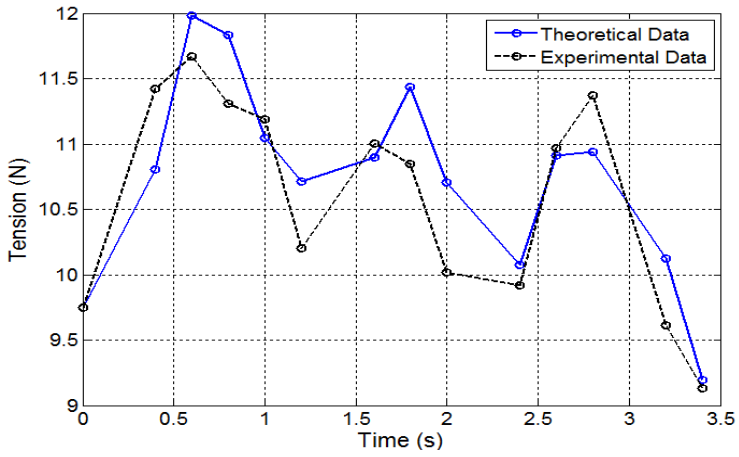

Figure 5.19: Mooring cable 4 tension.

The platform moves from the center position to the location of $x = 45$ and $y = 50$ as shown in Figure 5.15. The mooring cables' lengths were recorded accordingly with the movement of the platform. These measurements were used as input data to run the MatLab numerical code. The physical measurements and the numerical results for the mooring cables' lengths are shown in Figures 5.20 to 5.23. The numerical results followed the same trend as with the experimental results, but it gave slightly higher length values. For the four cables, the coefficients of variation of the root mean squared error CVs (RMSE) between

the numerical and experimental cable lengths data are 0.0135, 0.0118, 0.0178, and 0.0202, respectively.

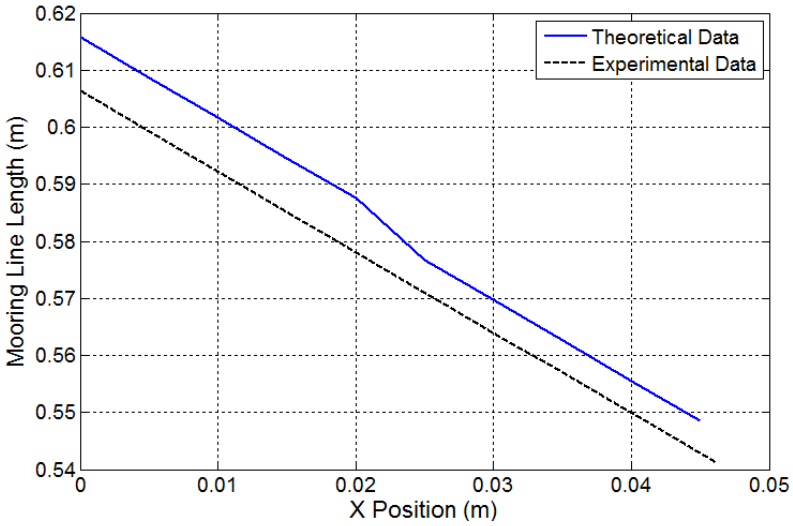

Figure 5.20: Experimental and theoretical length of mooring cable 1.

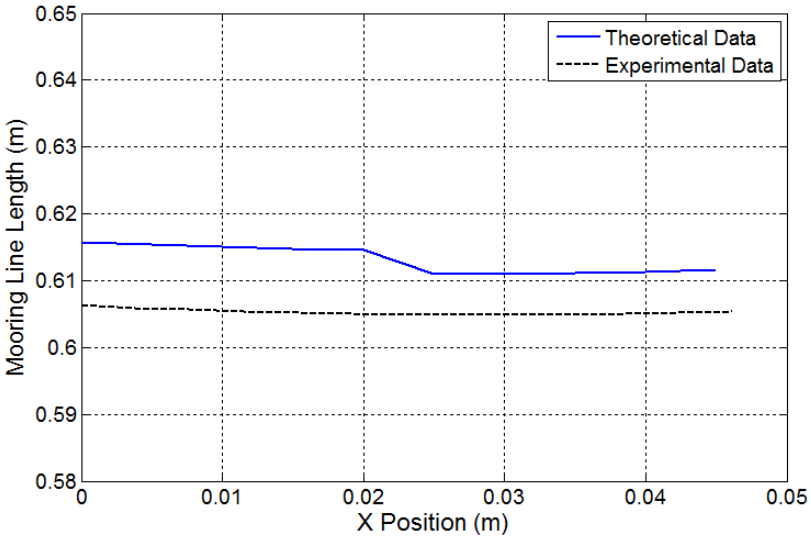

Figure 5.21: Experimental and theoretical length of mooring cable 2.

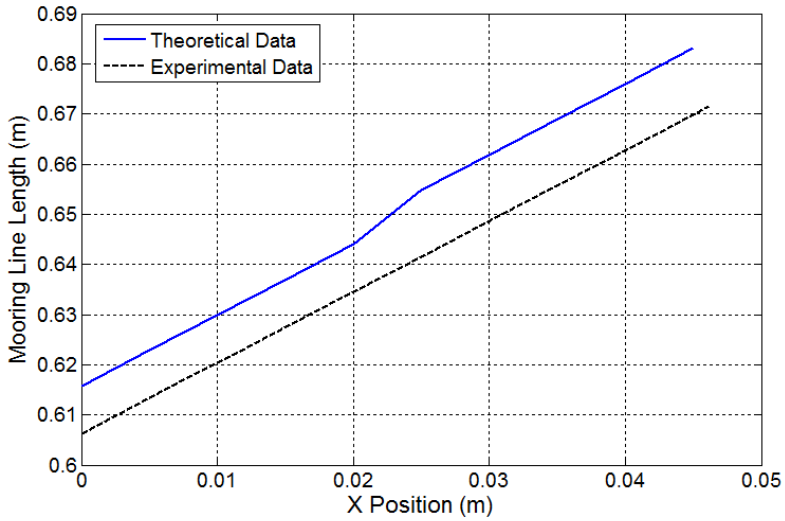

Figure 5.22: Experimental and theoretical length of mooring cable 3.

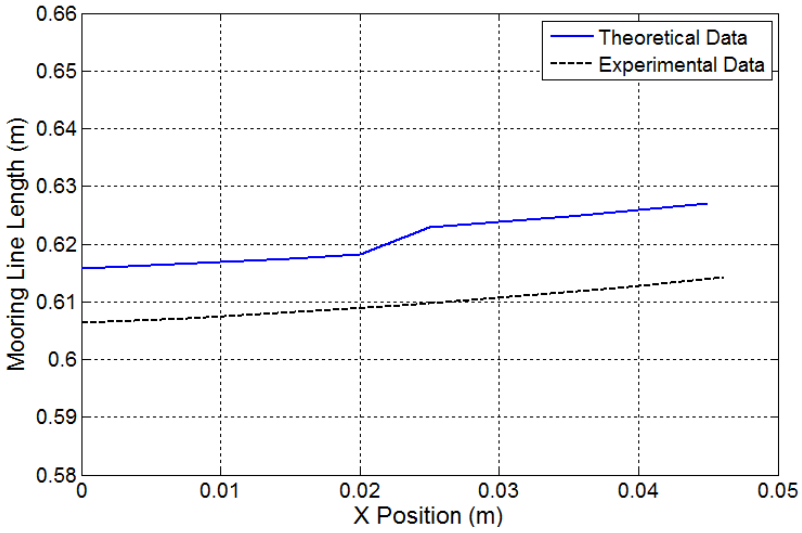

Figure 5.23: Experimental and theoretical length of mooring cable 4.

5.5 Chapter Summary

In conclusion, the numerical results were compared with the corresponding experimental measurements and the comparison showed strong trend agreement. The experimental measurements and the theoretical results of the mooring cable tensions were in good agreement for the four mooring cables. On the other hand, the experimental measurements

and the theoretical results of the mooring cable lengths had the same trend in the four mooring cables. This comparison verified the mathematical model and numerical code for FCDP.

CHAPTER 6
Analysis of a Movable Spar Platform

6.1 Introduction

A numerical analysis was conducted for predicting a movable spar platform (MSP) motion. This analysis is based on the universal marine mathematical model indicated in Chapter 3. In Section 6.2, the MSP mooring cables' configuration is considered based on the common configuration that used in the literature, then a modification, inspired using the Stewart Gough parallel manipulator configuration. In Section 6.3, the two MSP configurations are considered for static analysis to show the added benefit of the modification to the MSP.

The cables' tensions, effective area and the degree of rigidity of the modified MSP (robotics inspired platform) are studied in Section 6.4. A dynamical study is conducted for the robotics inspired platform in Section 6.5. Fluctuations in surge, sway, heave, roll, pitch and yaw motion responses are instigated to show the motion of the robotics inspired platform when it is exposed to environmental loads.

In Section 6.6, the robotics inspired platform effective area is studied. Moreover, the minimum submerged depths required at each location in the effective area of the MSP are determined. Also, the total mooring cables' tensions, displacement motion and degree of rigidity of robotics inspired platform are studied over its effective area.

Finally, a failure analysis is conducted, in Section 6.7, on the mooring system to show the effect of mooring cable failure on the MSP dynamic motion.

The purposes of this chapter study are to investigate the performance of the MSP using the universal mathematical model mentioned in Chapter 3 and to provide a good understanding of where a MSP can function, to study the degree of rigidity of the MSP in every location in its effective area, and to investigate the effect of mooring cable failure on the MSP dynamic motion. The general layout of the MSP is shown in Figure **6.1**.

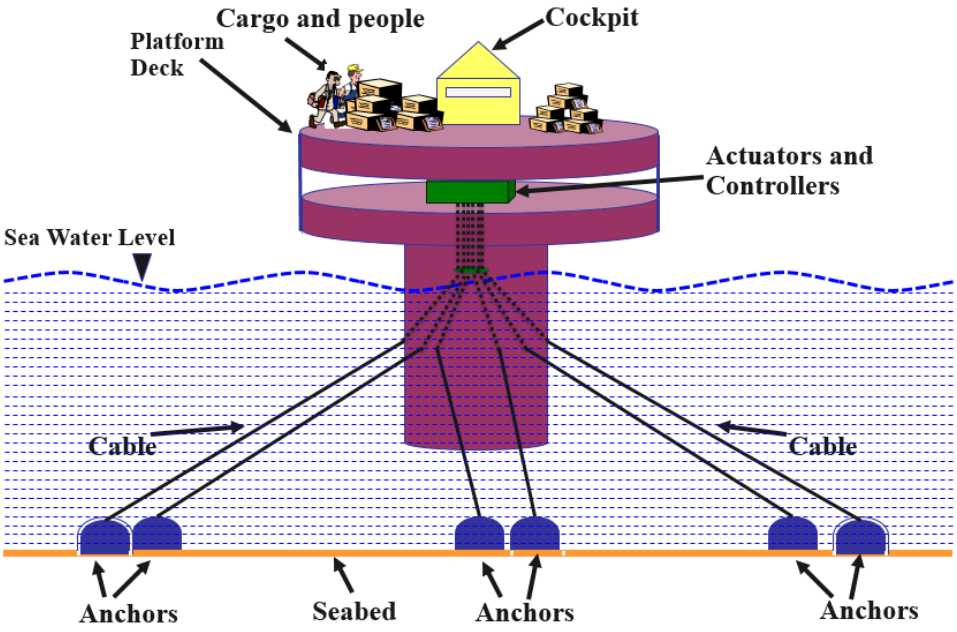

Figure 6.1: General view of MSP.

6.2 Layouts of an MSP Platform

In the literature, the classical configuration of the MSP [50, 52, 54, 93-99] is similar to one shown in Figure 6.2. A fixed frame of reference is located on an imaginary circle perimeter on seabed. The mooring cables are anchored to the seabed at different points which are located on the imaginary circle perimeter, making angles of $A_1, A_2, A_3, A_4, A_5,$ and A_6. These angles are measured from the fixed x-axis; see Table 6.1. A movable frame of reference is located on the floating structure at the center of gravity (CG). The six mooring

cables are hosted at co-located points $[B^{(1)}, B^{(4)}]$, $[B^{(2)}, B^{(5)}]$, and $[B^{(3)}, B^{(6)}]$ which are positioned on the (u,v)-plane and make angles of $0, 120, \text{and } 240,$ with the u-axis.

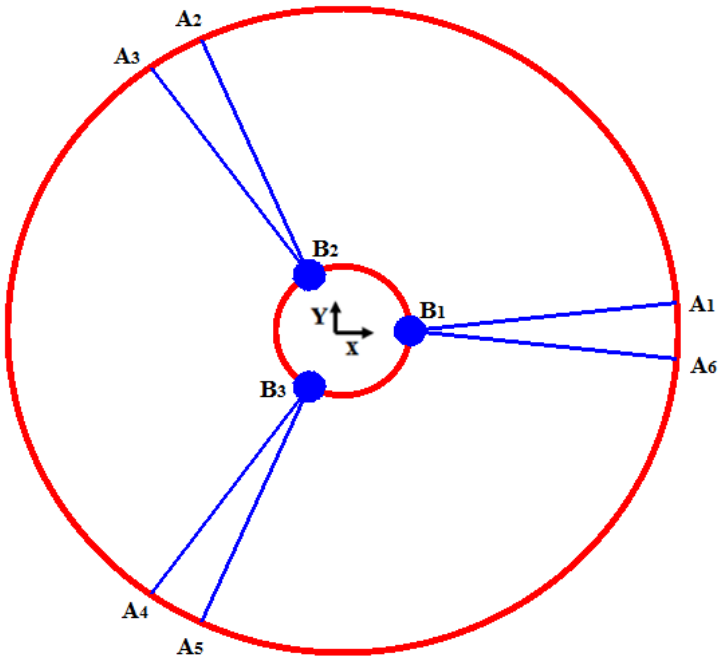

Figure 6.2: 2-D sketch of the classical spar platform configuration.

Table 6.1: Anchors' position angles of the classical spar platform configuration [99], with respect to the positive X-axis.

Mooring cable Number\ Points	A_i (°)
1	5
2	115
3	125
4	235
5	245
6	355

Figure **6.3** and Figure **6.4** showed the modified MSP layout (robotics inspired platform) which was inspired by the Stewart Gough parallel robot layout. While the anchor's position angles for a robotics inspired platform are derived from a 6-6 Stewart Gough parallel robot configuration, the motors' position angles are taken based on the common spar configuration.

The mooring system of the robotics inspired platform is made up of 12 mooring cables, divided into three groups, and each group has two mooring bundles. Every two mooring cables is assumed as one mooring bundle, and the centerlines of these mooring bundles are arranged in a form similar to that shown in Figure 6.3. The stiffness/tension of the assumed mooring bundle is equal to the summation of the stiffness/tension of two mooring cables.

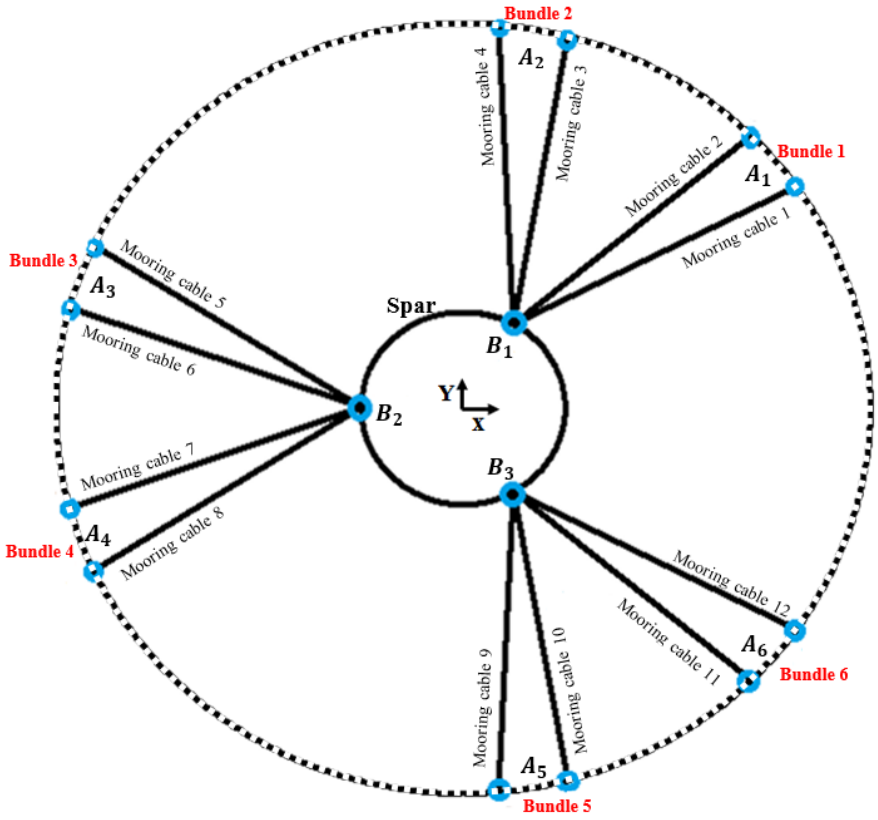

Figure 6.3: 2-D sketch for modified MSP (robotics inspired platform).

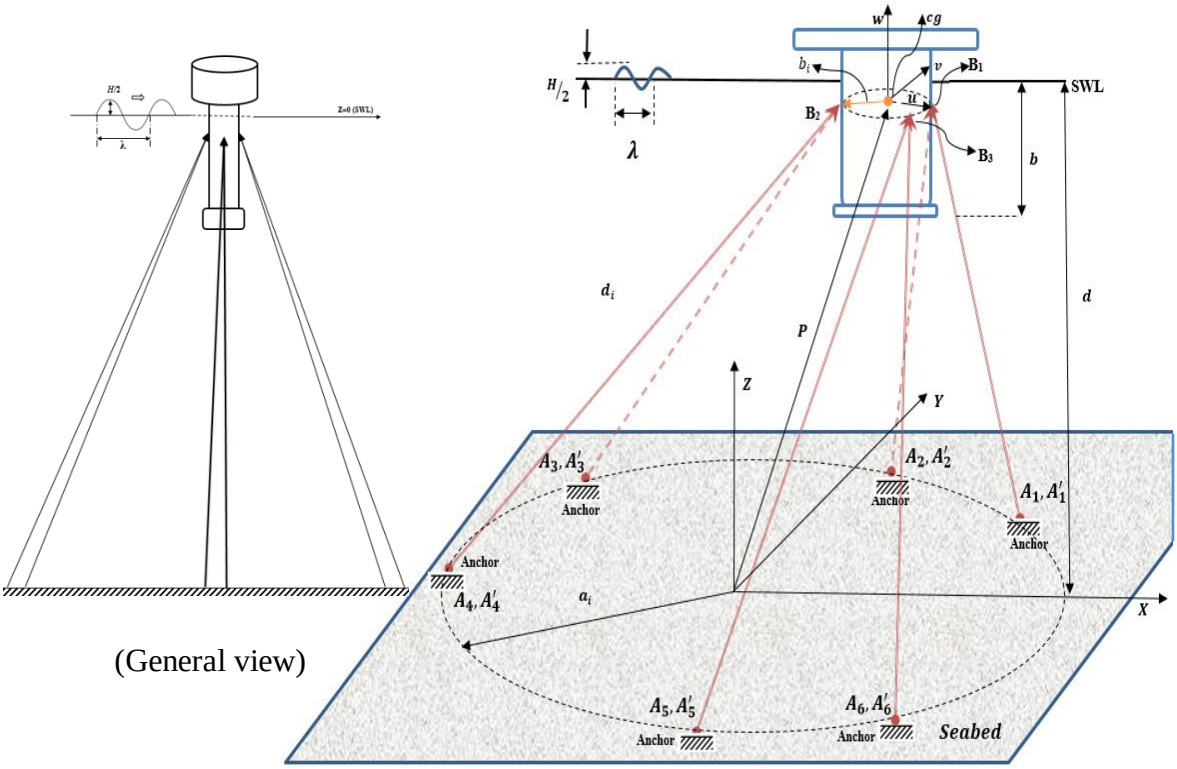

Figure 6.4: General MSP layout.

Table 6.2: Anchors'/Motors' position angles for robotics inspired platform, with respect to the positive X-axis.

Mooring bundle Number\ Points	A_i (°)	B_i (°)
1	45	0
2	75	120
3	165	240
4	195	--
5	285	--
6	315	--

Table **6.2** represents the A_i and B_i position angles respectively for the two MSP configurations to carry out the analysis. A_i values represent the angles between $a^{(i)}$ and the positive x-axis vectors. While, B_i values represent the angles between $b^{(i)}$ and the positive u-axis vectors.

Table 6.3: Simulation assumed values for MSPs.

Designation	
Platform	
Moving Radius (a)	10 m
Platform Height (h)	50 m
Platform Mass	$1.2566 * 10^7$Kg
Seabed Radius (r)	800 m
Water Depth (d)	800 m
Submerged Depth due to weight (b_w)	40 m
Stiffness (k_S)	30 KN/m
Damping ratio for surge	0.0027
Damping ratio for heave	0.0044
Damping ratio for sway	0.0026
Damping ratio for roll, pitch, and yaw	0.0005
Added mass coefficient (C_a)	1
Sea Wave	
Height (H) [54, 93, 96-98, 100]	2 m
Time Period (T_s)	5 sec

Table 6.3 represents the important parameters values of the MSP and sea waves which are used in the static and dynamic analysis.

Table 6.4: Natural frequencies for MSPs, at the center location and $b = 52$ m.

Natural Frequencies (ω_n)	Case 1 (rad/s)	Case 2 (rad/s)
1	0.0324	0.3718
2	0.1312	0.4996
3	0.5248	1.4730
4	1.6951	3.3754
5	4.4606	4.9283
6	5.8842	5.7959

Table **6.4** represents the natural frequency values of the classical spar platform (Case 1) and the robotics inspired platform (Case 2).

6.3 Static Analysis of MSPs

The classical spar platform and the robotics inspired platform configurations are studied in this section in a static environment. This study is performed to determine the most suitable MSP configuration, in a marine application.

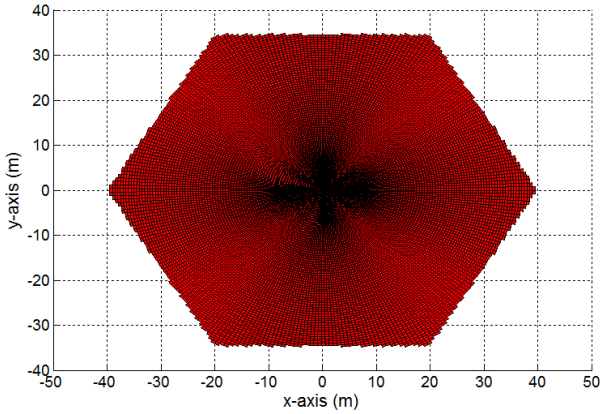

Figure 6.5: Effective area of the classical spar platform.

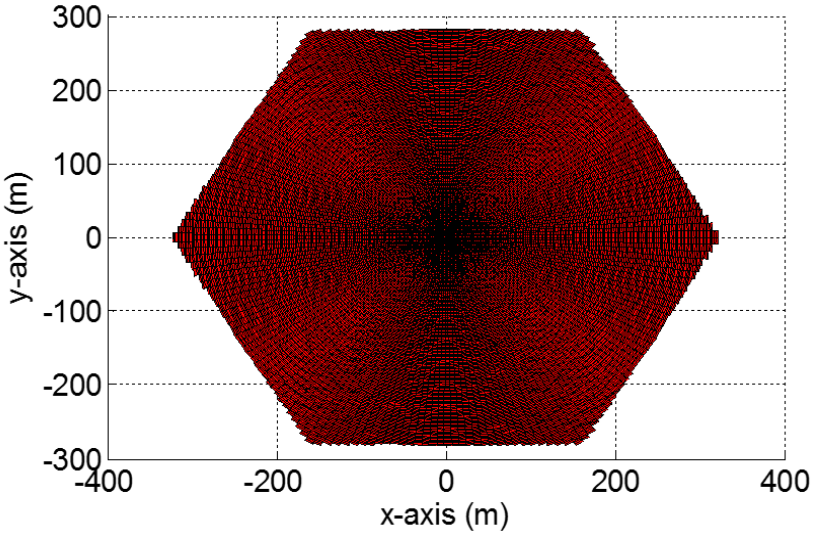

Figure 6.6: Effective area of the robotics inspired platform.

First, the effective area was checked for the two configurations of MSPs. Positive mooring cable tensions in the MSPs are required, Equation (3.83) is used to measure the mooring cables' tensions to ensure non-negative check. Figure **6.5** and Figure **6.6** represent the

effective area of classical spar platform and the robotics inspired platforms of an MSP, respectively. In conclusion, the larger effective area is acquired by the robotics inspired platform.

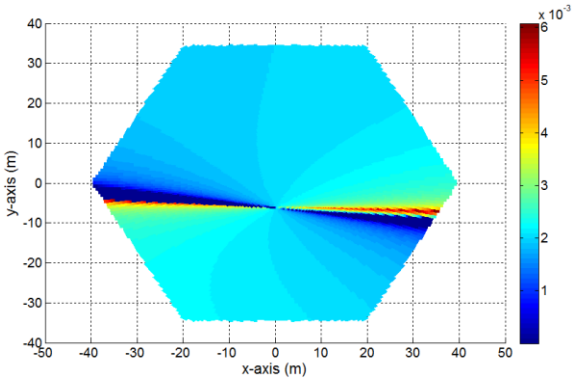

Figure 6.7: Minimum natural Frequency (colour, Hz) over the effective area of the classical spar platform.

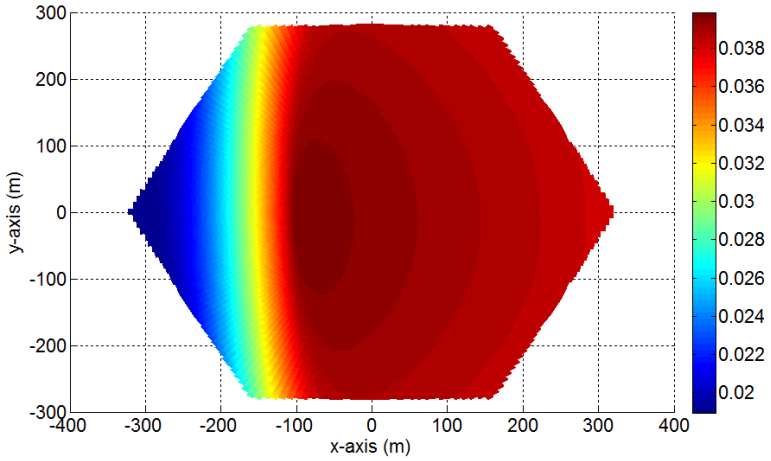

Figure 6.8: Minimum natural Frequency (colour, Hz) in the effective area of the robotics inspired platform.

The minimum natural frequency of the MSPs' configurations was found at all locations in the effective area. Equation (3.85) was used to measure the minimum natural frequency, at all locations, to detect the degree of rigidity of MSPs. Figure **6.7** and Figure **6.8** represent the minimum natural frequency over the effective areas of the classical spar and the robotics inspired platforms, respectively. As shown, the robotics inspired platform has

better degree of rigidity than the classical spar platform. This means that the robotics inspired platform is more rigid than the other.

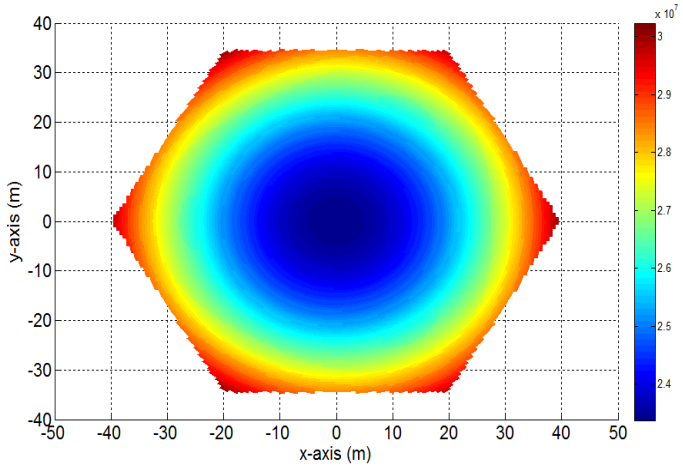

Figure 6.9: 2-norm tension values, of the six mooring cables, (colour, N) at each location in the effective area of the classical spar platform.

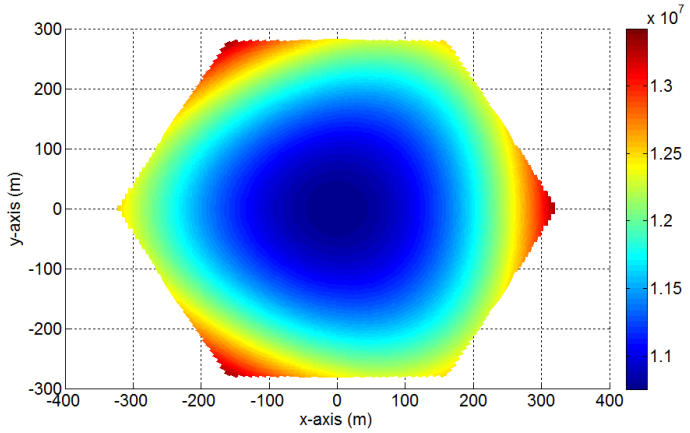

Figure 6.10: 2-norm tension values, of the six mooring cables, (colour, N) at each location in the effective area of the robotics inspired platform.

The 2-norm tension values of the mooring cables of the MSPs' configurations were calculated at all locations in the effective area. Equation (3.83) was used to measure the mooring cables' tension at all locations, then Equation (3.84) was used to find the Root Mean Square (RMS) of the mooring cables' tensions to quantify the tensions in each location.

Figure **6.9** and Figure **6.10** represent the 2-norm mooring cables' tension value over the effective areas of classical spar and robotics inspired platforms, respectively. The robotics inspired platform needs less mooring cable tension to work in the effective area without losing its degree of rigidity.

In conclusion, the modification, which is inspired by Stewart Gough parallel robot, provides the MSP a large effective area with high degree of rigidity with lower needed tension.

6.4 Dynamic Analysis of the MSP

6.4.1 Introduction

Based on the previous section, the MSPs configurations are studied in this section when it is exposed to environmental loads.

Figure **6.11** to Figure **6.13** show the time history of sea wave forces applied on the MSPs at the center location, $x = 0\ m;\ y = 0\ m$ with respect to the fixed global coordinate frame, as depicted in Figure **6.4**.

Table 6.3 data is used to perform the dynamical analysis of the MSPs. In addition, the main submerged depth b ≅ 46.9 m is used in the dynamical analysis.

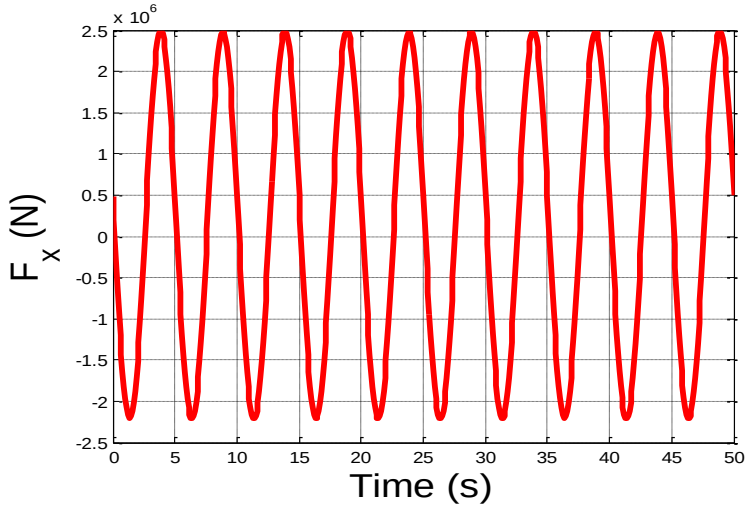

Figure 6.11: Surge excitation force on the MSP.

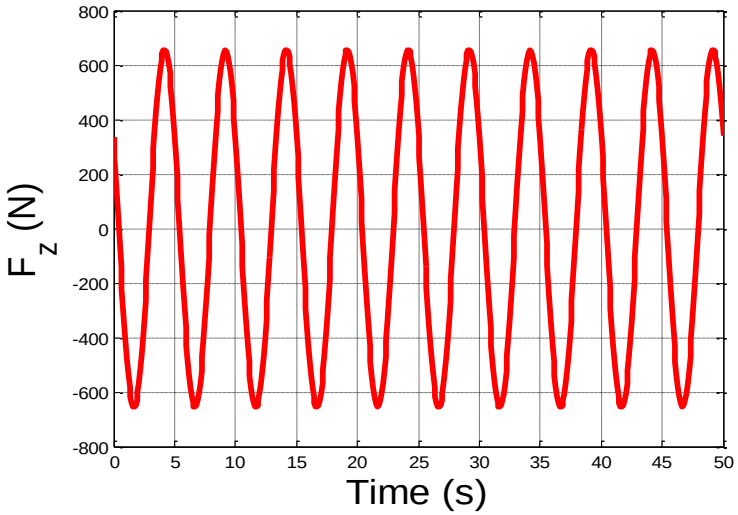

Figure 6.12: Heave excitation force on the MSP.

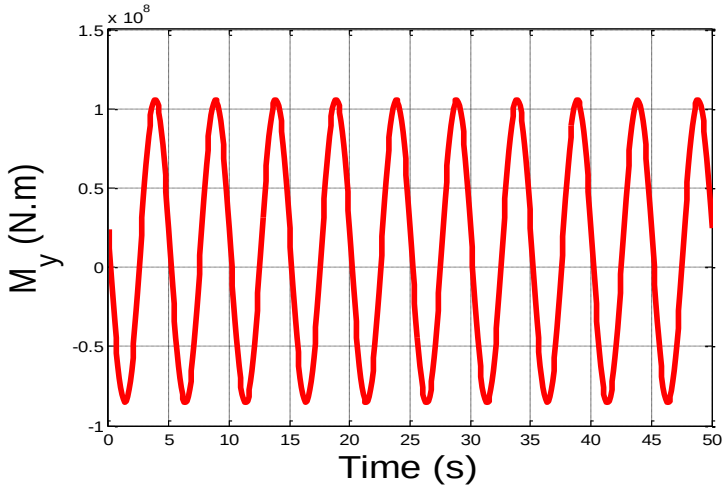

Figure 6.13: Pitch excitation force on the MSP.

Table 6.5: RMS dynamic for displacements, velocities, and accelerations for MSPs, the classical spar platform (Case 1) and the robotics inspired platform (Case 2).

SPAR Platform Cases	X (m)	Y (m)	Z (m)	ψ (rad)	θ (rad)	φ (rad)	$\dot{X}$ (m/s)	$\dot{Y}$ (m/s)	$\dot{Z}$ (m/s)
Case 1	**11.732**	**0.4012**	**7.9634**	**0.0410**	**0.4105**	**0.0146**	**0.9991**	**0.0072**	**0.7000**
Case 2	**1.0152**	**0.0016**	**0.7878**	**0.00021**	**0.0178**	**0.00001**	**0.5693**	**0.00027**	**0.4134**
SPAR Platform Cases	$\dot{\psi}$ $(\frac{rad}{s})$ $*10^{-2}$	$\dot{\theta}$ $(\frac{rad}{s})$	$\dot{\varphi}$ $(\frac{rad}{s})$ $*10^{-2}$	$\ddot{X}$ (m/s^2)	$\ddot{Y}$ (m/s^2)	$\ddot{Z}$ (m/s^2)	$\ddot{\psi}$ $(\frac{rad}{s^2})$ $*10^{-2}$	$\ddot{\theta}$ $(\frac{rad}{s^2})$	$\ddot{\varphi}$ $(\frac{rad}{s^2})$ $*10^{-2}$
Case 1	**0.0700**	**0.0350**	**0.0300**	**0.9065**	**0.0003**	**0.7057**	**0.0025**	**0.0264**	**0.0009**
Case 2	**0.0035**	**0.0164**	**0.00073**	**0.8323**	**0.00024**	**0.6143**	**0.00179**	**0.0223**	**0.0027**

Table **6.5** represents the dynamic analysis of the two configurations of the MSP at the center location and at the submerged depth b = 52 m. As shown, the robotics inspired platform has lower RMS response values than the other, which agreed with the static analysis conclusion in the previous section. Therefore, the robotics inspired platform is chosen for further study and analysis.

6.4.2 Dynamic Analysis Behavior of the Robotics Inspired Platform

To avoid mooring cable slack of the MSP, it is required to have varying mooring cable tensions in the MSP. Figure 6.14 shows the mooring cable tensions (calculated by Equation (3.83)) at the center location (x = 0 m, y = 0 m) and a submerged depth of b ≅ 46.9 m. These mooring cable tensions are the sufficient pre-tensions needed at that location to ensure that there isn't cable slack (negative tension) when the robotics inspired platform is exposed to environmental loads. These mooring cable tensions balance the sea wave forces and all static forces applied on the robotics inspired platform.

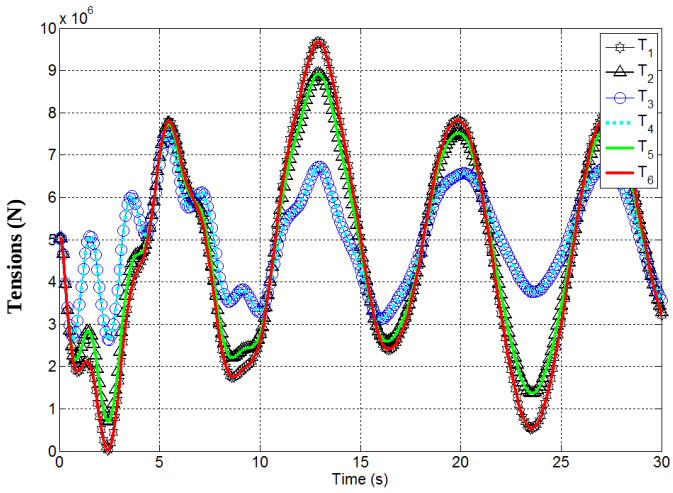

Figure 6.14: The six mooring cable tensions of a robotics inspired platform.

As a reference case, let us consider the dynamic response of a spar platform that is excited by the sea wave loads, and whose center of gravity is located at the point (x = 0, y = 0, z = 780.1 m), which indicates a submerged depth of 46.9m. The translational displacements of the platform center of gravity in the (u,v,w)-directions (surge, sway, and heave) and the rotational displacements about the (u,v,w)-axes (roll, pitch, and yaw) are shown as functions of time in Figures 6.15 and 6.16, based on time steps of 0.1 second. It is observed that the dynamic response to the impinging sea waves is characterized by noticeable heave and surge and negligible sway, while performing a dominantly pitch rotation, since the rotations in the roll and yaw are negligible. A fast Fourier transform is applied on Figures 6.15 and 6.16 data generates the spar platform natural frequencies as 0.0385, 0.0529, 0.3024, 0.1391, 0.4422, and 0.5249 Hz. Figure 6.17 shows how the platform vibrational energy is distributed among these frequencies.

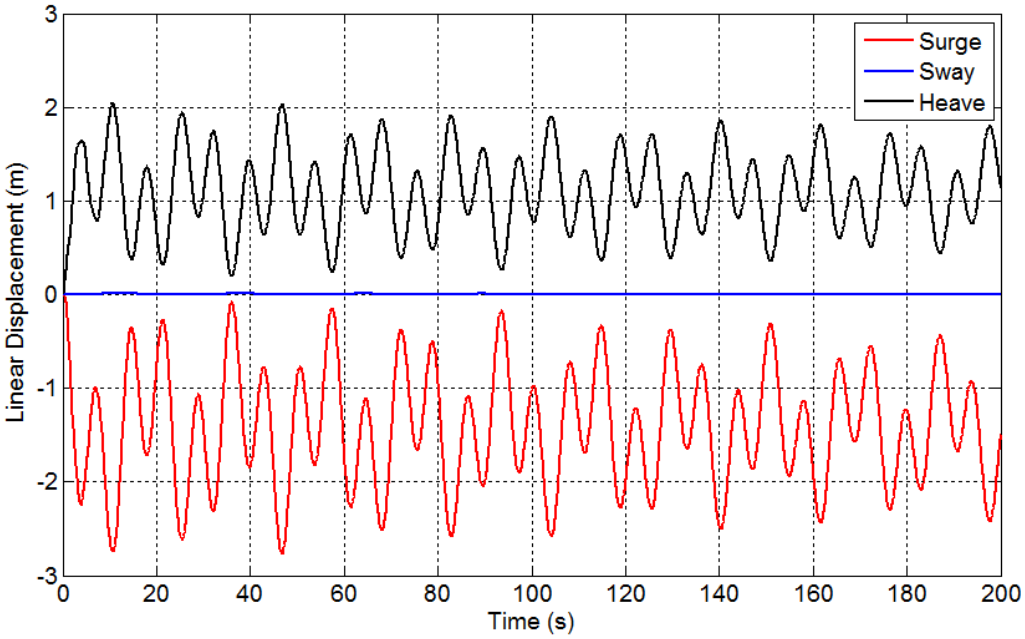

Figure 6.15: Time history of the Spar platform linear displacements.

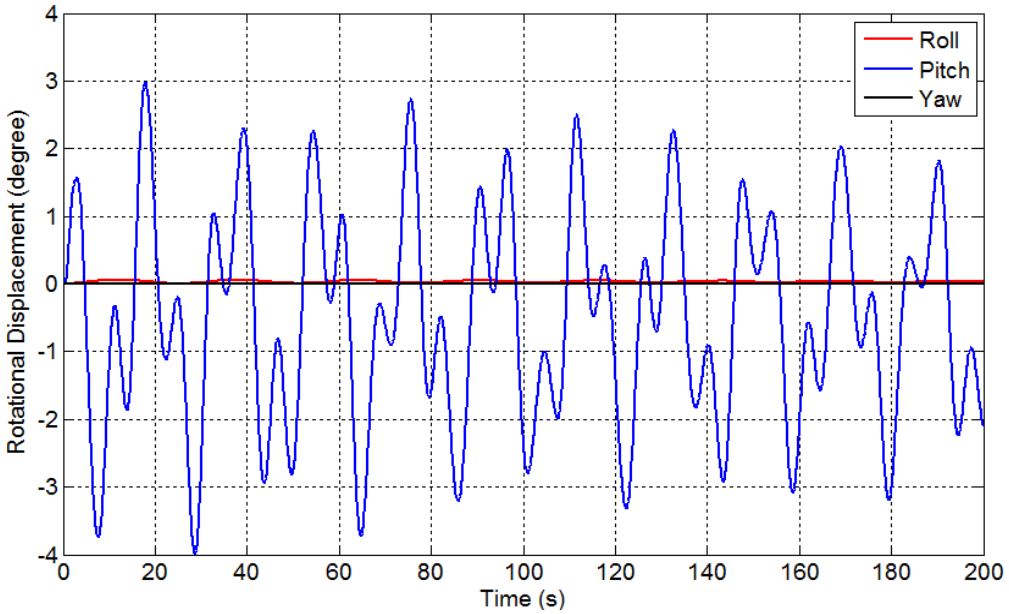

Figure 6.16: Time history of the Spar platform rotational displacements.

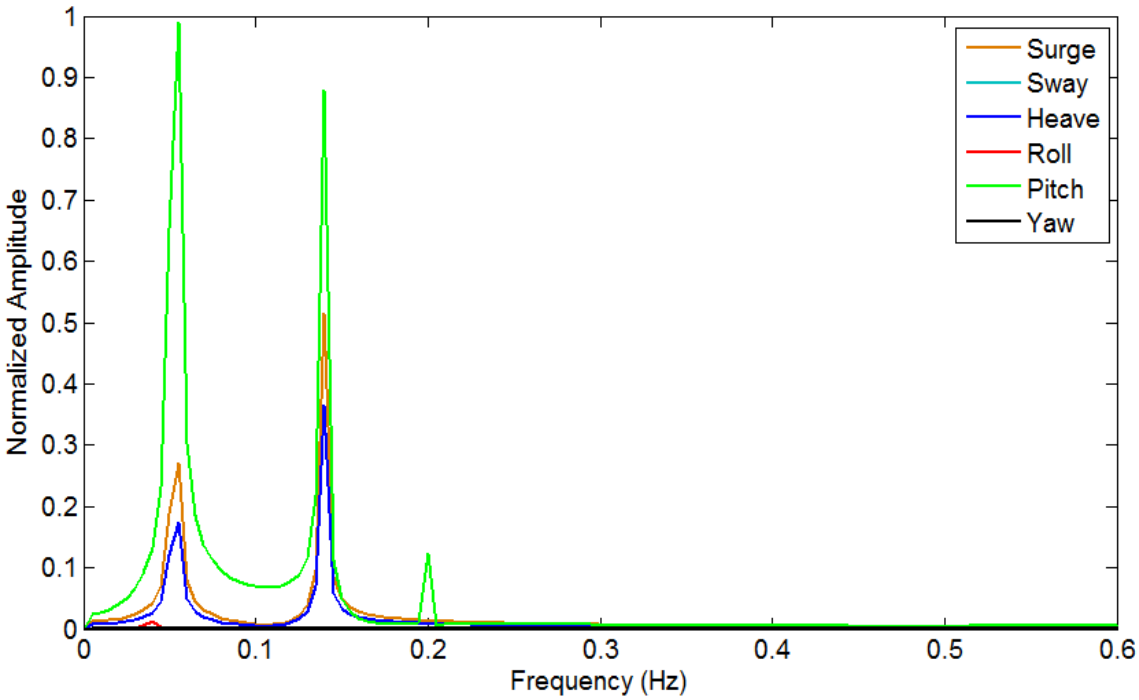

Figure 6.17: Frequency content of the spar platform vibrational motion.

6.5 Effective Area and Degree of rigidity Analysis of the Robotics Inspired Platform

The effective area of the MSP is represented by the area on the water surface that the MSP can work on without mooring cable slackness, shown in Figure 6.18. Figure 6.18 represents the metacentric height ($\overline{GM}$) within the effective area. The metacentric height is large at the darkest area in the effective area, then the platform is considered to be more stable in this area. It is shown that the metacentric height is small as the platform moves closer to the effective area edges, indicating less platform stability.

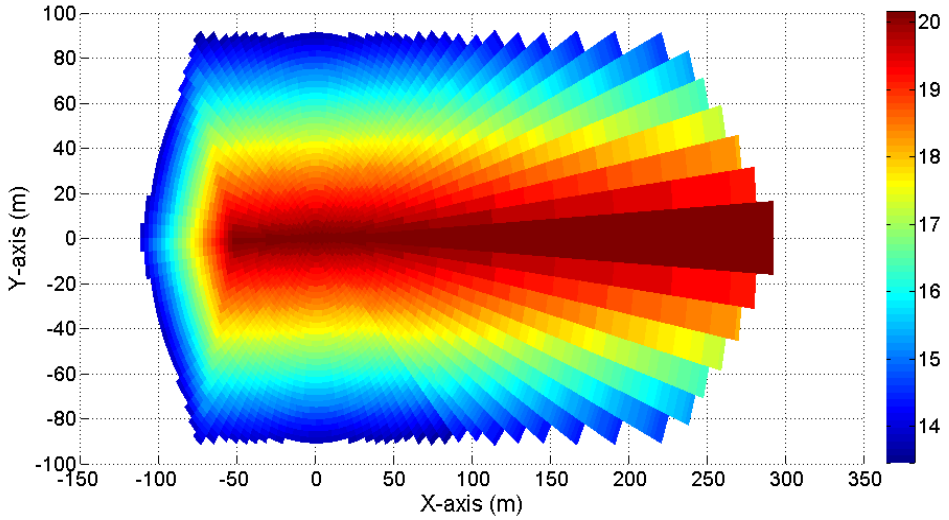

Figure 6.18: The robotics inspired platform metacenter height within its effective area (m).

The dynamic analysis is performed at each location within the effective area of the robotics inspired platform to determine the variation of the robotics inspired platform's dynamic performance in the effective area. To keep the mooring cables taut throughout the effective area, positive tensions in the mooring cables have to be maintained by applying sufficient pre-tensions. Because the necessary mooring cable pre-tensions are dependent on the location of the platform in the effective area, the resulting submerged depth of the platform will be variable. Figure **6.19** shows the variation of the minimum submerged depth across the effective area and shows that the minimum submerged depth increases as the robotics inspired platform moves closer to the effective area edges, due to the change in the mooring cable angles' directions.

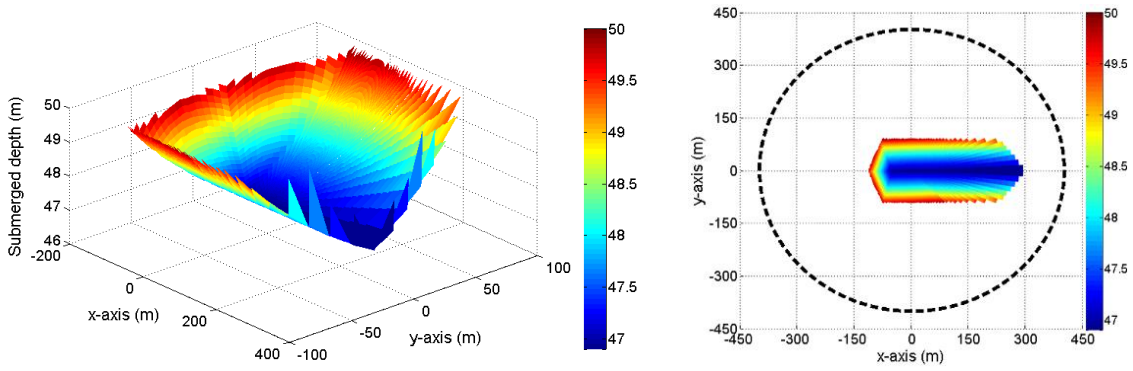

Figure 6.19: Minimum submerged depth required at each location in the robotics inspired platform effective area.

The dynamic analysis conducted at discrete locations in the effective area taking into account the variation of the submerged depth and mooring cables tensions across the effective area. Since the mooring cables' tensions and platform displacements vary with time, the Root Mean Square (RMS) measure is used to quantify the tensions and displacements in each location.

Figure **6.20** represented the 2-norm of the RMS values of the mooring bundles tensions at each location in the effective area. It is obvious that higher mooring cable tensions are needed to avoid mooring cable slack as the floating structure moves closer to the effective area edges. More cable tension is needed when the floating structure is at the negative X-direction of the effective area which is due to the asymmetry in the mooring cable configuration.

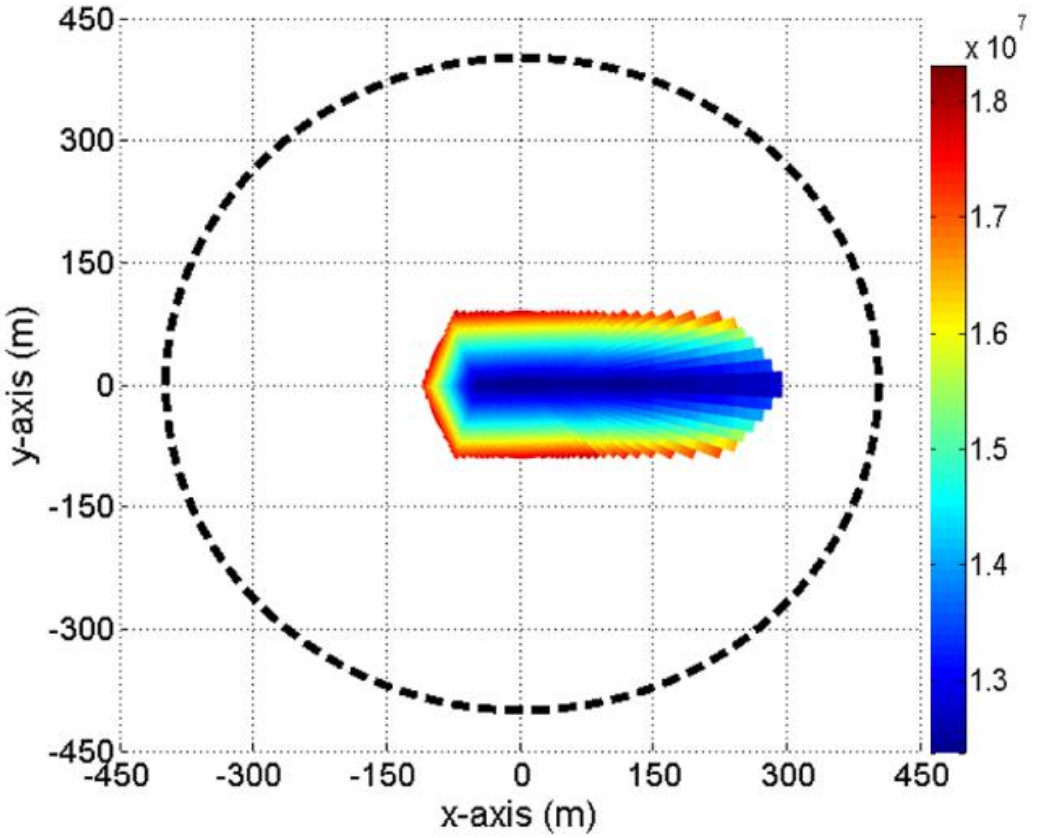

Figure 6.20: Mooring cable tensions at each location in the effective area.

Figure **6.21** shows the minimum natural frequency of the robotics inspired platform at each location in the effective area. It is shown that the minimum natural frequency and the stiffness is higher around the center of the effective area of the robotics inspired platform. The robotics inspired platform degree of rigidity is highest at the (x = -51m, y = 0m) location and it is lowest at the (x = 269m, y = $\pm$ 45.7m) locations in the platform effective area.

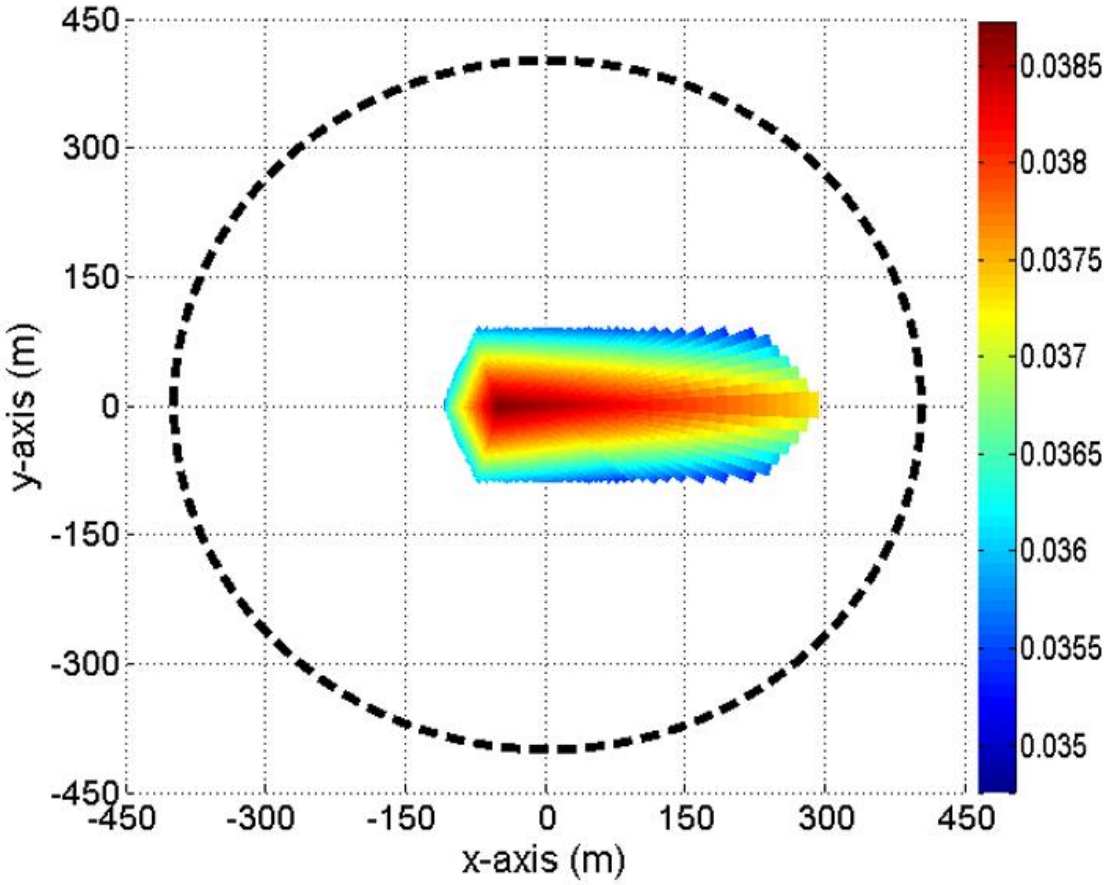

Figure 6.21: Minimum Frequency at each location in the effective area of the robotics inspired platform.

Figures 6.22 to 6.27 show the RMS values of the translational and rotational displacements at every location in the effective area, based on time steps of 0.1 second. It is noted that higher translational displacements are achieved in the surge and heave motions, compared to that in the sway motion, at the extreme negative x-central region of the spar platform effective area. In addition, higher rotational displacements are obtained in the roll and pitch motions, compared to the yaw motion, also at the extreme negative x-central region of the spar platform effective area.

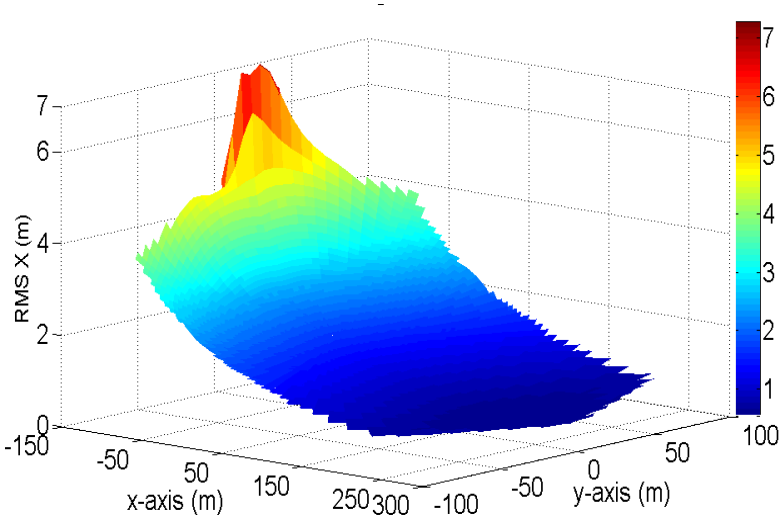

Figure 6.22: Root mean square values of robotics inspired platform surge displacement at each location in the effective area.

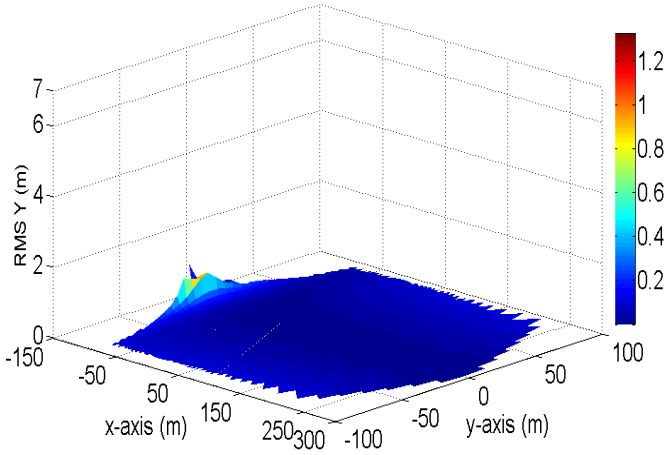

Figure 6.23: Root mean square values of robotics inspired platform sway displacement at each location in the effective area.

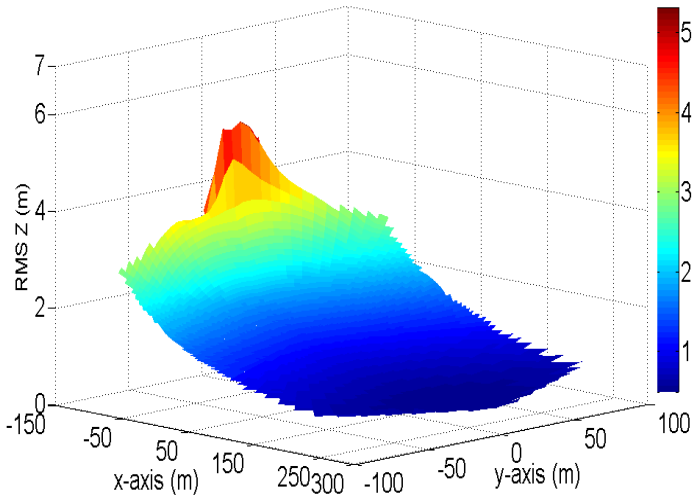

Figure 6.24: Root mean square values of robotics inspired platform heave displacement at each location in the effective area.

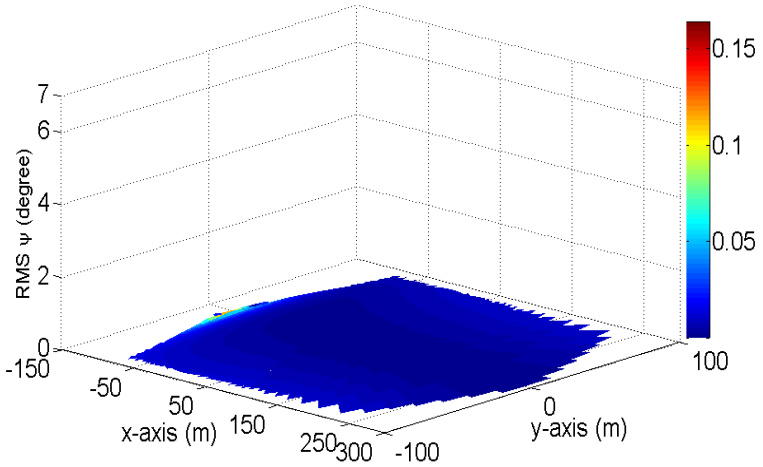

Figure 6.25: Root mean square values of robotics inspired platform roll displacement at each location in the effective area.

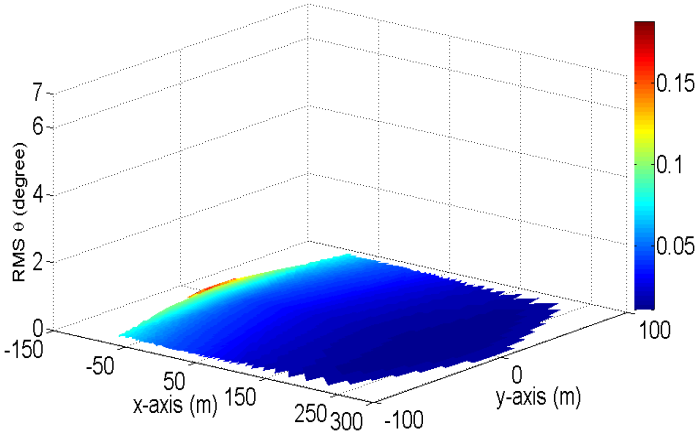

Figure 6.26: Root mean square values of robotics inspired platform pitch displacement at each location in the effective area.

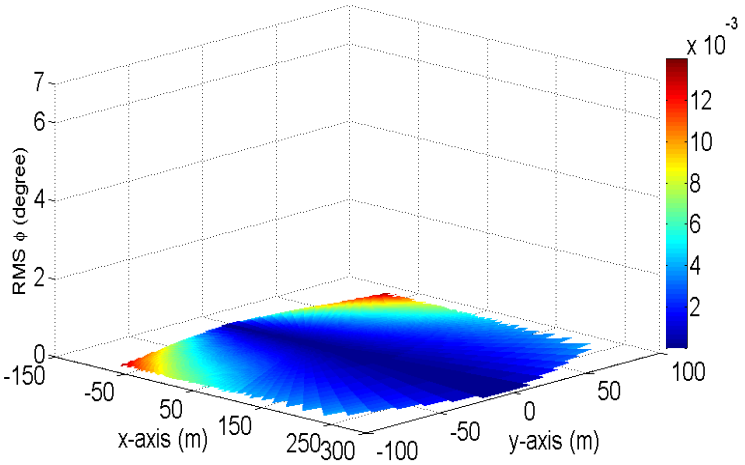

Figure 6.27: Root mean square values of robotics inspired platform yaw displacement at each location in the effective area.

6.6 Failure Analysis

Normally, mooring cables lose their characteristics due to the sea's side effects and time factors. For these reasons, a failure analysis is carried out on the mooring system of the robotics inspired platform.

This section investigates the effect of a mooring cable failure (mooring cable break) on the dynamic behavior of the robotics inspired platform. The center location x = 0 m, y = 0 m, and the submerged depth b = 47 m were used to conduct this analysis.

6.6.1 One Mooring Cable Failure

Figures 6.28 to 6.33 present the motion response of the robotics inspired platform with and without mooring cable failure. Mooring cable 1 was chosen to conduct this analysis. As can be seen from these figures, the amplitude of motion response in the sway, roll and yaw directions with mooring cable failure is far greater than without mooring cable failure.

Also, in the surge, heave and pitch directions the displacement response with mooring cable failure are higher than without mooring cable failure. Further, the displacement responses with mooring cable failure are shifted to the right due to this mooring cable failure. This result is in agreement with the nature of the system, because the stiffness and the tension, which conserves the degree of rigidity of the system, are decreased due to mooring cable failure.

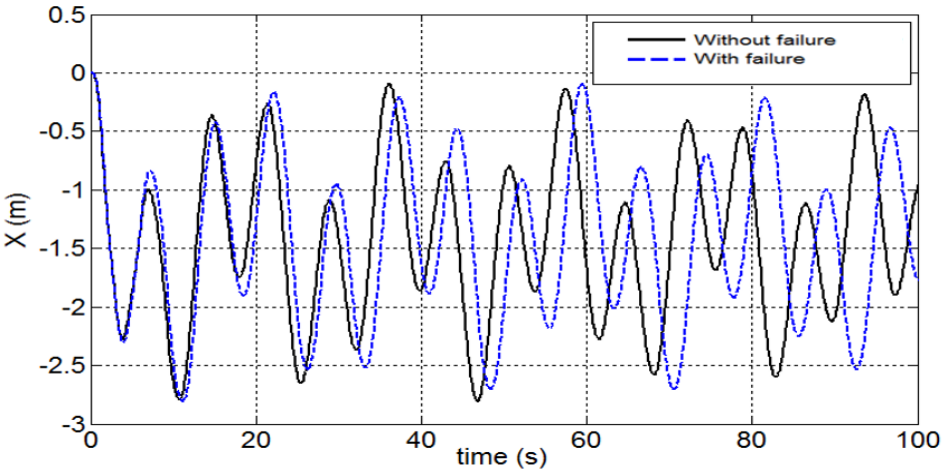

Figure 6.28: The robotics inspired platform surge displacement with/without failure in mooring cable 1.

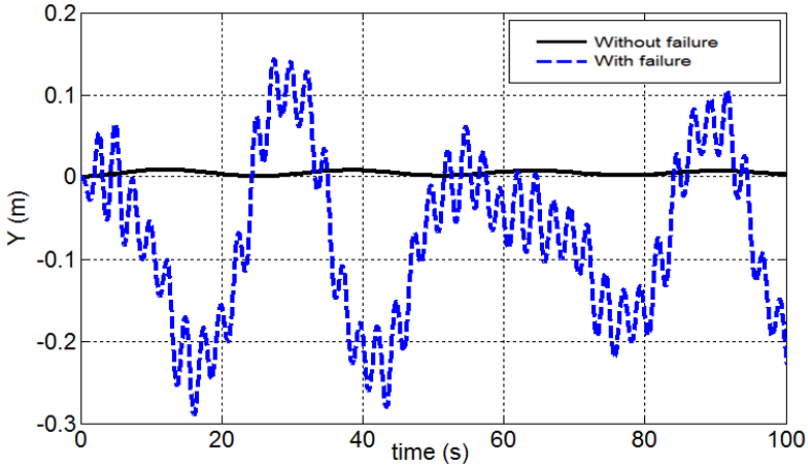

Figure 6.29: The robotics inspired platform sway displacement with/without failure in mooring cable 1.

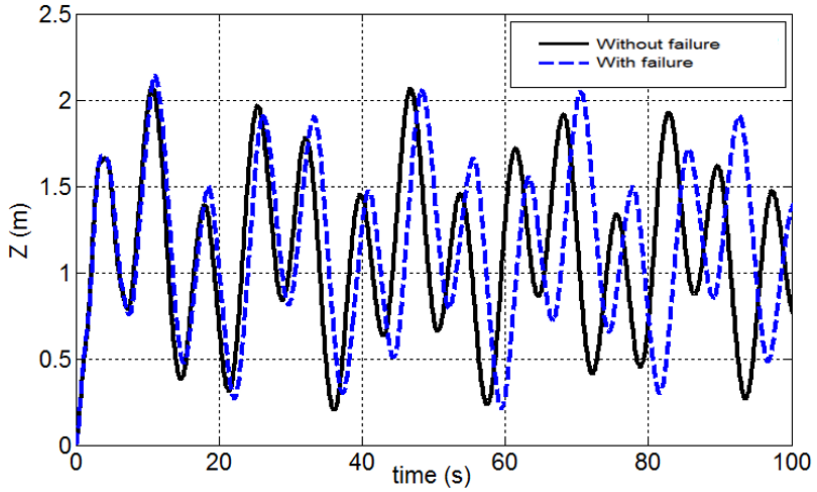

Figure 6.30: The robotics inspired platform heave displacement with/without failure in mooring cable 1.

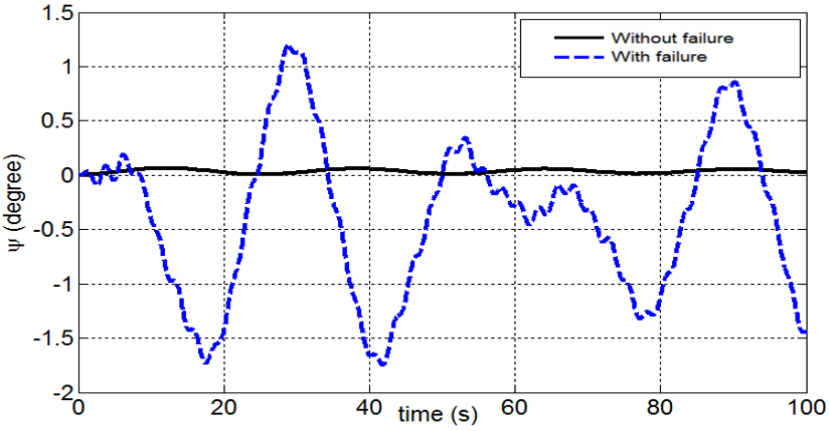

Figure 6.31: The robotics inspired platform roll displacement with/without failure in mooring cable 1.

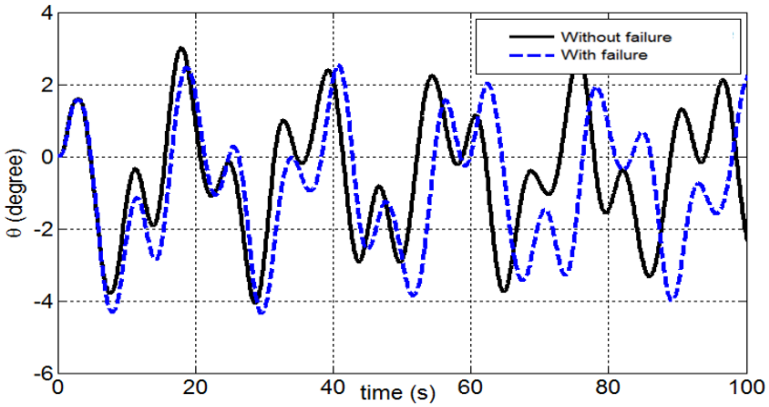

Figure 6.32: The robotics inspired platform pitch displacement with/without failure in mooring cable 1.

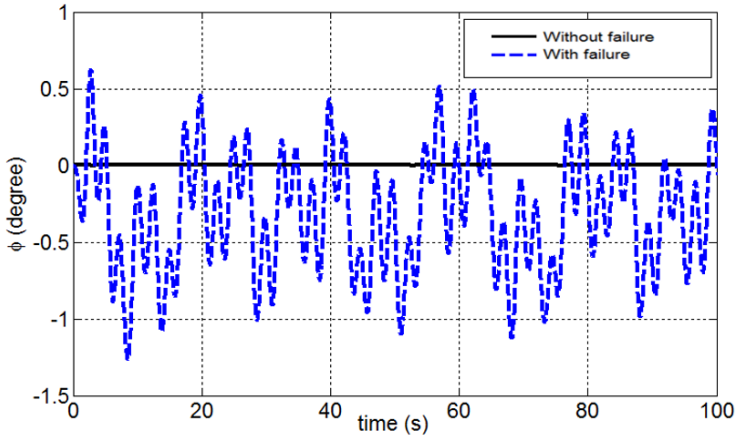

Figure 6.33: The robotics inspired platform yaw displacement with/without failure in mooring cable 1.

6.6.2 One Mooring Bundle Failure

Two study cases were conducted in this section (with and without mooring cable failure). In these two cases, a dynamical response analysis of the robotics inspired platform was conducted with and without a mooring bundle (two mooring cables) failure. The robotics inspired platform position is fixed while the dynamical response was analyzed, which means the results of this particular study present only the first moment of failure to show the instability of the system after a mooring bundle failure.

Figures 6.34 to 6.39 show the motion response of the robotics inspired platform with and without a mooring bundle failure. Mooring bundle 1 (mooring cables 1 and 2) were chosen to conduct this analysis. As can be seen from these figures, the instability of the motion responses in all degrees of freedom appear.

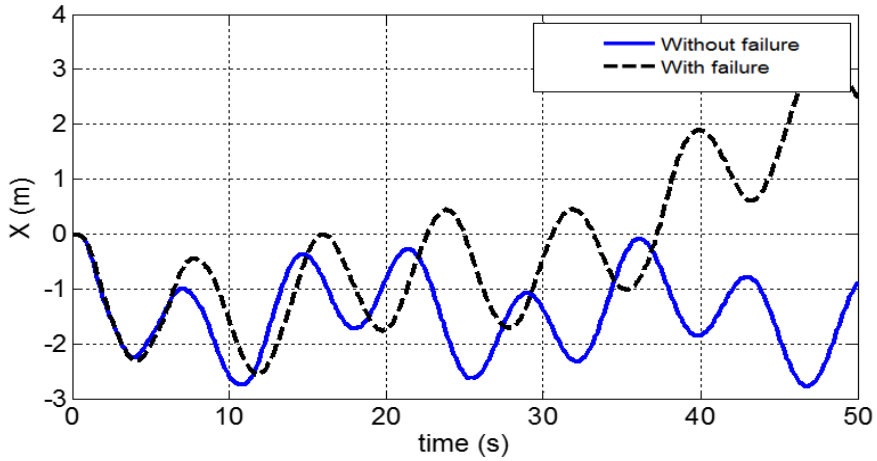

Figure 6.34: The robotics inspired platform surge displacement with/without failure in mooring bundle 1.

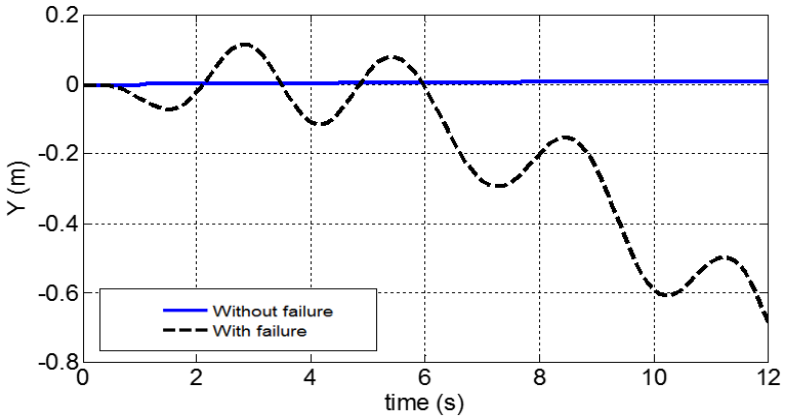

Figure 6.35: The robotics inspired platform sway displacement with/without failure in mooring bundle 1.

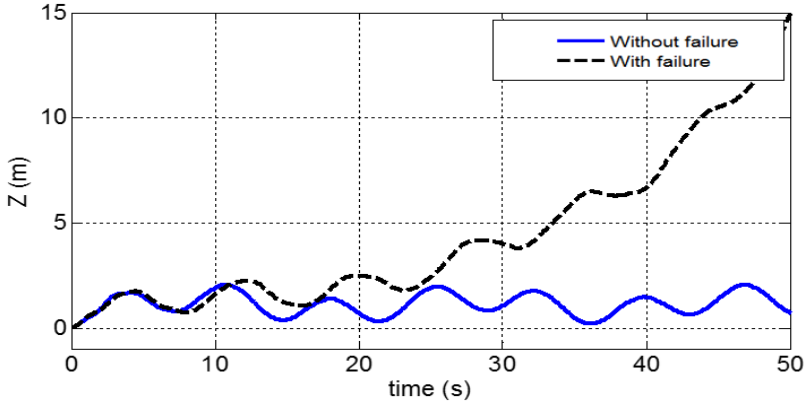

Figure 6.36: The robotics inspired platform heave displacement with/without failure in mooring bundle 1.

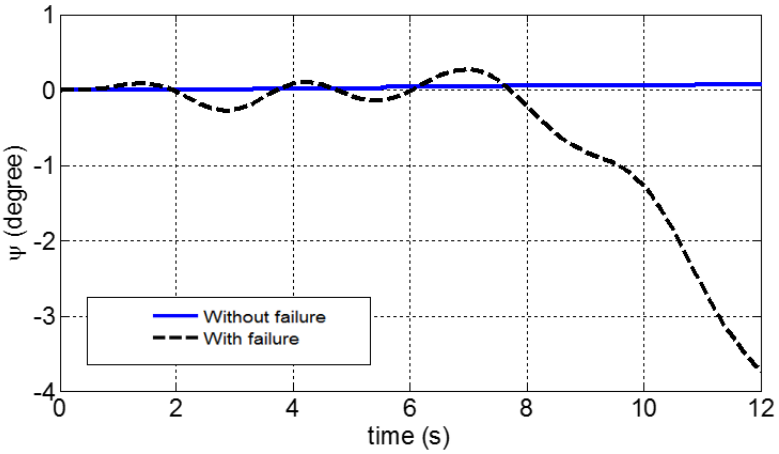

Figure 6.37: The robotics inspired platform roll displacement with/without failure in mooring bundle 1.

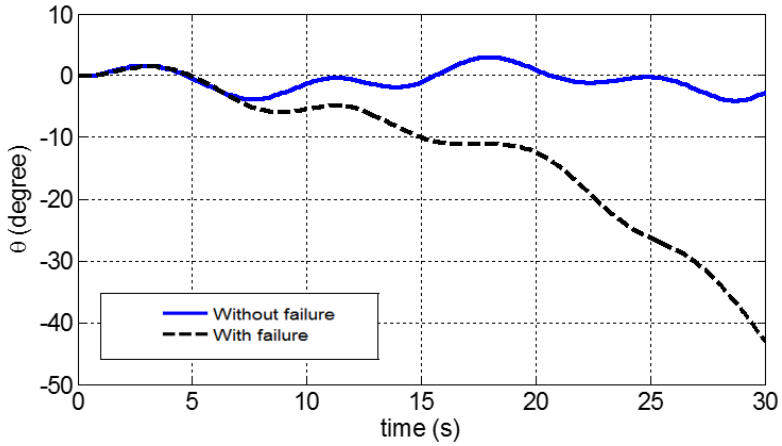

Figure 6.38: The robotics inspired platform pitch displacement with/without failure in mooring bundle 1.

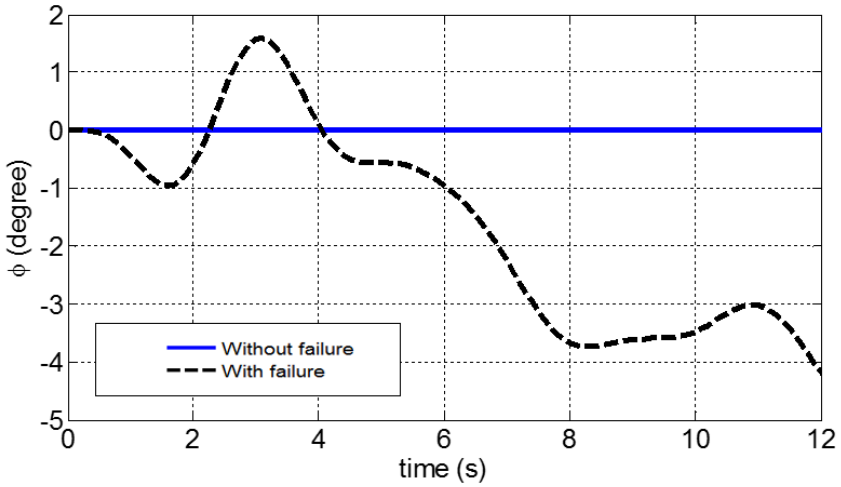

Figure 6.39: The robotics inspired platform yaw displacement with/without failure in mooring bundle 1.

In conclusion, the previous analysis proves the credibility of the condition mentioned in Chapter 2, which states that the number of mooring bundles should be equal to the number of degrees of freedom to have a fully constrained platform in the sea [68].

6.7 Influence of Mooring System Configuration

Having a larger effective area of the MSP helps to decrease the chance of failure in the mooring system when the MSP is exposed to environmental loading. There is a need to incorporate the best possible configuration analysis in design procedure which enhances the effective area of MSP. In this section, an effective area analysis is conducted for different MSP configurations with/without the effect of the Arabian Gulf's impinging water waves.

MSPs consist of a floating structure having a circular cylindrical shape with a radius of 5 m and a height (from the top of the floating structure to the bottom of the spar) of 5 m. MSPs mooring systems are made of 12 mooring cables, divided into six mooring bundles. The stiffness/tension of a mooring bundle is equal to the summation of the stiffness/tension of two mooring cables. The submerged depth of the floating structure is assumed to be constant (3 m). The mean water depth of the floating structure is assumed to be 50 m. The fixed reference is located on the seabed at the center of an imaginary circle of radius 200 m. The mooring bundles are anchored to the seabed at points $A_1, A_2, A_3, A_4, A_5,$ and A_6 which are located on the imaginary circle perimeter, measured from the fixed x-axis. The movable reference is located on the floating structure at the center of mass (Cg). The six mooring bundles are hosted at points $B_1, B_2, B_3, B_4, B_5,$ and B_6 which are positioned on the (u,v)-plane.

Figure 6.40 shows the MSP's configurations which were inspired from the classical spar platform and Stewart Gough parallel manipulator layouts [77]. Table 6.6 represents the A_i and B_i position angles respectively for the MSP configurations to carry out the analysis.

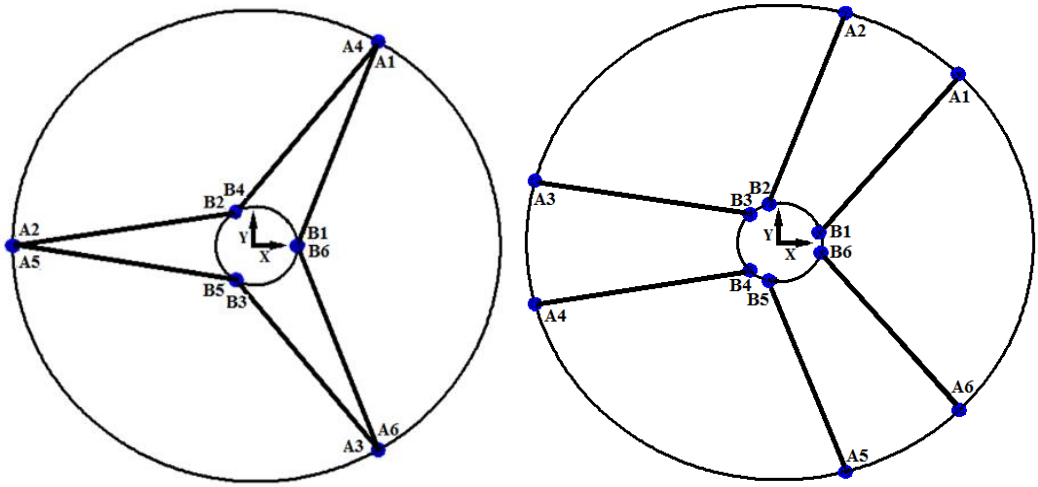

(3-3) (6-6)

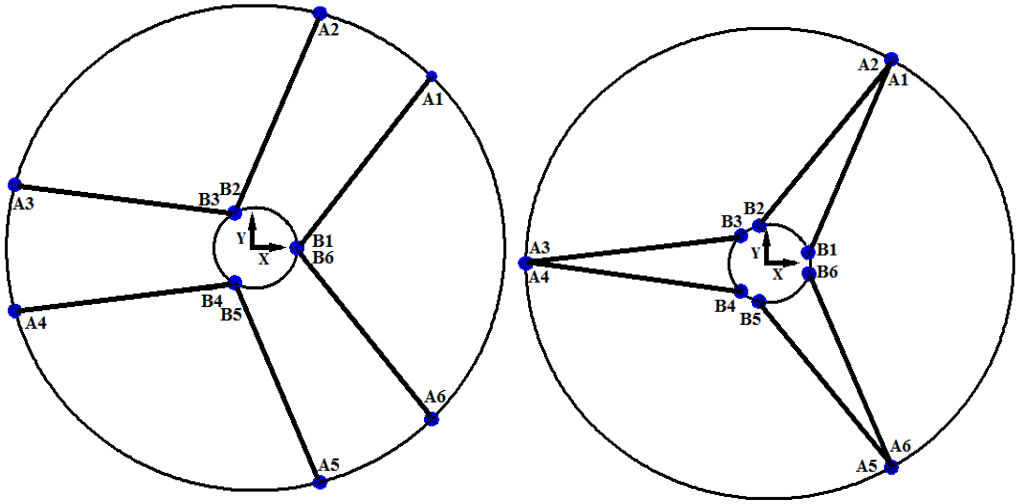

(6-3) (3-6)

Figure 6.40: Top view of MSPs configurations.

Table 6.6: Motors' and anchors' positions angles for MSPs configurations, with respect to the positive x-axis.

3-3 Configuration			6-6 Configuration			6-3 Configuration			3-6 Configuration		
i	A_i (°)	B_i (°)	i	A_i (°)	B_i (°)	i	A_i (°)	B_i (°)	i	A_i (°)	B_i (°)
1	60	0	1	45	15	1	45	0	1	60	15
2	180	120	2	75	105	2	75	120	2	60	105
3	300	240	3	165	135	3	165	120	3	180	135
4	60	120	4	195	225	4	195	240	4	180	225
5	180	240	5	285	255	5	285	240	5	300	255
6	300	0	6	315	245	6	315	0	6	300	345

Figures 6.41 to 6.43 represent the effective areas of the MSP's configurations in a static environment, in a sea water wavy environment, and under the effect of the impinging water waves. In addition, Table 6.7 shows the effective areas' percentage values of the MSP's configurations. Furthermore, Table 6.8 represent the minimum and maximum values of the natural frequencies (Hz) of the MSP's configurations in their effective areas.

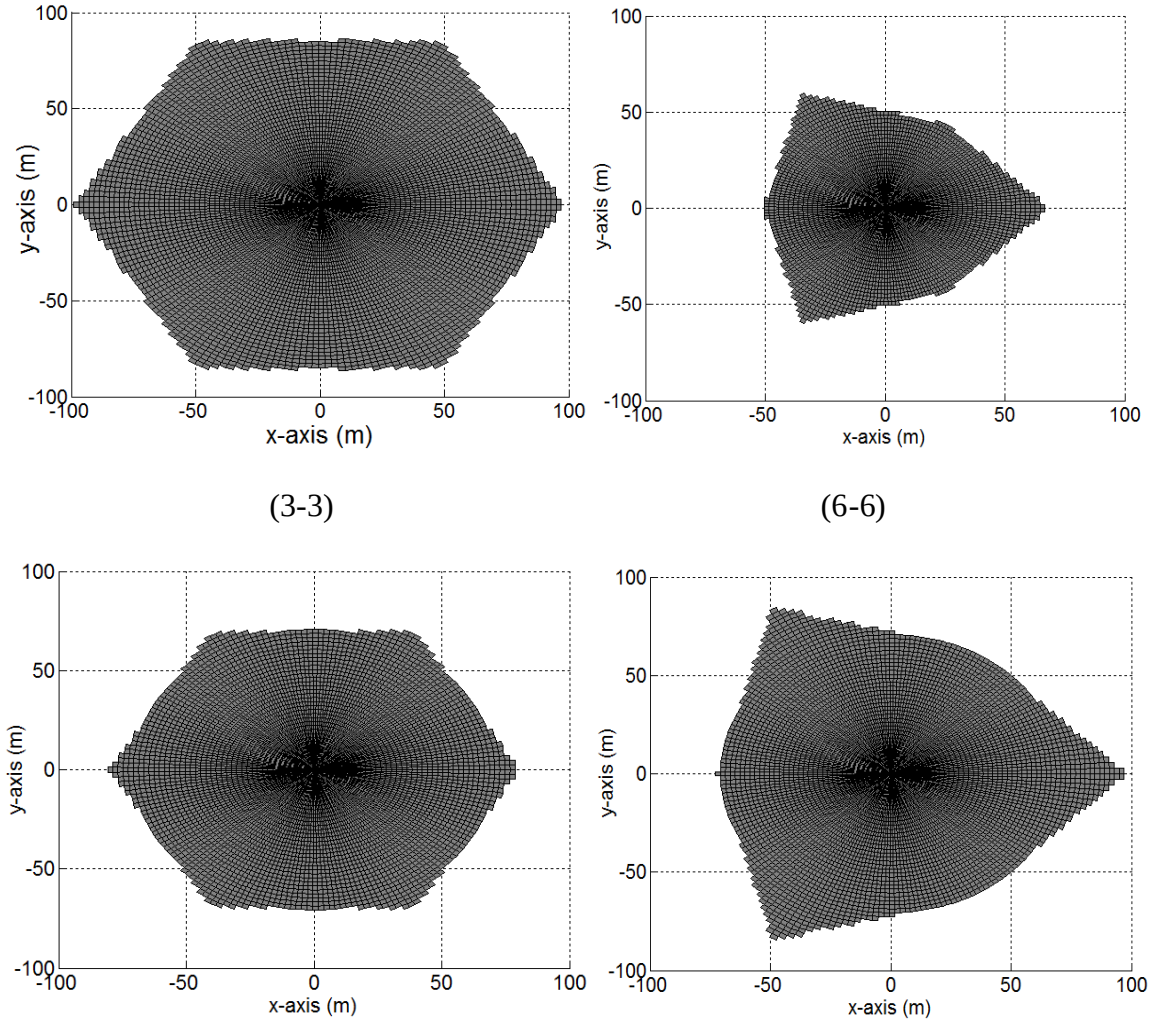

(3-3) (6-6)

(6-3) (3-6)

Figure 6.41: Effective areas of the MSP's configurations in a static environment.

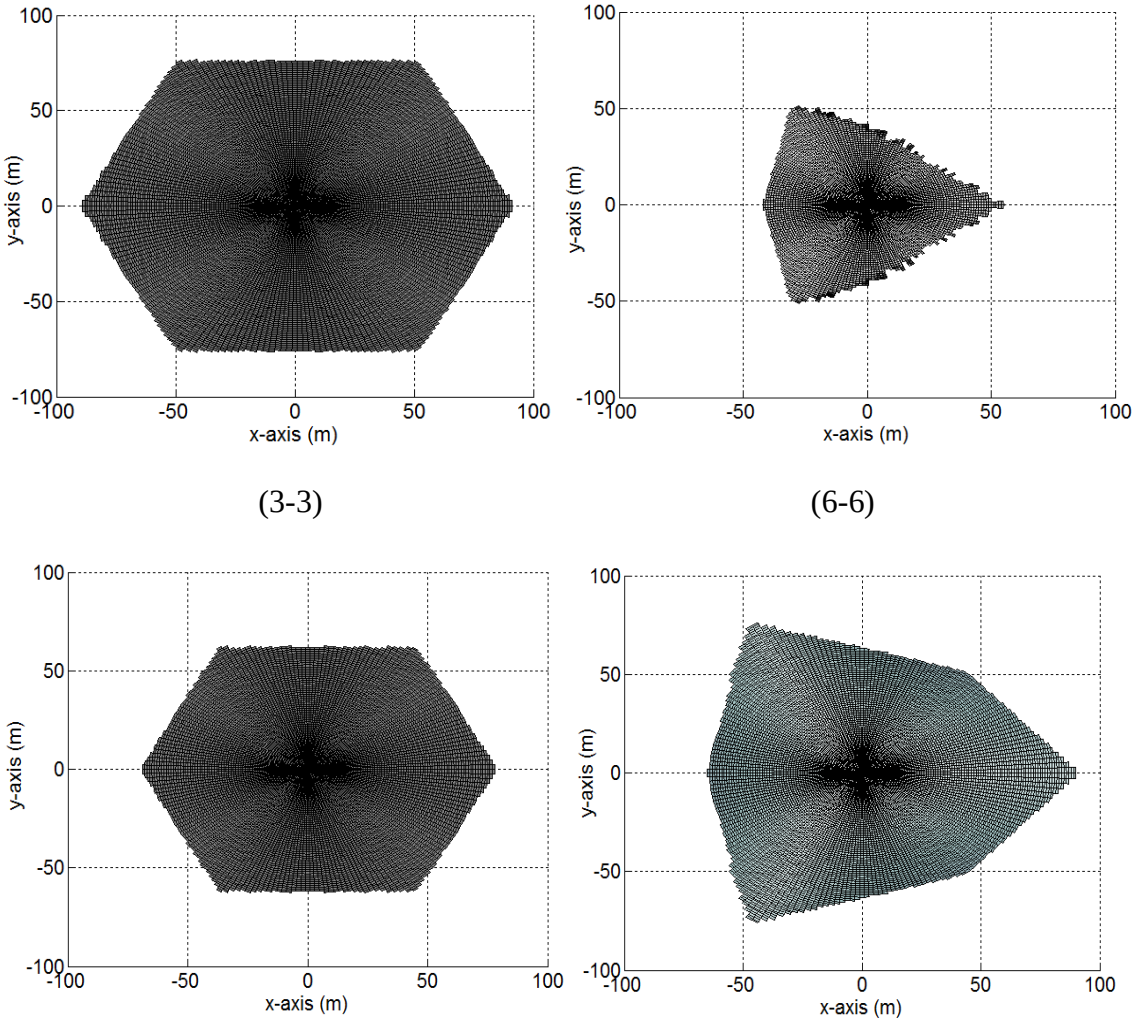

(3-3) (6-6)

(6-3) (3-6)

Figure 6.42: Effective areas of the MSP's configurations under the impinging water wave loads.

Table 6.7: Effective areas (%) of the MSP's configurations out of a square area measuring 200 m per side.

External Loads	3-3 Configuration (%)	6-6 Configuration (%)	6-3 Configuration (%)	3-6 Configuration (%)
Non	63.02	22.66	42.27	46.13
Sea waves	54.14	14.32	35.95	38.73

Table 6.8: Maximum and minimum natural frequencies (Hz) of the MSP's configurations in their effective areas.

External Loads	3-3 Configuration		6-6 Configuration		6-3 Configuration		3-6 Configuration	
	Max	Min	Max	Min	Max	Min	Max	Min
Non	0.541	0.301	0.469	0.313	0.483	0.306	0.521	0.301
Sea waves	0.361	0.265	0.298	0.002	0.267	0.201	0.296	0.225

The impinging water waves' loads significantly decrease the effective area of the MSPs. It is obvious that a 3-3 MSP has the largest effective area, as shown in the figures. While the 6-6 MSP configuration has the lowest effective area, the effective area of a 3-6 MSP configuration is larger than the 6-3 MSP configuration. As shown, the mooring system configuration will directly affect the effective area because of the influence of the directions of the mooring cables' forces. Also, the MSP stiffness is affected by the mooring system configuration. Table 6.8 that the 3-3 MSP has the best degree of rigidity of all configurations. So, the platform mooring system configuration is a factor used to ensure a larger effective area. A larger effective area reduces the chance of system failure while the floating platform moves horizontally due to the environmental loads.

6.8 Chapter Summary

In this chapter, a classical spar configuration was used to study the dynamic analysis of the MSP in a marine environment. The MSP was driven by twelve mooring cables, assumed as six mooring bundles, anchored in the seabed and driven by reel/motor devices which are mounted on the moving structure. Local dynamic analysis at the center location was conducted, showing the mooring bundles' tensions and the MSP displacement in response to sea wave forces.

A global dynamic analysis was conducted using RMS measures of the mooring bundles' tensions and the MSP's displacement across the effective area. The MSP's positive tensions were maintained by varying the submerged depth of the MSP to balance the variable sea wave forces. The minimum submerged depth showed higher values near the effective area edges, indicating higher mooring bundles' tensions are required, which affect the displacement motion response.

Failure analysis was conducted for a fixed position, on the MSP. While one mooring cable failure increased the motion responses' amplitudes. This failure study showed that the MSP has unstable motion response in all degrees of freedom. Finally, the influence of the mooring system configuration on the effective area of MSP was studied. The platform mooring system configuration was a factor which can be used to ensure a larger effective area; this larger effective area will reduce the chance of system failure while the floating platform moves horizontally due to the environmental loads.

CHAPTER 7
CONCLUSIONS AND RECOMMENDATIONS

7.1 Conclusions

In this dissertation, an efficient universal mathematical model was developed to describe the kinematics and dynamics of any floating cable driven/moored platforms (FCDPs) in a static and wavy water environment.

Within the context of rigid-body dynamics, the added mass matrix was established for the FCDP using the strip theory and a flat disk approach. A systematic approach was followed for the development of the stiffness matrix of the FCDP. Using the Jacobean manipulator concept, three components of the stiffness matrix were detailed: (i) the first part reflected the mooring cables' strengths, (ii) the second part was due to the mooring cables' tensions, and (iii) the third part was added due to the hydrodynamic effect. The damping matrix was established for the FCDP as a combination of the mass and stiffness matrices. The mass, damping, and stiffness matrices were established for an FCDP as functions of the platform position.

Offshore environmental loads, including force due to impinging 1-D waves were estimated. The solution for the equations of motion of the FCDPs were solved using a modal formulation. Then, a MatLab code was developed for the FCDP and it was used to generate different numerical results. An experimental study on an FCDP was conducted to validate the developed mathematical model. The obtained numerical results were compared with the

corresponding experimental measurements, showing good agreement. This comparison verified that the developed mathematical model and numerical code for the FCDP were valid.

The dynamics of two types of the floating movable marine platforms was studied, (i) A floating movable cylindrical platform and (ii) A movable spar platform were studied. Measures such as the degree of rigidity, the mooring cables' tensions, and the minimum submerged depth were mentioned to assess the mobility and the degree of rigidity of the FCDPs within their effective area. The following main conclusions were made:

- The minimum submerged depth was plotted across the FCDP's effective areas, which showed higher values near the effective area edges; this indicated that higher mooring cable tensions are required near the edges of the effective area.
- It was shown that increasing the mooring cable stiffness or decreasing the pre-tension resulted in a decrease in the RMS values of the platform displacements, velocities and accelerations.
- Mooring Cable failure analysis was conducted, at a fixed position, on the FCDPs. While one mooring cable failure analysis showed that the FCDP stabilization is decreased, one mooring bundle (two mooring cables) failure analysis showed that the FCDP had unstable dynamic response. Mooring cable failure analysis proved the credibility of the condition mentioned in Chapter 2, which stated that the number of mooring bundles should be equal to the number of degrees of freedom to have a fully constrained platform in the sea [68].

- The platform mooring system configuration was a factor that could be used to have a larger effective area and this larger effective area would reduce the chances of having

non positive mooring cable tensions while the floating platform moved horizontally due to the environmental loads.

- It was shown that the movable spar platform had a larger effective area than the floating movable cylindrical platform, but the floating movable cylindrical platform had more degree of rigidity within its effective area than the movable spar platform.

7.2 Recommendations

The main objective of this work was to study the dynamics of marine platforms, with adaptive mooring system, under various environmental loadings. The following suggested studies should assist in arriving at a better understanding of this topic:

1. The performance of marine platforms for multi-directional random waves involving all 6 DOF should be investigated.
2. An investigation of the riser effects on the dynamic response of marine platforms subjected to different environmental loadings is needed.
3. A fully coupled integrated dynamic analysis in the time domain for the platform and its mooring cables is needed.
4. In-depth work is needed on the optimization of mooring cable system configurations.

References

[1] A. Kareem, "Wind-induced response analysis of tension leg platforms," Journal of Structural Engineering, vol. 111, pp. 37-55, 1985.

[2] Y. E. Mostafa and M. H. El Naggar, "Response of fixed offshore platforms to wave and current loading including soil–structure interaction," Soil Dynamics and Earthquake Engineering, vol. 24, pp. 357-368, 2004.

[3] Offshore Industry. Available: http://maritime-connector.com/wiki/offshore-industry/

[4] R. Lamb. How Offshore Drilling Works. Available: http://science.howstuffworks.com/environmental/energy/offshore-drilling6.htm

[5] Raunekk. (2009). Oil Extraction from Sea Floor - Different Types of Offshore Production Platforms. Available: http://www.brighthubengineering.com/marine-engines-machinery/30775-different-types-of-offshore-production-platforms-for-oil-extraction/

[6] (2015). Semi-submersible. Available: http://en.wikipedia.org/wiki/Semi-submersible

[7] Tension Leg Platform (TLP). Available: http://www.globalsecurity.org/military/systems/ship/platform-tension-leg.htm

[8] Spar Design. Available: http://images.pennwellnet.com/ogj/images/ogj2/9644jsk02.gif

[9] W. Yu and W. Huang, "A new concept of spar and its hydrodynamic analysis," in The Twentieth International Offshore and Polar Engineering Conference, 2010.

[10] (2010). NSF-Funded Research Leads to New Energy Innovations. Available: http://www.nsf.gov/news/newsletter/jun_10/index.jsp

[11] J. Van Santen and K. de Werk, "On the typical qualities of spar type structures for initial or permanent field development," in Offshore Technology Conference, 1976.

[12] J. Bax and K. de Werk, "A floating storage unit designed specifically for the severest environmental conditions," in SPE European Spring Meeting, 1974.

[13] B. Hunter, S. Menard, R. E. Ohman, and R. S. Glanville, "Spar drilling, production, storage platform design takes next step," Offshore International, vol. 53, pp. 37-9, 1993.

[14] E. Horton and J. Halkyard, "A spar platform for developing deep water oil fields," in MTS, 1992, pp. 998-1005.

[15] R. Glanville, J. Paulling, J. Halkyard, and T. Lehtinen, "Analysis of the spar floating drilling production and storage structure," in Offshore Technology Conference, 1991.

[16] H. O. Berteaux, Buoy engineering: John Wiley & Sons, 1976.

[17] F. Fisher and F. Spiess, "Flip-Floating Instrument Platform," The Journal of the Acoustical Society of America, vol. 35, pp. 1633-1644, 1963.

[18] J. Korloo, "Design and installation of a cost-effective spar buoy flare system," in Offshore Technology Conference, 1993.

[19] P. Johnson, "Spar model test Joint Industry Project final report: Project summary," Report of Offshore Technology Research Center, vol. 1, 1995.

[20] J. N. Newman, "Second-order, slowly-varying forces on vessels in irregular waves," 1974.

[21] J. A. Pinkster, "Low frequency second order wave exciting forces on floating structures," TU Delft, Delft University of Technology, 1980.

[22] M.-H. Kim and D. K. Yue, "The complete second-order diffraction solution for an axisymmetric body Part 1. Monochromatic incident waves," Journal of Fluid Mechanics, vol. 200, pp. 235-264, 1989.

[23] M.-H. Kim and D. K. Yue, "The complete second-order diffraction solution for an axisymmetric body Part 2. Bichromatic incident waves and body motions," Journal of Fluid Mechanics, vol. 211, pp. 557-593, 1990.

[24] Z. Ran, M. Kim, J. Niedzwecki, and R. Johnson, "Responses of a spar platform in random waves and currents (Experiment Vs. Theory)," International Journal of Offshore and Polar Engineering, vol. 6, 1996.

[25] Y. Liu, C. Kim, and M. Kim, "The computation of mean drift forces and wave run-up by higher-order boundary element method," in The First International Offshore and Polar Engineering Conference, 1991.

[26] C. Johnson, C. Matos, J. Roesset, and B. Mekha, "Analysis in the time domain of a deep water spar platform," American Society of Mechanical Engineers, New York, NY (United States)1996.

[27] B. Mekha, D. Weggel, C. Johnson, and J. Roesset, "Effects of second order diffraction forces on the global response of spars," in The Sixth International Offshore and Polar Engineering Conference, 1996.

[28] B. Mekha, C. Johnson, and J. Roesset, "Nonlinear response of a spar in deep water: different hydrodynamic and structural models," in The Fifth International Offshore and Polar Engineering Conference, 1995.

[29] A. Chitrapu, S. Saha, and V. Salpekar, "Time-domain simulation of spar platform response in random waves and current," in OMAE 1998: 17 th International Conference on Offshore Mechanics and Arctic Engineering, 1998, p. 1998.

[30] G. Xu, Q. Ma, and L. Sun, "Numerical Investigations on Truss SPAR Motion in Waves," in The Twentieth International Offshore and Polar Engineering Conference, 2010.

[31] I. Anam and J. M. Roesset, "Effect of nonlinear wave kinematics on dynamic response of spars," Journal of engineering mechanics, vol. 128, pp. 925-934, 2002.

[32] a. A. K. B. I. Prislin, "Significance of short crested and diffracted waves on full scale motion correlation of a truss spar," presented at the International Conference on Civil Engineering in the Oceans VI.

[33] W. Ye, I. Anam, and J. Zhang, "Effects of wave directionality on wave loads and dynamics response of a spar," in American Society of Mechanical Engineers, 17 th International Conference on Offshore Mechanics and Arctic Engineering(USA), 1998, p. 6.

[34] A. Chitrapu, S. Saha, and V. Salpekar, "Motion response of spar platform in directional waves and current," in 18th International Conference on Offshore Mechanics and Arctic Engineering (OMAE99/OFT-4237), 1999, pp. 1-9.

[35] B. J. Leira, D. Myrhaug, and J. Voll, "Dynamic response analysis of a spar platform subjected to wind and wave forces," in ASME 2008 27th International Conference on Offshore Mechanics and Arctic Engineering, 2008, pp. 227-234.

[36] I. Anam, J. M. Roesset, and J. M. Niedzwecki, "Time domain and frequency domain analysis of Spar platforms," in The Thirteenth International Offshore and Polar Engineering Conference, 2003.

[37] M. Lake, H. He, A. W. Troesch, M. Perlin, and K. P. Thiagarajan, "Hydrodynamic coefficient estimation for TLP and Spar structures," Journal of Offshore Mechanics and Arctic Engineering, vol. 122, pp. 118-124, 2000.

[38] I. Prislin, R. Blevins, and J. Halkyard, "Viscous damping and added mass of solid square plates," 1998.

[39] A. Magee, A. Sablok, J. Maher, J. Halkyard, L. Finn, and I. Datta, "Heave plate effectiveness in the performance of truss spars," in Proceedings of the ETCE/OMAE2000 Joint Conference, New Orleans, LA, 2000, pp. 1-11.

[40] F. Fischer and R. Gopalkrishnan, "Some observations on the heave behavior of spar platforms," Journal of Offshore Mechanics and Arctic Engineering, vol. 120, pp. 221-225, 1998.

[41] M. Downie, J. Graham, C. Hall, A. Incecik, and I. Nygaard, "An experimental investigation of motion control devices for truss spars," Marine structures, vol. 13, pp. 75-90, 2000.

[42] L. Tao, K. Y. Lim, and K. Thiagarajan, "Heave response of classic spar with variable geometry," Journal of Offshore Mechanics and Arctic Engineering, vol. 126, pp. 90-95, 2004.

[43] H. Haslum and O. Faltinsen, "Alternative shape of spar platforms for use in hostile areas," in Offshore technology conference, 1999.

[44] D. N. Veritas, "SESAM User Manual Wadam," 2008.

[45] A. K. Jha, P. De Jong, and S. R. Winterstein, "Motions of a spar buoy in random seas: Comparing predictions and model test results," Proc., BOSS-97, vol. 2, pp. 333-347, 1997.

[46] S. J. Lim, J. B. Rho, and H. S. Choi, "An experimental study on motion characteristics of cell spar platform," in The Fifteenth International Offshore and Polar Engineering Conference, 2005.

[47] A. Agarwal and A. Jain, "Nonlinear coupled dynamic response of offshore Spar platforms under regular sea waves," Ocean engineering, vol. 30, pp. 517-551, 2003.

[48] L. Finn, J. Maher, and H. Gupta, "The cell spar and vortex induced vibrations," in Offshore Technology Conference, 2003.

[49] F. Zhang, J. Yang, R. Li, and Z. Hu, "Effects of heave plate on the hydrodynamic behaviors of cell spar platform," in 25th International Conference on Offshore Mechanics and Arctic Engineering, 2006, pp. 203-209.

[50] F. Zhang, J.-m. YANG, R.-p. LI, and C. Gang, "Numerical investigation on the hydrodynamic performances of a new spar concept," Journal of Hydrodynamics, Ser. B, vol. 19, pp. 473-481, 2007.

[51] Y. Su, J. Yang, L. Xiao, and G. Chen, "Model test verification of a cell truss spar using hybrid model testing technique," in ASME 2007 26th International Conference on Offshore Mechanics and Arctic Engineering, 2007, pp. 141-148.

[52] F. Zhang, J.-m. YANG, R.-p. LI, and C. Gang, "Coupling effects for cell-truss spar platform: Comparison of frequency-and time-domain analyses with model tests," Journal of Hydrodynamics, Ser. B, vol. 20, pp. 424-432, 2008.

[53] M. Jameel, S. Ahmad, A. S. Islam, and M. Z. Jumaat, "Non-linear dynamic analysis of coupled spar platform," Journal of Civil Engineering and Management, vol. 19, pp. 476-491, 2013.

[54] O. Montasir, A. Yenduri, and V. Kurian, "Effect of mooring line configurations on the dynamic responses of truss spar platforms," Ocean Engineering, vol. 96, pp. 161-172, 2015.

[55] R. E. Harris, L. Johanning, and J. Wolfram, "Mooring systems for wave energy converters: A review of design issues and choices," Marec2004, 2004.

[56] F. Nielsen and A. Bindingbø, "Extreme loads in taut mooring lines and mooring line induced damping: an asymptotic approach," Applied Ocean Research, vol. 22, pp. 103-118, 2000.

[57] V. Anchors, "Vryhof anchor manual," Krimpen ad Yssel, Netherlands, 2005.

[58] Z. Gao and T. Moan, "Mooring system analysis of multiple wave energy converters in a farm configuration," in Proc. of the 8th European Wave and Tidal Energy Conference (EWTEC), Uppsala, Sweden, 2009.

[59] I. Ridge, S. Banfield, and J. Mackay, "Nylon fibre rope moorings for wave energy converters," in OCEANS 2010, 2010, pp. 1-10.

[60] C.-y. Ji, Z.-m. Yuan, and M.-l. Chen, "Study on a new mooring system integrating catenary with taut mooring," China Ocean Engineering, vol. 25, pp. 427-440, 2011.

[61] P. Ricci, A. Rico, P. Ruiz-Minguela, F. Boscolo, and J. Villate, "Design, modelling and analysis of an integrated mooring system for wave energy arrays," in Proceedings of the 4th International Conference on Ocean Energy, 2012.

[62] S. Weller, P. Davies, I. L. Johanning, and S. Banfield, "Guidance on the use of synthetic fibre ropes for marine energy devices," ed: Deliverable, 2013.

[63] R. A. Dalrymple and R. G. Dean, Water wave mechanics for engineers and scientists: Prentice-Hall, 1991.

[64] Available: www.ldeo.columbia.edu/~vaillanc/Lec6Chap7.ppt

[65] S. Neelamani, K. Al-Salem, and K. Rakha, "Extreme Waves For Different Return Periods In The Arabian Gulf."

[66] A. Parvaresh, S. Hassanzadeh, and M. Bordbar, "Statistical analysis of wave parameters in the north coast of the Persian Gulf," in Annales Geophysicae, 2005, pp. 2031-2038.

[67] W. R. a. E. Division, "Aramco Sustaining Research Project Environmental Studies," 1990.

[68] R. G. Roberts, T. Graham, and T. Lippitt, "On the inverse kinematics, statics, and fault tolerance of cable-suspended robots," Journal of Robotic Systems, vol. 15, pp. 581-597, 1998.

[69] O. Faltinsen, Sea loads on ships and offshore structures vol. 1: Cambridge university press, 1993.

[70] J. N. Newman, Marine hydrodynamics: MIT press, 1977.

[71] R. Mansouri and H. Hadidi, "Comprehensive study on the linear hydrodynamic analysis of a truss spar in random waves," World Academy of Science, Engineering and Technology, vol. 53, pp. 930-942, 2009.

[72] M. Denny, Ecological Mechanics: Principles of Life's Physical Interactions, Princeton University Press, 2015.

[73] O. Brunstad, "Multi-span suspension bridge with floating towers," 2013.

[74] A. Incecik, "Design aspects of the hydrodynamic and structural loading on floating offshore platforms under wave excitation," University of Glasgow, 1982.

[75] I. Anan, Evaluation of the dynamic response of Spar platforms, 2000.

[76] S. Chandrasekaran and A. Jain, "Dynamic behaviour of square and triangular offshore tension leg platforms under regular wave loads," Ocean Engineering, vol. 29, pp. 279-313, 2002.

[77] J.-y. Gu, J.-m. Yang, and H.-n. Lv, "Studies of TLP dynamic response under wind, waves and current," China Ocean Engineering, vol. 26, pp. 363-378, 2012.

[78] L.-W. Tsai, Robot analysis: the mechanics of serial and parallel manipulators: John Wiley & Sons, 1999.

[79] S. Kawamura and K. Ito, "A new type of master robot for teleoperation using a radial wire drive system," in Intelligent Robots and Systems' 93, IROS'93. Proceedings of the 1993 IEEE/RSJ International Conference on, 1993, pp. 55-60.

[80] A. Ming and T. Higuchi, "Study on multiple degree-of-freedom positioning mechanism using wires. I: Concept, design and control," International Journal of the Japan Society for Precision Engineering, vol. 28, pp. 131-138, 1994.

[81] J. Pusey, A. Fattah, S. Agrawal, and E. Messina, "Design and workspace analysis of a 6–6 cable-suspended parallel robot," Mechanism and machine theory, vol. 39, pp. 761-778, 2004.

[82] E. Stump and V. Kumar, "Workspaces of cable-actuated parallel manipulators," Journal of Mechanical Design, vol. 128, pp. 159-167, 2006.

[83] C. B. Pham, S. H. Yeo, G. Yang, M. S. Kurbanhusen, and I.-M. Chen, "Force-closure workspace analysis of cable-driven parallel mechanisms," Mechanism and Machine Theory, vol. 41, pp. 53-69, 2006.

[84] P. Bosscher, A. T. Riechel, and I. Ebert-Uphoff, "Wrench-feasible workspace generation for cable-driven robots," Robotics, IEEE Transactions on, vol. 22, pp. 890-902, 2006.

[85] M. Gouttefarde and C. M. Gosselin, "Analysis of the wrench-closure workspace of planar parallel cable-driven mechanisms," Robotics, IEEE Transactions on, vol. 22, pp. 434-445, 2006.

[86] X. Diao and O. Ma, "Force-closure analysis of general 6-DOF cable manipulators," in Intelligent Robots and Systems, 2007. IROS 2007. IEEE/RSJ International Conference on, 2007, pp. 3931-3936.

[87] S. Behzadipour and A. Khajepour, "Stiffness of cable-based parallel manipulators with application to stability analysis," Journal of mechanical design, vol. 128, pp. 303-310, 2006.

[88] A. Moradi, "Stiffness Analysis of Cable-Driven Parallel Robots," 2013.

[89] R. Kobes. (1997). Buoyant Forces. Available: http://theory.uwinnipeg.ca/physics/fluids/node10.html.

[90] W. Finnegan, M. Meere, and J. Goggins, "The wave excitation forces on a truncated vertical cylinder in water of infinite depth," Journal of Fluids and Structures, vol. 40, pp. 201-213, 2013.

[91] S. S. Rao and F. F. Yap, Mechanical vibrations vol. 4: Addison-Wesley Reading, 1995.

[92] M. Hassan and A. Khajepour, "Analysis of a large-workspace cable-actuated manipulator for warehousing applications," in ASME 2009 International Design Engineering Technical Conferences and Computers and Information in Engineering Conference, 2009, pp. 45-53.

[93] M. Yang, B. Teng, D. Ning, and Z. Shi, "Coupled dynamic analysis for wave interaction with a truss spar and its mooring line/riser system in time domain," Ocean Engineering, vol. 39, pp. 72-87, 2012.

[94] S. Jeon, Y. Cho, M. Seo, J. Cho, and W. Jeong, "Dynamic response of floating substructure of spar-type offshore wind turbine with catenary mooring cables," Ocean Engineering, vol. 72, pp. 356-364, 2013.

[95] M. J. Muliawan, M. Karimirad, Z. Gao, and T. Moan, "Extreme responses of a combined spar-type floating wind turbine and floating wave energy converter (STC) system with survival modes," Ocean Engineering, vol. 65, pp. 71-82, 2013.

[96] M. J. Muliawan, M. Karimirad, and T. Moan, "Dynamic response and power performance of a combined spar-type floating wind turbine and coaxial floating wave energy converter," Renewable Energy, vol. 50, pp. 47-57, 2013.

[97] M. Karimirad and T. Moan, "Feasibility of the application of a spar-type wind turbine at a moderate water depth," Energy Procedia, vol. 24, pp. 340-350, 2012.

[98] B. Koo, M. Kim, and R. Randall, "Mathieu instability of a spar platform with mooring and risers," Ocean engineering, vol. 31, pp. 2175-2208, 2004.

[99] Z. Ran, Coupled dynamic analysis of floating structures in waves and currents, 2000.

[100] M. Yu, Z.-q. Hu, and L.-f. Xiao, "Wind-wave induced dynamic response analysis for motions and mooring loads of a spar-type offshore floating wind turbine," Journal of Hydrodynamics, Ser. B, vol. 26, pp. 865-874, 2015.

VITA

Name: MAMON HOROUB

Place of Birth: Hebron, Palestine.

Nationality: Palestinian, Jordanian Passport

Permanent Address: Dayr Samet,

Dura, Hebron,

Palestine.

Telephone: +970-599897661, +966-596429407

Email Address: mamonhoroub@gmail.com

Educational Qualification:

PhD (Mechanical Engineering)

March, 2016

King Fahd University of Petroleum and Minerals

Dhahran, Saudi Arabia.

M.S (Mechanical Engineering)

Dec, 2011

King Fahd University of Petroleum and Minerals

Dhahran, Saudi Arabia.

B. Tech. (Mechatronics Engineering)

January 2009

Collage of Eng. & Technology-Palestine Polytechnic

University (PPU).Hebron-Palestine.

Research Activities

- **Horoub M.**, Hassan, M., Hawwa M.A., "Dynamic Analysis of a Floating Cable-driven Platform for Marine Applications," *Proceedings of the 3rd International Conference on Mechanical Engineering and Mechatronics 2014*, Paper No. 153.

- **Mamon Horoub**, Mahir Hassan, Muhammad Hawwa, "Workspace Analysis of a Floating Cable-Driven Platform for Marine Applications," *Proceedings of the International Conference on Mechanical Engineering and Mechatronics 2013*.

- M. A. Hawwa, and **M. H. Mamon**, "Reduction of noise using multiple expansion chambers," *Canadian Acoustics*, vol. 39, no. 3, pp. 146-147, 2011.

- **Mamon Horoub**, Mahir Hassan, Muhammad Hawwa, "Dynamic Analysis of a Cable-Driven Marine Platform within Its Workspace," Submitted to *Journal of* Mechanical Engineering Science.

- **Mamon Horoub**, Muhammad Hawwa, "SPAR Marine Platform Inspired by Robotic Manipulator," *under preparation.*